Hypernucler γ-ray spectroscopy via the ^{12}C(π^+, K^+) reaction

A dissertation

by

KENJI HOSOMI

Submitted to
Department of Physics, Tohoku University
in partial fulfillment of the requirements
for the degree of Doctor of Science

February, 2013

Abstract

The precise structures of ${}^{11}_{\Lambda}$B and ${}^{12}_{\Lambda}$C were experimentally revealed by the high-resolution γ-ray spectroscopy technique. This dissertation presents the results of the KEK-E566 experiment performed at the KEK-PS K6 beam line in 2005. The purpose of the experiment was to investigate the ΛN interaction in p-shell hypernuclei including the coupling between the ΛN and ΣN channels (ΛN-ΣN coupling).

In the KEK-E566 experiment, ${}^{11}_{\Lambda}$B and ${}^{12}_{\Lambda}$C were produced via the ^{12}C(π^+, K^+) reaction at $p_\pi = 1.05$ GeV/c, where ${}^{11}_{\Lambda}$B was produced through one proton emission from particle-unbound excited states of ${}^{12}_{\Lambda}$C. The K6 beam spectrometer for incident pions and Superconducting Kaon Spectrometer (SKS) for outgoing kaons were employed to identify the hypernuclear production. The hypernuclear γ rays were detected by a dedicated germanium detector array, Hyperball2, in coincidence with the (π^+, K^+) reaction.

We succeeded in observing three γ-ray transitions from ${}^{11}_{\Lambda}$B and four transitions from ${}^{12}_{\Lambda}$C. The energy spacings of three spin doublets, ${}^{11}_{\Lambda}$B$(3/2^+, 1/2^+)$, ${}^{11}_{\Lambda}$B$(7/2^+, 5/2^+)$ and ${}^{12}_{\Lambda}$C$(2^-_1, 1^-_1)$, were experimentally determined. The available p-shell hypernuclear data including these results were systematically studied in terms of shell-model calculations with the parametrized effective ΛN interaction and the effect of ΛN-ΣN coupling from the NSC97f interaction, which is one of the Nijmegen models. As a result, we found that ΛN-ΣN coupling makes significant contributions of varying size in p-shell spin-doublet spacings. Since the energy spacing of the ${}^{12}_{\Lambda}$C$(2^-_1, 1^-_1)$ doublet is very sensitive to the effect of ΛN-ΣN coupling, the present experimental result strongly favors the NSC97f interaction for ΛN-ΣN coupling.

We also succeeded in identifying three peaks in the ${}^{12}_{\Lambda}$C mass spectrum from a coincidence analysis with the specified hypernuclear γ-ray events. The new peak at $B_\Lambda = -4.9$ MeV was observed for the first time by selecting the ${}^{11}_{\Lambda}$B$(1/2^+ \to 5/2^+)$ transition. Although more theoretical studies are necessary, we suggest the assignment of ${}^{12}_{\Lambda}$C(3^-) for this peak with the $[p_n^{-1}, d_\Lambda]$ configuration. The production process of ${}^{12}_{\Lambda}$C(2^-_1) state was examined by precisely analyzing the mass spectrum attributed to the ${}^{12}_{\Lambda}$C$(2^-_1 \to 1^-_1)$ transition. As a result, we obtained the first experimental evidence that the spin-flip 2^-_1 state is directly populated by the (π^+, K^+) reaction. It was also found that the state at $B_\Lambda = -2.7$ MeV assigned as the 2^+ state de-excites via the $2^+ \to 2^-_1$ transition with a $\sim$80 % branching ratio.

Acknowledgement

My heartfelt appreciation goes to all members of the KEK-E566 collaboration and the SKS stuffs of KEK for their great efforts to perform the present experiment.

I would like to express his sincere gratitude to Professor H. Tamura, who is my supervisor and the spokesperson of the KEK-E566 experiment. He gave me a lot of invaluable knowledge about experimental techniques and nuclear physics. I learned the attitude as a scientist through discussions with him.

I would like to thank the Professors of the Hyperball group, T. Koike, M. Ukai and K. Miwa for their support of the experiment and the analysis. I am greatly indebted to them for their bright ideas and suggestions for this work. I am also grateful to the professors of the Strangeness Nuclear Physics group, S. N. Nakamura, Y. Fujii, M. Kaneta and K. Tsukada for their advice and encouragements. My special thanks goes to Mr. N. Chiga, who is a technical staff of Tohoku University. He told me many of expertise in designing and machining detectors. I am heartily thankful to my colleagues, Dr. Y. Okayasu, Dr. A. Matsumura, Dr. Y. Ma, Dr. K. Futatsukawa, Dr. K. Shirotori, Dr. D. Kawama, Dr. B. Beckford, Mr. M. Mimori, Mr. T. O. Yamamoto, Mr. S. Gogami, Mr. R. Honda and Mr. S. Nagao for providing a very fulfilling university life. We have improved ourselves through friendly rivalry.

Last but not the least, I would like to express my gratitude to my family for their moral support and warm encouragements.

Contents

Chapter 1

Introduction

A hypernucleus is a baryonic many-body system composed of protons, neutrons and a few hyperons, such as Λ, Σ and Ξ. Study of hypernuclear structure based on two-body hyperon-nucleon (YN) and hyperon-hyperon (YY) interactions leads to the unified understanding of general baryon-baryon (BB) interactions beyond the well-known NN interaction. As the first step toward the unified understanding, the ΛN interaction has been studied so far through the spectroscopic experiments of Λ hypernuclei, in which only one Λ hyperon is included.

This dissertation focuses on an experimental study of Λ hypernuclei ($^{11}_{\Lambda}$B and $^{12}_{\Lambda}$C) using a γ-ray spectroscopy technique. A high-resolution measurement by using germanium (Ge) detectors can reveal precise level structures of the hypernuclei and help us investigate particularly the spin-dependent part of the ΛN interaction.

1.1 ΛN interaction and Λ hypernuclear structure

The forces between baryons are considered to be mediated by mesons in meson-exchange models. They have been extended to YN and YY interactions from the NN interaction using the flavor SU(3) symmetry. In the NN case, the long-range part is explained by the one-pion-exchange picture, while the short-range part, which is attributed to the heavier meson exchange, is not understood well. Although the meson-exchange models phenomenologically describe the short-range force including the repulsive core, it is rather natural to consider the quark-gluon exchange picture of the constituent quarks in the range shorter than the baryon radius. In the study of the BB interactions, the Nijmegen [1] and Jülich [2, 3] models are available for the meson-exchange model, and the quark cluster model [4] is for the quark model. The property of these models can be tested by experimental data of the ΛN interaction.

When we study the ΛN interaction experimentally, providing a low-energy Λ

beam is quite difficult due to a short lifetime (263 ps) of a Λ hyperon. This is why the ΛN interaction has been studied by spectroscopic investigation of Λ hypernuclei, unlike the study of NN interaction via scattering experiments. The ΛN interaction can be extracted from the level structure of hypernuclei, but it is the "effective" interaction which includes the effects from nuclear medium such as the Pauli principle and many-body effects. It is known that the bare ΛN interaction in the free space and the effective ΛN interaction in the nuclear medium can be connected through a G-matrix calculation [5]. The G-matrix calculation for the ΛN interaction succeeds in connecting between the bare and effective interactions quantitatively unlike the case of the NN interaction. This advantage comes from the fact that a Λ hyperon in the nuclear medium is free from the Pauli blocking effect at least in the baryon level and the fact that the ΛN interaction is relatively weaker than the NN interaction. For this reason, it has been long recognized that the energy spectra of Λ hypernuclei can provide a direct information on the bare ΛN interaction.

1.1.1 Spin-dependent ΛN interaction

The effective ΛN interaction is given by the following equation.

$$V_{\Lambda N}(r) = V_0(r) + V_\sigma(r)\boldsymbol{s}_N \cdot \boldsymbol{s}_\Lambda + V_\Lambda(r)\boldsymbol{l}_{N\Lambda} \cdot \boldsymbol{s}_\Lambda + V_N(r)\boldsymbol{l}_{N\Lambda} \cdot \boldsymbol{s}_N + V_T(r)\boldsymbol{S}_{12} \ , \quad (1.1)$$

$$\boldsymbol{S}_{12} = \frac{3(\boldsymbol{s}_N \cdot \boldsymbol{r})(\boldsymbol{s}_\Lambda \cdot \boldsymbol{r})}{r^2} - \boldsymbol{s}_N \cdot \boldsymbol{s}_\Lambda \ ,$$

where $\boldsymbol{r}$ means the relative coordinate between a Λ hyperon and a nucleon, and $\boldsymbol{l}_{N\Lambda}$ stands for the relative orbital angular momentum. The $\boldsymbol{s}_N$ is the spin angular momentum operator of the nucleon and the $\boldsymbol{s}_\Lambda$ is that of the Λ hyperon. The terms, V_0, V_σ, V_Λ, V_N and V_T, correspond to the spin-averaged central force, the spin-spin force, the Λ-spin-dependent spin-orbit force, the N-spin-dependent spin-orbit force and the tensor force, respectively. The strength of the spin-averaged central force is obtained from the binding energies of Λ hypernuclei over a wide range of mass number. The binding energies of Λ hypernuclei can be well reproduced by a simple Woods-Saxon type single particle potential with a 28-MeV depth [6], which is about 2/3 of the nucleon potential depth. The other terms are spin-dependent and must be studied through the hypernuclear level structure.

When we study the level structure of hypernuclei, a weak-coupling scheme is assumed that a hypernucleus consists of two components, a Λ hyperon and the remaining "core" nucleus, and the Λ hyperon does not change the structure of the core nucleus. In this scheme, low-lying levels of hypernuclei are described as follows. Suppose that a core nucleus ($^{\mathrm{A\text{-}1}}$Z) has a non-zero spin J and a Λ hyperon is added in the

s orbit. Since a Λ hyperon has 1/2 spin, the state of a hypernucleus ($^{\rm A}_{\Lambda}$Z) splits into spin-doublet states with the spins of $J+1/2$ and $J-1/2$ as shown in Figure 1.1. The spatial wavefunctions of the spin-doublet states are the same in the weak-coupling limit. Therefore, the energy spacing of the spin-doublet states is determined only by the ΛN spin-dependent interactions. The energy spacing is typically of the order of 100 keV, and thus a γ-ray spectroscopy method using germanium (Ge) detectors with a few keV resolution is necessary to resolve their splitting.

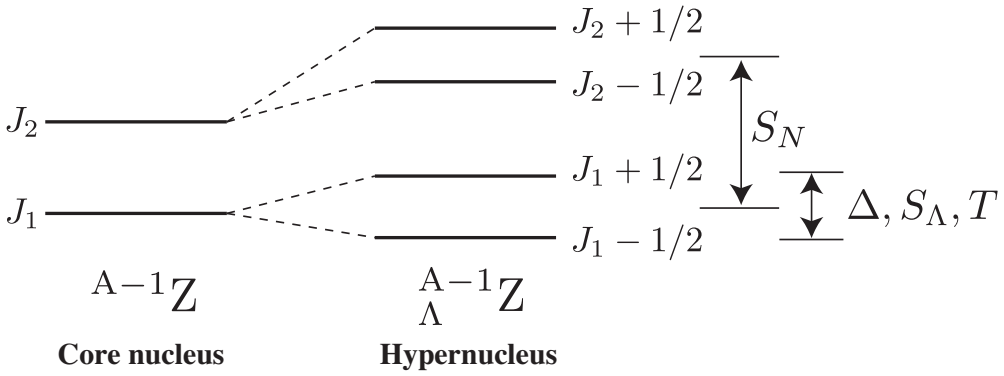

Figure 1.1: Low-lying hypernuclear levels and the main components of the energy spacing based on the parameters of the effective two-body interaction.

1.1.2 Shell model approach

For the p-shell hypernuclei, a phenomenological approach to the study of hypernuclear structure with shell-model calculations was first made by Gal, Soper and Dalitz [7, 8, 9] and then improved by Millener [10, 11, 12]. In this approach, the strength of each spin-dependent term in Eq. 1.1 is expressed as Δ, S_Λ, S_N and T by taking the radial integrals over the shell model wavefunctions. For example, Δ is defined as

$$\Delta = \int \phi^*_{\Lambda N}(r) V_\sigma(r) \phi_{\Lambda N}(r) r^2 dr \ ,$$

where $\phi_{\Lambda N}(r)$ is the radial part of the relative wavefunction between a Λ hyperon in the s orbit and a nucleon in the p orbit. Similarly, the others are defined from $V_\Lambda(r)$, $V_N(r)$ and $V_T(r)$. They can be treated as parameters to be determined phenomenologically by fitting the data of p-shell hypernuclear level energies.

When we consider the low-lying levels of p-shell hypernuclei, the energy spacings of two levels are described by liner combinations of those four spin-dependent pa-

rameters. In the case of the spin-doublet states which share the same core state, the energy spacing is written as

$$E_{upper} - E_{lower} = a\Delta + bS_\Lambda + cS_N + dT \ ,$$

where a, b, c and d are the coefficients which are evaluated by shell-model calculations. In the case of two hypernuclear states which have different core states, their energy spacing is written as

$$E_{upper} - E_{lower} = \Delta E_{core} + a'\Delta + b'S_\Lambda + c'S_N + d'T \ ,$$

where ΔE_{core} denotes the difference of excitation energies between the core states. In the weak-coupling limit, the energy spacing of spin doublet is determined by Δ, S_Λ and T, while S_N changes the effective spacing of core levels as illustrated in Figure 1.1.

The coefficients for various p-shell hypernuclei are given by Millener. His shell-model calculations are perfumed for $\{s^4p^{\mathrm{A}-5}s_\Lambda\}$ configurations mainly using the interaction of Cohen and Kurath [13] for the core wavefunctions.

1.1.3 ΛNN three-body interaction

The YN interaction involves the coupling between the ΛN and ΣN channels (ΛN-ΣN coupling) as illustrated in Figure 1.2. It is pointed out that the direct ΛN-ΛN channel does not contain a one-pion exchange contribution because of isospin conservation while the ΛN-ΣN coupling channels does. Therefore, the ΛN interaction is relatively weak, and there is a reason to believe that the ΛNN three-body interaction in a hypernucleus could be important. Since the effect of the ΛNN three-body interaction cannot be incorporated in the effective two-body ΛN interaction, it has to be estimated for each hypernuclear levels in the present framework.

Recently, Akaishi *et al.* [14] succeeded in reproducing well the binding energies of A=3, 4 and 5 hypernuclei by introducing the effective ΛNN three-body interaction explicitly, where the NSC97f interaction of the Nijmegen models gave rather plausible results. According to their calculation, the spacing of the ${}^{4}_{\Lambda}\mathrm{He}(1^+, 0^+)$ doublet is caused roughly a half by the spin-spin interaction and a half by the ΛNN three-body interaction.

Millener calculated the effect of ΛN-ΣN coupling in p-shell hypernuclear levels based on the NSC97f interaction through G-matrix calculation. The effect is found to be generally small in p-shell hypernuclei compared with the s-shell case, but it still has a non-negligible contribution. Then, the energy spacing of p-shell hypernuclear

levels is expressed as

$$E_{upper} - E_{lower} = (\Delta E_{core}+)\ a\Delta + bS_\Lambda + cS_N + dT + \Lambda\Sigma\ ,$$

where $\Lambda\Sigma$ denotes the effect of ΛN-ΣN coupling and $\Delta E_{core} = 0$ in the case of spin-doublet states. It is pointed out that the $\Lambda\Sigma$ strength must be experimentally determined because the ΛN-ΣN coupling component of the NSC97f interaction is one of the theoretical predictions.

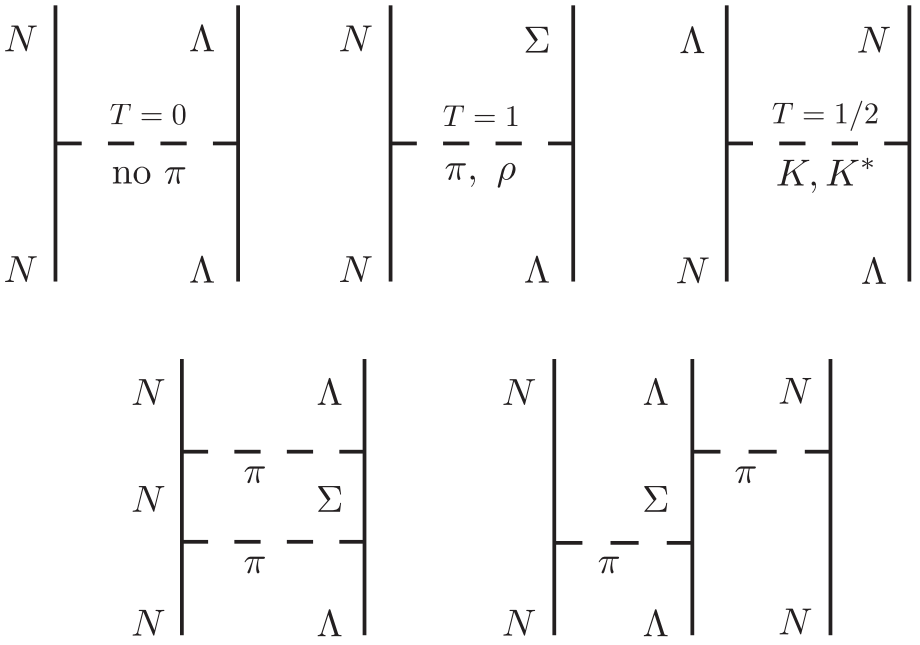

Figure 1.2: Diagrams for the direct ΛN-ΛN channel and the ΛN-ΣN coupling channels. The one-pion exchange is forbidden in the direct channel due to isospin conservation. The last diagram shows the two-pion exchange three-body interaction.

1.2 Hyperball project

High-precision γ-ray spectroscopy technique of hypernuclei using a dedicated Ge detector array, Hyperball, was established in 1998 [15]. Thereafter, a series of experiments has successfully revealed detailed level schemes of several p-shell Λ hypernuclei, ${}^{7}_{\Lambda}$Li [16, 17, 18, 19], ${}^{9}_{\Lambda}$Be [20], ${}^{10}_{\Lambda}$B [21], ${}^{11}_{\Lambda}$B [22], ${}^{15}_{\Lambda}$N [23] and ${}^{16}_{\Lambda}$O [23, 24], in KEK (E419, E509, E518) and BNL (E930). Observed γ transitions and determined level schemes are summarized in Figure 1.3. The most important purpose of Hyperball experiments was to determine the four parameters (Δ, S_Λ, S_N and T) in the effective ΛN interaction.

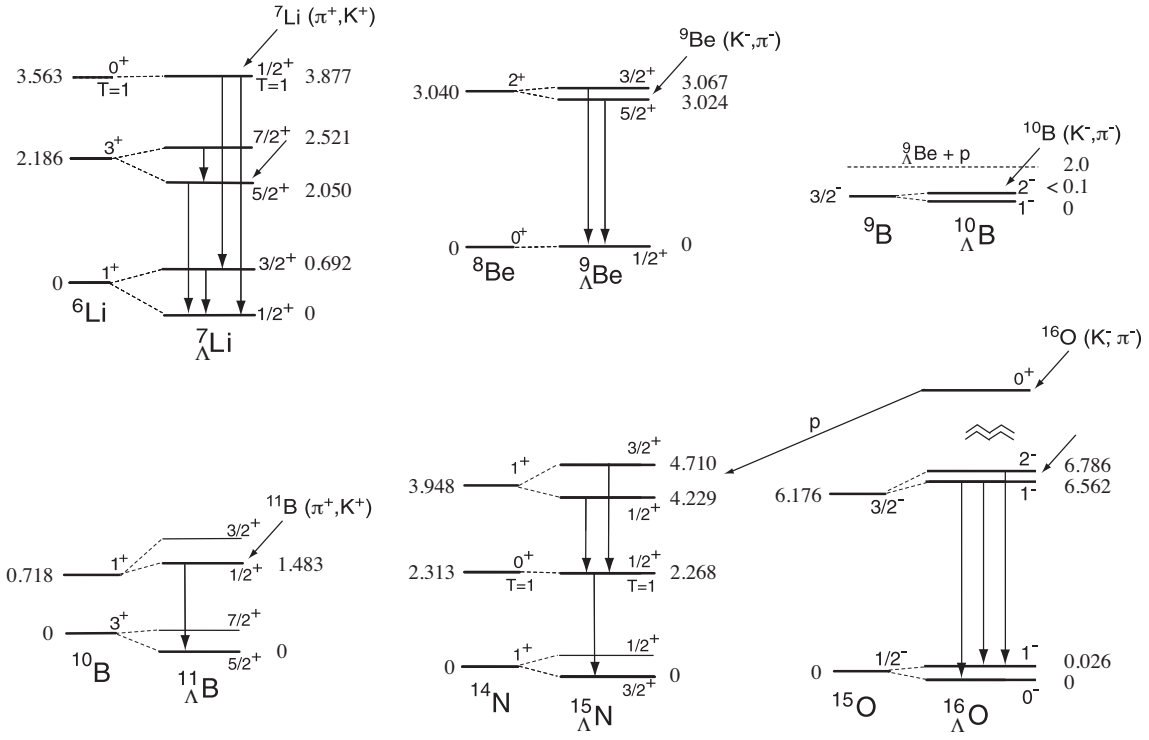

Figure 1.3: Level schemes of ${}^{7}_{\Lambda}$Li, ${}^{9}_{\Lambda}$Be, ${}^{10}_{\Lambda}$B, ${}^{11}_{\Lambda}$B, ${}^{15}_{\Lambda}$N and ${}^{16}_{\Lambda}$O determined from our recent γ-ray spectroscopy experiments with Hyperball. Observed γ transitions and measured level energies (MeV) are indicated. Level schemes of corresponding core nuclei are also shown.

1.2.1 Experimental determination of parameters

From the data accumulated by the Hyperball experiments, each strength of spin-dependent interactions has been experimentally determined [12] as

$$\Delta = 0.43, \;\; S_\Lambda = -0.01, \;\; S_N = -0.39, \;\; T = 0.03 \;\; \text{MeV} \, , \tag{1.2}$$

by focusing on specific hypernuclear energy spacings which are dominantly characterized by each of the parameters.

In the first experiment using Hyperball (KEK E419), the parameters Δ and S_N were determined from the level scheme of the ${}^{7}_{\Lambda}$Li hypernucleus. The energy spacing of the ${}^{7}_{\Lambda}$Li $(3/2^+, 1/2^+)$ spin doublet is ideal for studying the spin-spin interaction strength (Δ) because the ground state of ^{6}Li (1^+) is an almost pure $S = 1$, $L = 0$ state. Thus, the ground-state splitting of ${}^{7}_{\Lambda}$Li is dominated by the spin-spin interaction, and the Δ value can be obtained from their energy spacing. In addition, the effect of ΛN-ΣN coupling is also expected to be small because ${}^{7}_{\Lambda}$Li $(3/2^+, 1/2^+)$ states are isospin singlet. On the other hand, the strength of the N-spin-dependent spin-orbit interaction (S_N) is sensitive to the change of the spacing of the core levels before and after a Λ hyperon is added. Therefore, the S_N value was determined by taking the spin-weighted averages of ${}^{7}_{\Lambda}$Li $(7/2^+, 5/2^+)$ and ${}^{7}_{\Lambda}$Li $(3/2^+, 1/2^+)$ doublets.

In the next experiment at BNL (E930), the parameters S_Λ and T were determined from the level schemes of ${}^{9}_{\Lambda}$Be and ${}^{16}_{\Lambda}$O hypernuclei. The first excited state (2^+) of ^{8}Be core has an almost pure $S = 0$, $L = 2$ configuration, and thus the energy spacing of the ${}^{9}_{\Lambda}$Be doublet $(3/2^+, 5/2^+)$ is governed by the strength of the Λ-spin-dependent spin-orbit interaction (S_Λ). This energy spacing was measured as the energy difference between the two $E2$ transitions ($3/2^+$ or $5/2^+ \to 1/2^+$), and the S_Λ value was derived. At the same time, the strength of the tensor interaction (T) was measured by the ground-state splitting of ${}^{16}_{\Lambda}$O. This is because the ground-state spin-doublet spacings in $p_{1/2}$-shell hypernuclei such as ${}^{16}_{\Lambda}$O $(1^-, 0^-)$ have a large contribution from the tensor interaction while the contribution is small in $p_{3/2}$-shell hypernuclei [10].

1.2.2 Comparison with BB interaction models

The obtained Δ value in the Hyperball experiment is consistent with the value of $\Delta \sim$0.5 MeV estimated from the old experimental data for A=4 hypernuclei [10], where γ-ray spectroscopy with NaI counters was employed. According to this result, it is found that the strength of the spin-spin interaction of the NSC97e, f models is plausible among Nijmegen models. For the T value, the small strength of the tensor

force from 0.02 MeV to 0.05 MeV is predicted by the Nijmegen models [25], and it is also consistent with our result. However, both strengths of the spin-orbit forces (S_Λ and S_N) seem to be explained well by the quark model rather than the meson-exchange model. Considering a short-range nature of the spin-orbit forces, this trend could be expected.

The spin-orbit force can be considered in another formalization, namely the symmetric spin-orbit force (SLS, $\propto \boldsymbol{l}_{N\Lambda}(\boldsymbol{s}_\Lambda + \boldsymbol{s}_N)$) and the antisymmetric spin-orbit force (ALS, $\propto \boldsymbol{l}_{N\Lambda}(\boldsymbol{s}_\Lambda - \boldsymbol{s}_N)$). The ALS term is peculiar to the hyperon-nucleon (YN) interaction because this term does not exist in the case of the NN interaction. The quark model predicts that the ALS component of the YN interaction is strong and almost comparable with the SLS component [26]. On the other hand, the meson-exchange model predicts a much smaller ALS force. In the case of the ΛN interaction, the SLS and ALS components have different signs. Therefore, S_Λ (SLS+ALS) is predicted to be almost zero in the quark model, while a finite value is derived in the meson-exchange model. The very small S_Λ value measured from ${}^{9}_{\Lambda}$Be supports the quark model. The S_N value from ${}^{7}_{\Lambda}$Li also agrees with the quark model prediction.

1.2.3 Inconsistency of parameters

A recent increase of hypernuclear γ-ray data enables us to cross-check whether the obtained parameter set (Eq. 1.2) also explains other hypernuclear level energies and to confirm validity of the present framework. Many of other hypernuclear data are found to be reproduced quite well by this parameter set [12], but for two exceptions of ${}^{10}_{\Lambda}$B $(2^-, 1^-)$ and ${}^{11}_{\Lambda}$B $(1/2^+, 5/2^+)$.

In the case of ${}^{10}_{\Lambda}$B, the γ transition between the ground state doublet $M1(2^- \to 1^-)$ was searched for but not observed in two independent experiments at BNL [27, 21], which gives $E(2^-) - E(1^-) < 100$ keV. This result suggests much smaller Δ value of less than 0.3 MeV, and it is obviously inconsistent with the parameter set (Eq. 1.2). This inconsistency could be resulted from some missing components in the framework of our approach. It is pointed out that the effect of the ΛNN three-body interaction caused by ΛN-ΣN coupling may be a possible source of the inconsistency.

Another inconsistency is found in the level structure of ${}^{11}_{\Lambda}$B measured in KEK-E518. The measured energy spacing between $1/2^+$ and $5/2^+$ states (1482 keV) is quite different from the one expected from the parameter set (Eq. 1.2), 1020 keV [22]. If the difference is ascribed to S_N, it gives $S_N \sim -0.9$ MeV. This ${}^{11}_{\Lambda}$B problem presumably implies that the wavefunction of the core ^{10}B used in the shell-model calculation is not correct because the coefficient for S_N is quite sensitive to the core wavefunction.

1.3 γ-ray spectroscopy via the ^{12}C(π^+, K^+) reaction

The purposes of the γ-ray spectroscopy via the ^{12}C(π^+, K^+) reaction are to experimentally establish the effect of ΛN-ΣN coupling in the p-shell hypernuclei and to accumulate more γ-ray data for further systematic study of the ΛN interaction. When ^{12}C nuclei are irradiated with high-energy pion beams, $^{12}_{\Lambda}$C hypernuclei can be produced via the (π^+, K^+) reaction. In the same reaction, $^{11}_{\Lambda}$B hypernuclei are also populated through one-proton emission from particle-unbound excited states of $^{12}_{\Lambda}$C. Thus, γ rays from both hypernuclei can be detected at the same time. Hypernuclear γ-rays are identified by selecting the mass of hypernuclei in the missing mass spectrum of the ^{12}C(π^+, K^+) reaction.

1.3.1 Motivation of $^{12}_{\Lambda}$C

The spin-doublet spacings of mid-p-shell hypernuclei, in particular $^{10}_{\Lambda}$B and $^{12}_{\Lambda}$C, are suitable subjects for investigating the effect of ΛN-ΣN coupling. This is because their small coefficients for the spin-dependent interactions allow the $\Lambda\Sigma$ value to have a relatively large contribution to the doublet spacings. For example, the contribution is expected to be ~ 30 % for the ground-state doublet spacing of $^{12}_{\Lambda}$C while ~ 10 % for that of $^{7}_{\Lambda}$Li. The effect of ΛN-ΣN coupling qualitatively reduces the excitation energies of hypernuclear states but the actual accounts vary depending on the state configurations. Therefore, the structure of $^{12}_{\Lambda}$C is similar to that of $^{10}_{\Lambda}$B, but the changes of the doublet spacings due to ΛN-ΣN coupling are expected to be opposite as illustrated in Figure 1.4. In the Millener's calculation, their ground-state doublet spacings are expressed as

$$\begin{aligned} {}^{10}_{\Lambda}\mathrm{B}: \quad E(2^-) - E(1^-) &= 0.578\Delta + 1.41S_\Lambda + 0.014S_N - 1.07T + \Lambda\Sigma({}^{10}_{\Lambda}\mathrm{B}) \ , \\ {}^{12}_{\Lambda}\mathrm{C}: \quad E(2^-_1) - E(1^-_1) &= 0.534\Delta + 1.44S_\Lambda + 0.047S_N - 1.72T + \Lambda\Sigma({}^{12}_{\Lambda}\mathrm{C}) \ , \end{aligned}$$

where the coefficients of the four parameters are close to each other. However, the calculated $\Lambda\Sigma$ values have opposite sign as

$$\Lambda\Sigma({}^{10}_{\Lambda}\mathrm{B}) = -0.015 \text{ MeV}, \quad \Lambda\Sigma({}^{12}_{\Lambda}\mathrm{C}) = 0.057 \text{ MeV} \ ,$$

due to opposite signs of the isovector matrix elements for the ^{9}B and the ^{11}C ground states. Using the parameter set (Eq. 1.2), their spacings are predicted to be 182 keV for $^{10}_{\Lambda}$B and 202 keV for $^{12}_{\Lambda}$C. According to this prediction, we can detect the direct spin-flip $M1(2^-_1 \rightarrow 1^-_1)$ transition between the ground state doublet of $^{12}_{\Lambda}$C. Even when the $\Lambda\Sigma(^{12}_{\Lambda}\mathrm{C})$ value have negative sign and would decrease the energy spacing

below the detection limit, we can still obtain the ground-state doublet spacing by measuring the two $M1(1_2^- \to 2_1^-, 1_1^-)$ transitions from the 1_2^- state. This fact is of great advantage to the γ-ray spectroscopy of ${}^{12}_{\Lambda}$C compared with the ${}^{10}_{\Lambda}$B case.

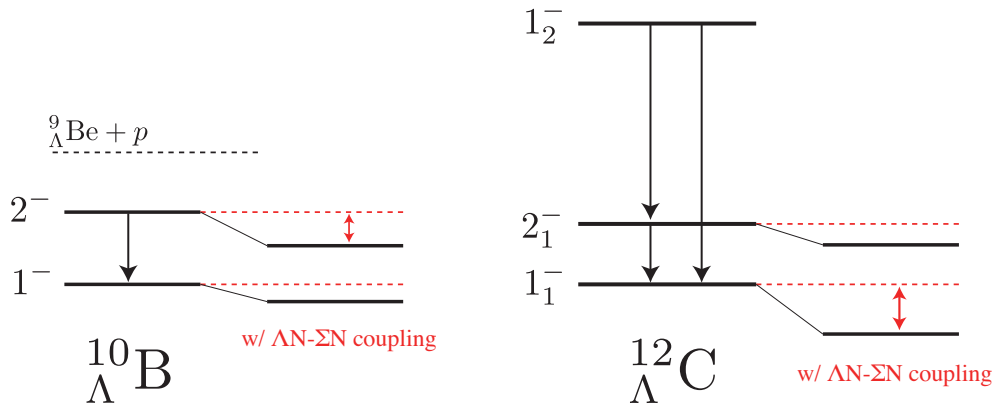

Figure 1.4: Low-lying level schemes of ${}^{10}_{\Lambda}$B and ${}^{12}_{\Lambda}$C. For the ${}^{10}_{\Lambda}$B hypernucleus, only the $M1(2^- \to 1^-)$ transition is allowed because the excitation energies of upper states are higher than that of ${}^{9}_{\Lambda}$Be+p threshold. The energy spacing of the ${}^{10}_{\Lambda}\mathrm{B}(2^-, 1^-)$ doublet decreases with ΛN-ΣN coupling. On the other hand, the ${}^{12}_{\Lambda}\mathrm{C}(2_1^-, 1_1^-)$ spacing increases with ΛN-ΣN coupling.

1.3.2 Motivation of ${}^{11}_{\Lambda}$B

Several γ-ray peaks from ${}^{11}_{\Lambda}$B were observed in the KEK-E518 experiment. However, many of the observed γ rays have not been assigned yet due to complicated structure of ${}^{11}_{\Lambda}$B. In the present experiment, ${}^{11}_{\Lambda}$B is produced via one-proton emission of ${}^{12}_{\Lambda}$C excited states, the excitation energy of which can be measured by the missing mass spectroscopy method. In this case, we may choose a populated state of ${}^{11}_{\Lambda}$B by selecting the excitation energy of ${}^{12}_{\Lambda}$C. In addition, an upgraded Ge detector array, Hyperball2, enables us to use the γ-γ coincidence technique. These features will enhance the ability of hypernuclear level assignment.

1.3.3 Production and expected transitions

The mass spectrum with the scale of Λ binding energy $(-B_\Lambda)$ for the ${}^{12}\mathrm{C}(\pi^+, K^+)$ reaction measured in the past KEK-E369 experiment [36] is shown on the left side in Figure 1.5. The experimental setup of KEK-E369 is almost the same as the present experiment except for the Ge detectors. The two pronounced peaks correspond to the states with the configurations $[(p_{3/2})_n^{-1}, (s_{1/2})_\Lambda]$ 1_1^- and

$[(p_{3/2})_n^{-1}, (p_{3/2,1/2})_\Lambda]$ 2_1^+, 2_2^+, 0_1^+. The three satellite peaks (#2, #3, #4) are assigned as the core-excited states with $[^{11}\mathrm{C}^*(1/2^-) \otimes s_\Lambda]$ 1_2^-, $[^{11}\mathrm{C}^*(3/2^-) \otimes s_\Lambda]$ 1_3^- and $[^{11}\mathrm{C}^*(5/2^+) \otimes s_\Lambda]$ 2^+. The remaining small peak of #6 is also assigned as the core-excited state with $[^{11}\mathrm{C}^*(1/2^-) \otimes p_\Lambda]$ 2_3^+. According to the KEK-E369 results, the level scheme of ${}^{12}_{\Lambda}\mathrm{C}$ is expected as shown in Figure 1.5, where the level scheme of ${}^{11}_{\Lambda}\mathrm{B}$ expected from KEK-E518 results is also shown. The γ-ray transitions expected to be observed in the present experiment are marked as red arrows. Cross sections from DWIA calculations by Itonaga [38] and γ-ray branching ratios calculated by Millener [28] are also shown.

It is remarkable that the 2^+ components of the #5 peak events exclusively decay into ${}^{11}_{\Lambda}\mathrm{B}$ through one-proton emission, where only the ground-state doublet of ${}^{11}_{\Lambda}\mathrm{B}$ are energetically allowed to be produced. This is experimentally confirmed from the KEK-E518 result for the ${}^{11}_{\Lambda}\mathrm{B}(1/2^+, 5/2^+)$ energy spacing (1483 keV) and the old emulsion data for the precise ${}^{12}_{\Lambda}\mathrm{C}(2^+)$ and ${}^{11}_{\Lambda}\mathrm{B}(5/2^+)$ energies [29]. Thus, γ rays from the ${}^{11}_{\Lambda}\mathrm{B}(7/2^+ \to 5/2^+)$ transition are expected to be dominated and identified uniquely when we select the #5 peak events.

The 2_1^- state of ${}^{12}_{\Lambda}\mathrm{C}$ is hardly produced in the (π^+, K^+) reaction because of a small spin-flip amplitude. Thus, γ rays from ${}^{12}_{\Lambda}\mathrm{C}$ should be attributed to the core-excited states (#2, #3, #4) below the ${}^{11}_{\Lambda}\mathrm{B}$+$p$ threshold at $B_\Lambda = -1.55$ MeV [29].

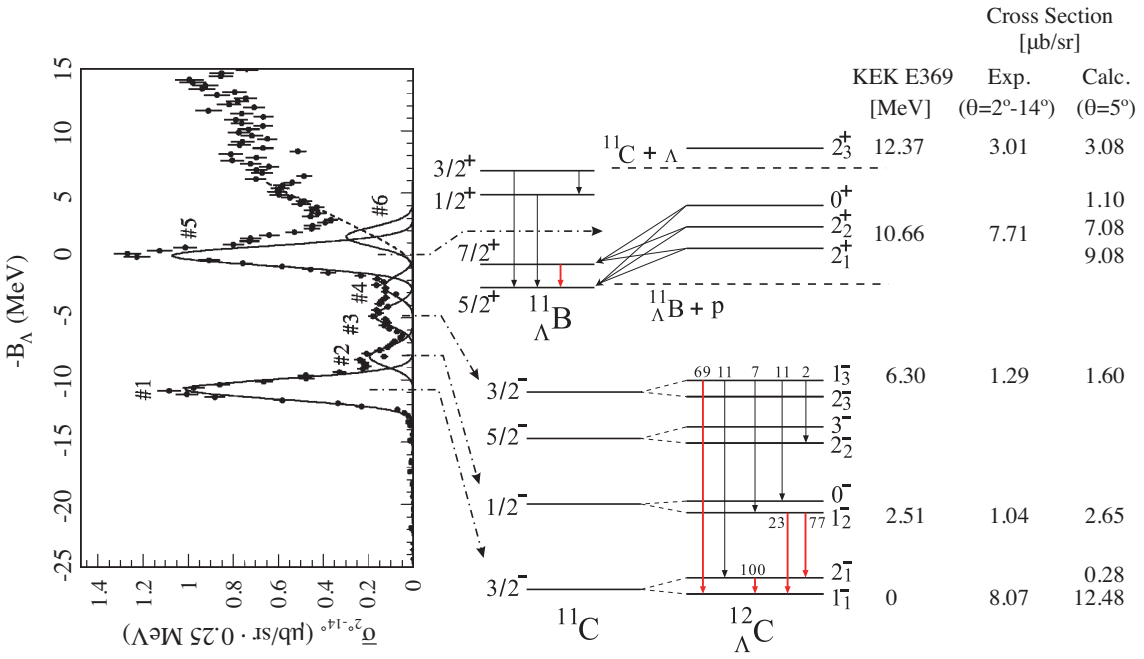

Figure 1.5: Expected level schemes of ${}^{12}_{\Lambda}$C and ${}^{11}_{\Lambda}$B. The left figure is the missing mass spectrum for the ^{12}C(π^+, K^+) reaction taken in the KEK-E369 experiment [36]. The excitation energies and the (π^+, K^+) cross sections are also shown in the right side for experimental values by E369 and for calculated values by Itonaga [38]. γ transitions expected to be observed in the present experiment are shown as red arrows. γ-ray branching ratios calculated by Millener [28] are also shown.

Chapter 2

Experiment

2.1 Overview of the experiment

A γ-ray spectroscopy experiment (KEK-E566) was carried out at the KEK-PS K6 beam line in 2005. We used the ^{12}C(π^+, K^+) reaction to produce $^{11}_{\Lambda}$B and $^{12}_{\Lambda}$C hypernuclei, in which $^{11}_{\Lambda}$B was produced through one proton emission from particle-unbound excited states of $^{12}_{\Lambda}$C. A polyethylene block was used as the ^{12}C target. The momentum of the incident pion was set to be 1.05 GeV/c, at which the cross section of the elemental process, $n(\pi^+, K^+)\Lambda$, has a sharp peak as shown in Figure 2.1. The K6 beam line and Superconducting Kaon Spectrometer (SKS) were employed to obtain a mass spectrum for $^{12}_{\Lambda}$C. A germanium detector array, Hyperball2, was constructed and installed around the experimental target to detect γ rays emitted from hypernuclei in coincidence with the (π^+, K^+) reaction. Through one month beam time, 2×10^{12} pions were irradiated on the target in total.

2.2 KEK-PS and K6 beam line

The primary beam of 1.1×10^{12} protons per spill was accelerated by KEK-PS (Proton Synchrotron) up to the energy of 12 GeV and extracted to the K6 beam line. The duration of the beam extraction was 1.5 second in every 4.0 second of the KEK-PS operation cycle. This duration is called a spill. The K6 beam line is illustrated in Figure 2.2. The extracted primary proton beam was bombarded on a production target located at the most upstream of the K6 beam line and produced secondary particles. The production target was a platinum rod of $\phi 6 \times 60$ mm^2. The secondary beam of positive pion was transported through the magnets from D1 to Q10 and achromatically focused on the experimental target, where the momentum and mass of the beam pions were spatially selected by an electrostatic separator (DC separator)

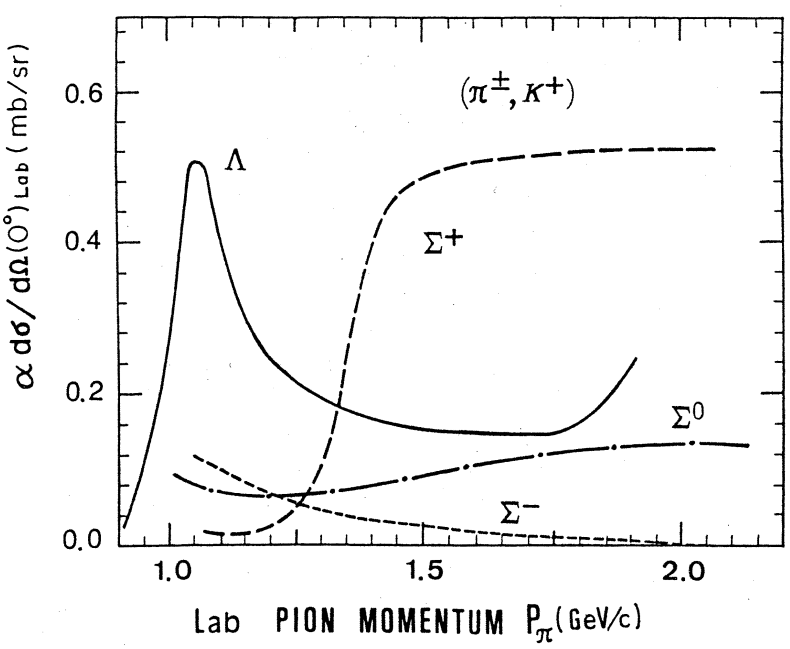

Figure 2.1: The forward lab cross section as a function of the projectile momentum in the $\pi N \to YK^+$ reactions. Taken from Ref. [30].

and a series of slits placed between D1 and Q7. The measured beam size was typically 5.0 mm (horizontal) $\times$ 8.5 mm (vertical) in rms, as shown in Figure 2.3. The size of ^{12}C target was selected large enough to fully cover the profile of the beam. The pion beam intensity at the experimental target was typically 3×10^6/spill for 1.05 GeV/c momentum. The experimental condition of the beam is summarized in Table 2.1, and the specifications of the K6 beam line are summarized in Table 2.2.

Table 2.1: Experimental beam condition.

Primary proton momentum	12 GeV/c
Primary proton intensity	1.1×10^{12}/spill
Repetition cycle	4.0 s
Spill length	1.5 s
Secondary pion momentum	1.05 GeV/c
Secondary pion intensity	3×10^6/spill

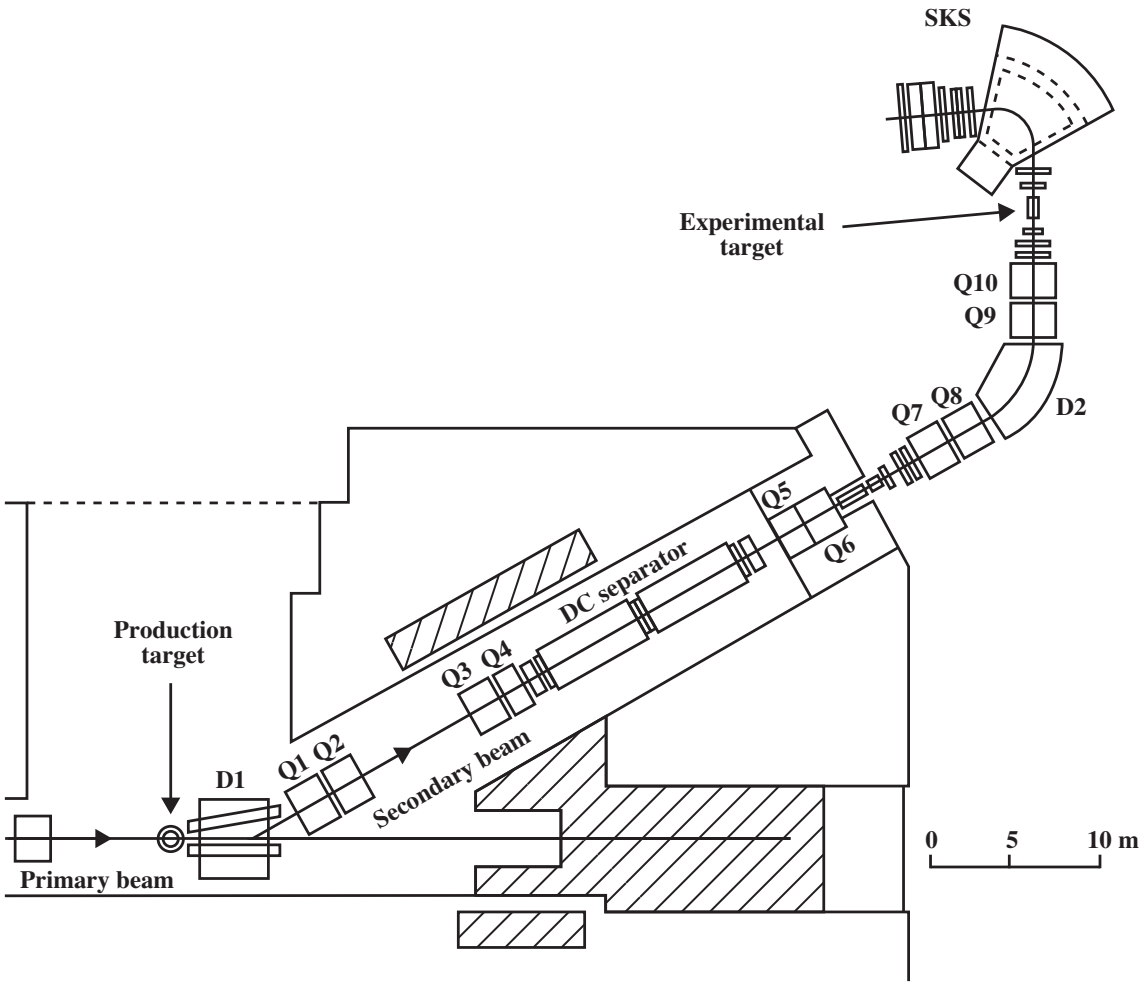

Figure 2.2: A schematic view of the KEK-PS K6 beam line and the experimental area. All detectors except for Hyperball2 are shown.

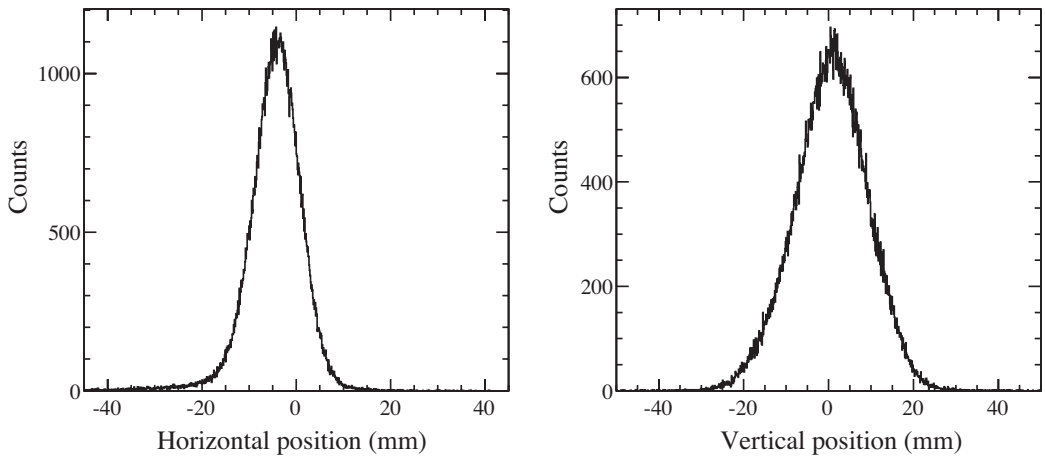

Figure 2.3: Typical beam profile at the experimental target.

Table 2.2: Specifications of the K6 beam line.

Momentum range	0.5 - 2.0 GeV/c
Momentum bite	±3 %
Momentum resolution	0.1 % (FWHM)
Beam line length	30 m

2.3 Spectrometer system

2.3.1 Beam spectrometer

The end part of the K6 beam line was used as a spectrometer for beam particles in order to identify particles and to analyze the momentum. Figure 2.4 shows a schematic view of the beam spectrometer. The beam spectrometer consists of QQDQQ magnets, four sets of drift chambers (BDC1,2,3 and 4) and three sets of trigger counters (GC, BH1 and BH2). For the momentum reconstruction, a third-order transfer matrix was used. In order to minimize the multiple scattering effect on the momentum resolution, the $\langle x|\theta\rangle$ term of the transport matrix was tuned to be zero. In addition, the beam pipe in QQDQQ magnets was evacuated with a Kapton window of 100 μm thickness, and the tracking chambers were also made as thin as possible. The designed momentum resolution of the beam spectrometer was 0.1 % (FWHM) at 1.0 GeV/c [31].

Trigger counters

Three sets of trigger counters (GC, BH1, BH2) were used for particle identification at the trigger level. Positrons and protons were the main contaminations in the beam at the entrance of the beam spectrometer. Fractions of these particles were about 20 % for positrons and 10 % for protons. The contamination of positive kaon was negligible because of its short life time. Specifications of these counters are listed in Table 2.3

The Freon-gas Čherenkov counter (GC) was installed at the most upstream part of the beam spectrometer. The positron contamination was rejected by this counter with a rejection efficiency better than 99 %.

BH1 and BH2 were plastic scintillation counters. BH1 was segmented into seven parts and BH2 was segmented into four parts in order to reduce the counting rate. BH1 was located just downstream of GC and BH2 was installed at 40-cm upstream of the experimental target. By requiring the time difference between BH1 and BH2, the

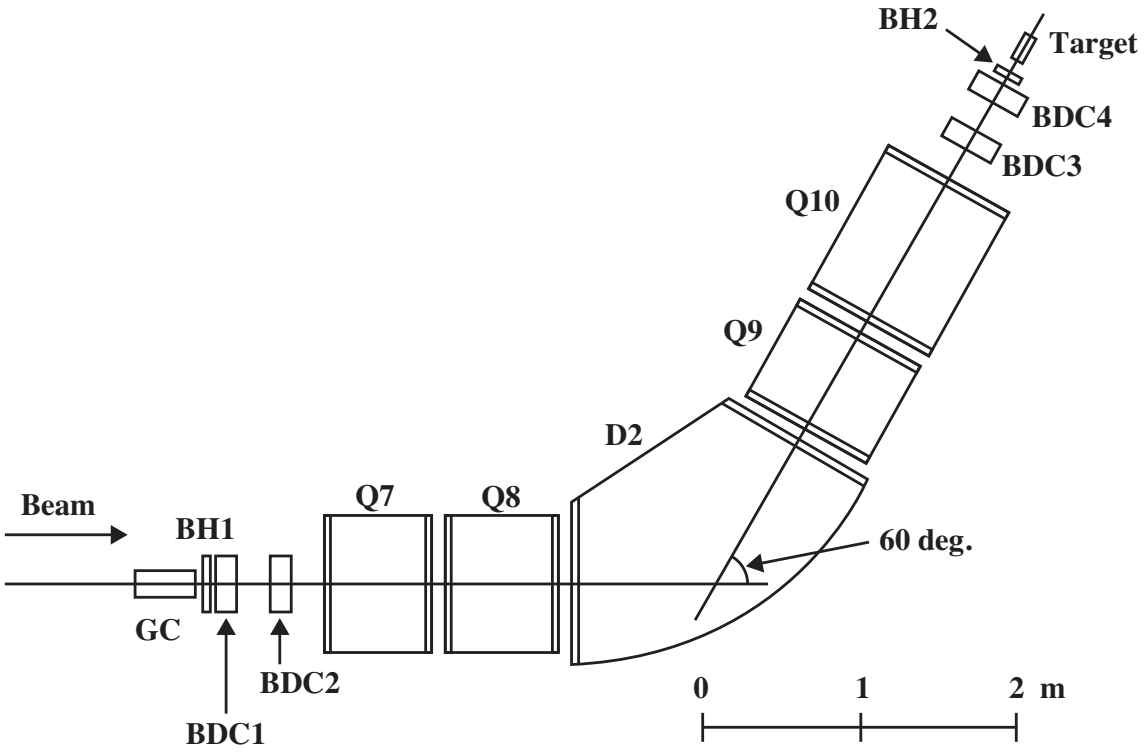

Figure 2.4: A schematic view of the beam spectrometer

proton contamination was rejected as well as other background particles which could not pass through the beam spectrometer. BH2 also served as a time zero counter for the whole system.

Drift chambers

Four sets of drift chambers (BDC1,2,3 and 4) were used to measure the particle tracks. The momentum of each beam pion was determined by the track information from these chambers in the off-line analysis. BDC1 and BDC2 were placed upstream of the QQDQQ magnets, and BDC3 and BDC4 were placed downstream of these magnets. The specifications of these chambers are summarized in Table 2.4. The BDC chambers had the same structure which was composed of the six layers of sense-wire plane ($xx'uu'vv'$). x, u or v denotes a vertical wire plane or a wire plane tilted by ± 15 degree, respectively. In order to solve left-right ambiguities, sense-wire positions were shifted by a drift length of 2.5 mm in each pair of (xx'), (uu') and (vv') planes.

Table 2.3: Specifications of trigger counters.

Name	Sensitive area (cm)	Radiator	etc.
Beam spectrometer			
GC	$\phi 20 \times 29^L$	Freon-12 (2.2 atm)	n=1.00245
BH1	$19^W \times 9^H \times 0.5^T$	Plastic scintillator	7 segments
BH2	$9.4^W \times 4^H \times 0.6^T$	Plastic scintillator	4 segments
SKS			
TOF	$105^W \times 100^H \times 3^T$	Plastic scintillator	15 segments
AC1	$105^W \times 120^H \times 9^T$	Aerogel	n=1.06
AC2	$140^W \times 140^H \times 12^T$	Aerogel	n=1.06
LC	$140^W \times 140^H \times 4^T$	Lucite	14 segments, n=1.49

Table 2.4: Specifications of drift chambers.

Name	Sensitive area (cm)	Drift length (mm)	Layers	Resolution (μm in rms)
Beam spectrometer				
BDC1	$24^W \times 15^H$	2.5	$xx'uu'vv'$	300
BDC2	$24^W \times 15^H$	2.5	$xx'uu'vv'$	300
BDC3	$24^W \times 15^H$	2.5	$xx'uu'vv'$	300
BDC4	$24^W \times 15^H$	2.5	$xx'uu'vv'$	300
SKS				
SDC1	$24^W \times 15^H$	2.5	$uu'vv'$	300
SDC2	$40^W \times 15^H$	2.5	$xx'uu'vv'$	300
SDC3	$100^W \times 100^H$	21	$xx'yy'$	300
SDC4X	$100^W \times 100^H$	21	$x \times 6$	300
SDC4Y	$100^W \times 100^H$	21	$y \times 6$	300

2.3.2 Superconducting Kaon Spectrometer

The particles going to downstream of the experimental target were identified and momentum analyzed by Superconducting Kaon Spectrometer (SKS). SKS was designed for a mass spectroscopy of Λ hypernuclei via the (π^+, K^+) reaction [31]. The concept of SKS was to have a good momentum resolution of 0.1 % together with a large acceptance of 100 msr at around 1 GeV/c. The flight path was also kept as short as 5 m for the central trajectory in order to minimize the kaon decay loss at the exit of SKS. These characteristic features allow us to efficiently tag hypernuclear production events, which is the most important for hypernuclear γ-ray spectroscopy. The specifications of SKS are summarized in Table 2.5.

As shown in Figure 2.5, SKS was composed of a superconducting dipole magnet, four sets of drift chambers (SDC1,2,3 and 4) and three kinds of trigger counters (TOF, AC, LC). The momentum of the scattered particle was measured via the off-line analysis by reconstructing a trajectory with the Runge-Kutta method using a magnetic filed map. The magnetic filed map was calculated by ANSYS code. In the experiment, SKS magnet was excited at 2.2 T (272 A), where the central trajectory corresponded to 0.72 GeV/c. This momentum is typical for kaons produced in the ^{12}C(π^+, K^+) reaction with a 1.05 GeV/c beam.

Table 2.5: Specifications of SKS.

Maximum central momentum	1.1 GeV/c
Momentum bite	$\pm$10 %
Momentum resolution	0.1 % (FWHM) at 720 MeV/c
Bending angle	100 deg. for the central trajectory
Magnetic field	2.2 T for central momentum of 720 GeV/c
Solid angle	100 msr
Flight path	5 m for the central trajectory

Trigger counters

The three kinds of counters (TOF, AC, LC) were used in order to make trigger logic to identify scatted particles such as pions, kaons and protons. TOF is sensitive to charged particles, AC is sensitive only to pions, and LC is insensitive to protons. The specifications of those trigger counters are listed in Table 2.3.

TOF was made of fifteen segments of plastic scintillator, located just behind

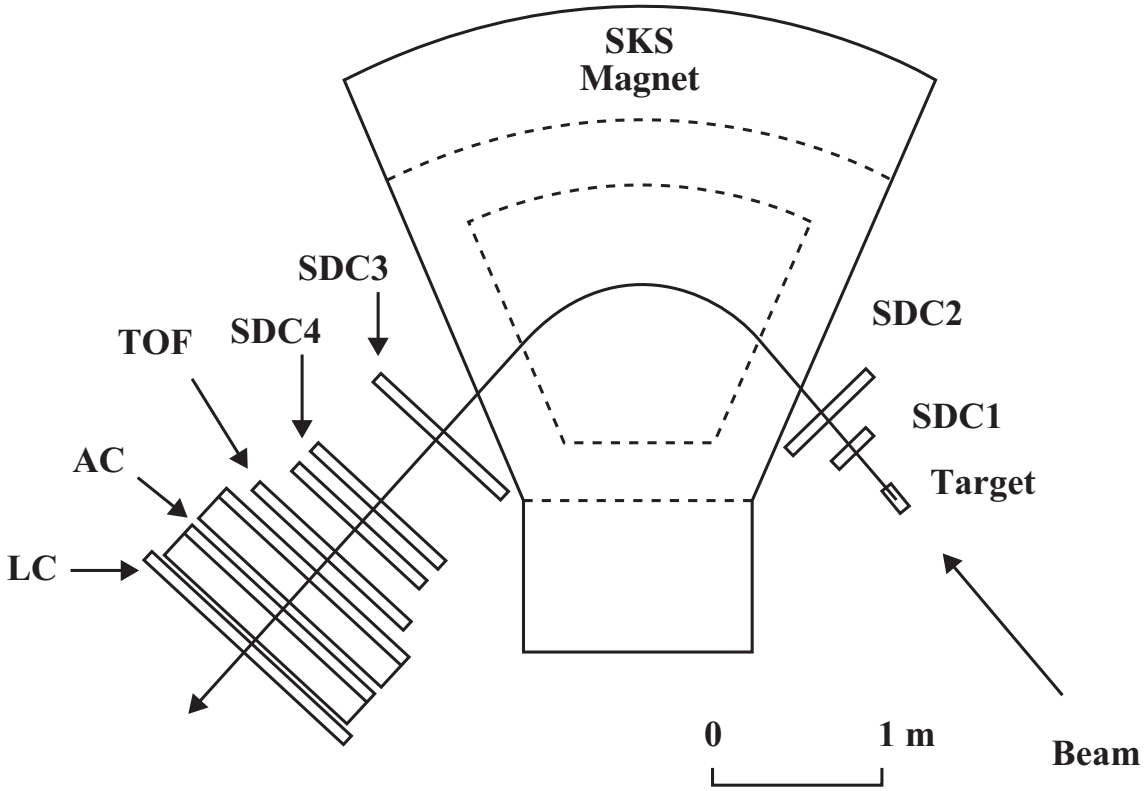

Figure 2.5: A schematic view of SKS

SDC4. The time-of-flight information between BH2 and TOF was used for selecting kaons from contaminating pions and protons in the off-line analysis.

AC consisted of two sets (AC1 and AC2) of aerogel Čherenkov counters, placed downstream of TOF. The radiator in AC was silica aerogel of 1.06 refractive index, which corresponded to threshold momenta of 0.4 GeV/c for pions and 1.8 GeV/c for kaons. Pions were rejected at the trigger level by anti-coincidence with this counter.

LC was the most downstream counter in SKS. It was composed of fourteen segments of Lucite Čherenkov counters. The refractive index of Lucite was 1.49 corresponding to threshold momenta of 0.13 GeV/c for pions, 0.45 GeV/c for kaons, and 0.85 GeV/c for protons. Proton contaminations in the kaons were vetoed by requiring a hit in LC.

Drift chambers

The specifications of the SKS drift chambers are listed in Table 2.4. The SDC1 and SDC2 were placed at the entrance of the SKS magnet. The same cell structure of 2.5-mm drift length as BDC chambers was adopted because they were also exposed to the beam. SDC1 had four layers of the sense-wire plane ($uu'vv'$) and SDC2 had

six layers of the sense-wire plane ($xx'uu'vv'$).

SDC3 and SDC4 were installed at the exit of the SKS magnet. They had a large drift length of 21 mm because of lower counting rates than the upstream chambers. The sensitive area of these chambers was large enough to fully cover the wide angular and momentum acceptance of SKS. SDC3 had four layers of the sense-wire plane ($xx'yy'$), where y denotes a horizontal wire plane. In order to solve left-right ambiguities, sense-wire positions of SDC3 were also shifted by a drift length in each pair of (xx') and (yy') planes. SDC4 was composed of SDC4X and SDC4Y, where SDC4X had six layers of x plane and SDC4Y had six layers of y plane.

2.4 Targets

Two types of carbon materials were used as the ^{12}C target. The main experimental target was polyethylene with a density of 0.955 g/cm^3. The dimensions of the polyethylene target was ϕ50 mm $\times$ 200^L mm, which corresponded to the mass thickness of 19.1 g/cm^2. Graphite with a density of 1.7 g/cm^3 was also used as a reference target in order to confirm reproducibility of the mass spectrum by comparing with the previous SKS experiment. The dimensions of the graphite target were ϕ50 mm $\times$ 20^L mm. Figure 2.6 illustrates the targets.

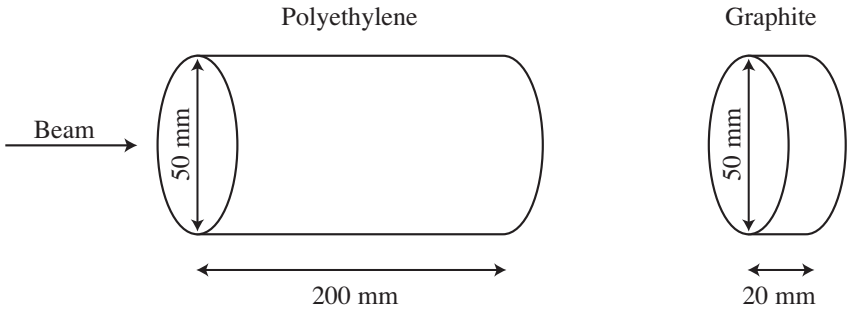

Figure 2.6: Schematic view of the ^{12}C targets.

2.5 Hyperball2

A new germanium (Ge) detector array called Hyperball2 was constructed and used in this experiment. It was installed around the experimental target. For Hyperball2, six clover-type Ge detectors were added to the previous Ge detector array, Hyperball [15], made of fourteen single-type Ge detectors in order to increase the detector efficiency. Each of the Ge detectors was surrounded by BGO scintillation counters to suppress background signals mainly caused by Compton scattering. In order to monitor the in-beam performance, Hyperball2 was equipped with an efficient monitoring system using ^{60}Co sources.

Figure 2.7 shows the configuration of Hyperball2. The upstream ring consisted of six single-type detectors, which were vertically titled by 27 degree. The downstream ring was also composed of six single-type detectors, which were vertically titled by -27 degree. Two single-type detectors and six clover-type detectors were installed in the middle ring. Typical distance between the target center and the surface of the Ge detectors was about 15 cm. Hyperball2 covered about 25 % of the full solid angle around the target.

2.5.1 Ge detectors

The single-type Ge detector had a high-purity, n-type germanium crystal with a typical size of $\phi 70 \times 70^L$ mm^3. The clover-type Ge detector was a composite detector consisting of four pieces of high-purity, n-type germanium crystal with a typical size of $41 \times 41 \times 71^L$ mm^3. Their relative efficiencies with respect to a 3"$\phi \times 3$" NaI(Tl) counter were ~ 60 % for the single-type detector and ~ 20 % for each crystal in the clover-type detector. By taking the sum of energies in the four crystals, a clover-type detector as a whole had a relative efficiency of ~ 120 %, which is known as the add-back effect [32].

Reset-type preamplifier

All of the Ge detectors were equipped with transistor-reset type preamplifiers to tolerate the ultra-high energy deposits rate condition. In a hypernuclear γ-ray spectroscopy, Ge detectors are exposed to high-energy particles which originate in beam halo and scattering in the target. The energy deposit of a charged particle is of the order of 50 MeV and is extremely large compared to the energy of nuclear γ rays. The reset-type preamplifier operates in this high-deposit-rate condition while the resistive-feedback type does not. A dead time of 20 or 30 μs, however, was made after each reset which occurred in every 150-MeV deposit.

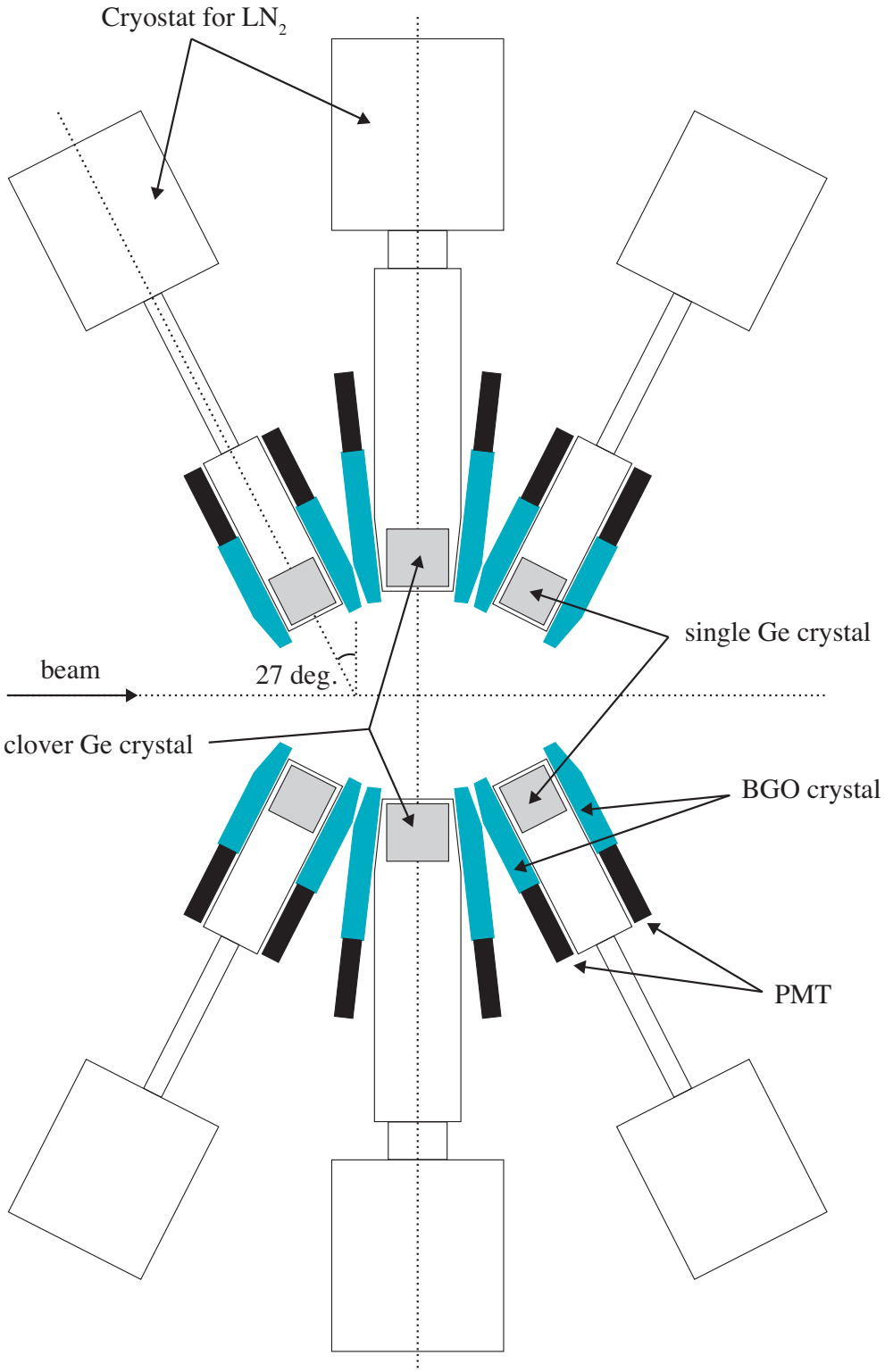

Figure 2.7: A cross sectional view of Hyperball2

Readout electronics

The readout electronics connected to the preamplifier were also specialized for the high counting rate condition. In the readout of energy, the Ultra-High-rate Amplifier (ORTEC 973U) was used for the main amplifier, the dead time of which due to a pulse pileup was 6 μs. The output signals from 973U were digitalized by a peak-sensitive ADC (Analog-to-Digital Converter) with 13 bit resolution (ORTEC AD413A). The time information of the Ge detectors was digitized by multi-hit TDC (Time-to-Digital Converter, LeCroy 3377) after the signal was processed through a fast shaping amplifier (ORTEC 579) and a constant fraction discriminator (ORTEC 934).

2.5.2 BGO counters

The germanium crystal of each Ge detector was surrounded by scintillation counters to suppress background events, where Compton scattering, high-energy γ rays from π^0 decay and high energy charged particles penetrating the Ge crystal were dominant. Bismuth germinate ($Bi_4Ge_3O_{12}$) crystal was used for the background suppression counters. The characteristic features of BGO crystal are a large density of 7.31 g/cm^3 and large effective mass number of 75, which enable efficiently suppression for background γ rays.

The configurations of the combined detector unit are illustrated in Figure 2.8. The single-type Ge detectors was surrounded by six pieces of the BGO counters and the clover-type Ge detector was surrounded by twelve pieces of the BGO counters. The combination of the Ge and BGO detectors for the background suppression logic scheme is summarized in Table 2.6.

Table 2.6: The crystal combination for background suppression.

Ge crystal	BGO crystal
single-type	any of six
clover-type 1	1, 2, 11, 12
clover-type 2	2, 3, 4, 5
clover-type 3	5, 6, 7, 8
clover-type 4	8, 9, 10, 11

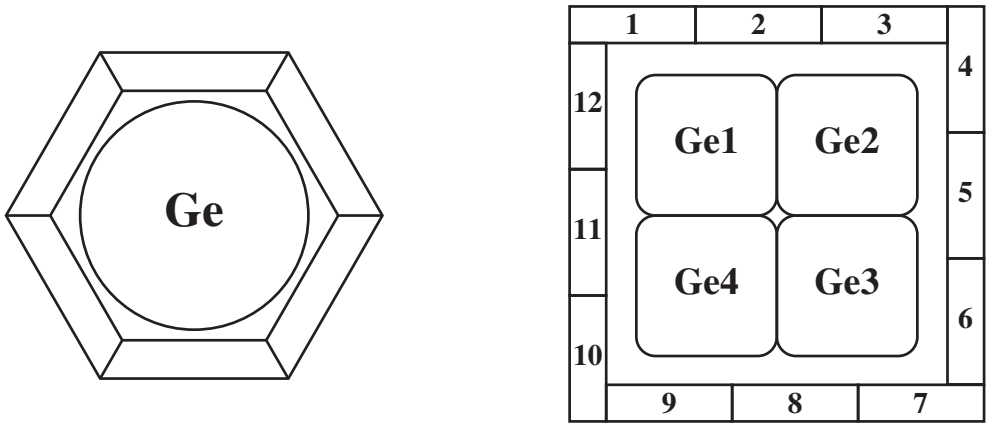

Figure 2.8: Configurations of the Ge detector and BGO counters.

2.5.3 ^{60}Co pulsers

A plastic scintillation counter embedded with a ^{60}Co source, called a ^{60}Co pulser, was installed close to each of the Ge detectors. The ^{60}Co pulser provided a timing signal for γ-ray emission from ^{60}Co by detecting β rays with the plastic scintillator. By taking a coincidence between the ^{60}Co pulser and the corresponded Ge detector, we were able to accumulate ^{60}Co γ-ray events efficiently even in the in-beam period. The observed peaks (1.17 MeV and 1.33 MeV) were used to monitor the performance of the Ge detectors during the beam time.

Figure 2.9 shows a typical γ-ray spectrum obtained by the ^{60}Co pulser trigger, where whole hits of the Ge detectors are filled including the add-back data of the clover-type detectors. The energy resolution of Hyperball2 was measured to be 5.4 keV (FWHM) at 1.33 MeV during the in-beam period and to be 5.1 keV (FWHM) during the off-beam period. The in-beam live time of Hyperball2 was measured to be ~ 60 % by comparing the ^{60}Co γ-ray yields in each period, where the DAQ dead time was included. A peak-position shift of ~ 1 keV to the lower energy side was also observed during the in-beam period.

2.6 Trigger and data acquisition system

Trigger

The main background in the (π^+, K^+) trigger came from pion-nucleus reactions, such as (π^+, p)X and (π^+, π^+)X, whose cross sections were typically two or three orders of

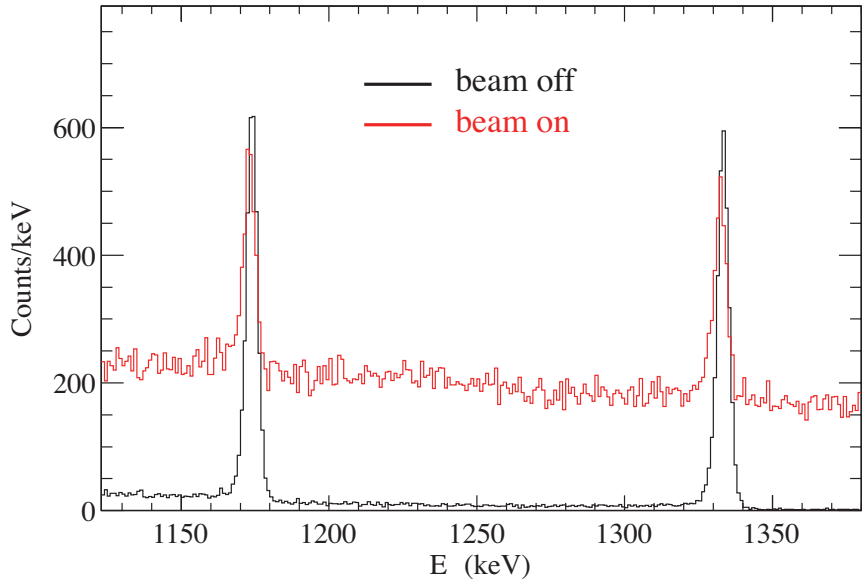

Figure 2.9: A γ-ray spectrum obtained by Hyperball2 with the ^{60}Co pulser trigger during the off-beam or in-beam period.

magnitude larger than that for the (π^+, K^+) reaction. The K6 beam line and SKS were equipped with an excellent trigger system in order to tag the (π^+, K^+) reaction efficiently.

The π^+ beam trigger was defined as

$$\mathrm{BEAM} = \overline{\mathrm{GC}} \times \mathrm{BH1} \times \mathrm{BH2} \ .$$

The positron contamination was rejected by taking anti-coincidence of GC. The contaminating protons were rejected by using time difference between BH1 and BH2, where the difference of time-of-flight between pions and kaons was about 10 ns at 1.05 GeV/c.

The (π^+, π^+) trigger was defined as

$$\mathrm{PIPI} = \mathrm{BEAM} \times \mathrm{TOF} \times \mathrm{AC} \times \mathrm{LC} \ ,$$

which was used to calibrate positions and time offsets of detectors.

The (π^+, K^+) trigger was defined as

$$\mathrm{PIK} = \mathrm{BEAM} \times \mathrm{TOF} \times \overline{\mathrm{AC}} \times \mathrm{LC} \ .$$

The contaminating (π^+, π^+) triggers were suppressed with anti-coincidence of AC. The (π^+, p) contamination was also reduced by requiring a hit on LC. The remaining

contamination was rejected in the off-line analysis based on the time-of-flight between BH2 and TOF and the momentum measured by SKS.

Data acquisition system

Two types of VME memory modules were used for accumulating the data from the detectors. To reduce the dead time of readout, the data stored in these memories were transported to the computer only in the off-beam period. All the data sent to the computer were recorded on a DVD-RAM.

A VME memory called UMEM (Universal Memory Module) was used to store the data from Ge detectors via the FERA bus. Another VME memory called SMP (Symmetric Memory Partner) was used to acquire the data from other detectors via the TKO bus.

2.7 Data summary

The total beam time we used for the experiment was about 650 hours. Irradiated pions on the main target of polyethylene counted 2×10^{12} in total. We also took reference data without target and with graphite target. The data acquired in the experiment are summarized in Table 2.7.

Table 2.7: Total number of pions irradiated on each target.

Target	thickness (g/cm^2)	number of pions
Carbon (polyethylene)	19.1	2×10^{12}
Carbon (graphite)	3.4	8×10^{9}
Empty	–	8×10^{4}

Chapter 3

Analysis I – the (π^+, K^+) reaction

The data analysis can be separated into two parts, namely the analysis of the magnetic spectrometers and the analysis of the Ge detectors. The analysis of the K6 beam spectrometer and the SKS spectrometer is described in this chapter. The goal of this part is to obtain a missing mass spectrum for the (π^+, K^+) reaction. The analysis of Hyperball2 is described in the next chapter.

3.1 Outline

For each of the K6 beam spectrometer and the SKS spectrometer, a local track of the entering particle into the spectrometer is determined by analyzing the set of the chambers installed at the entrance of the spectrometer. A local track for the outgoing particle is similarly obtained from the set of the downstream chambers. By connecting those two local tracks through the magnetic field of the spectrometer, the momentum and trajectory of the passing particle are determined. The momentum vector at the target position of a incident pion is measured by the beam spectrometer and that of a scattered kaon is measured by SKS. Then, the mass of a produced hypernucleus ($M_{\rm HY}$) is obtained as a missing mass in the (π^+, K^+) reaction by calculating the following equation in the laboratory frame

$$M_{HY} = \sqrt{(E_\pi + M_{target} - E_K)^2 - (p_\pi^2 + p_K^2 - 2p_\pi p_K \cos\theta_{\pi K})} \ ,$$

where E_π and p_π are the energy and the momentum of the pion, E_K and p_K are those of the kaon, M_{target} is the mass of the target nucleus (^{12}C), and $\theta_{\pi K}$ is the angle between the measured two vectors. The missing mass can be converted to the

binding energy (B_Λ) of a Λ hyperon in the hypernucleus as

$$B_\Lambda = M_{core} + M_\Lambda - M_{HY} \ ,$$

where M_{core} is the mass of the core nucleus (^{11}C) and M_Λ is the mass of a Λ hyperon. In the analysis for missing mass, particle identification is essential for obtaining background-free spectra, because a large portion of the data belongs to background even though the data were taken with the PIK trigger. The analysis procedures of the missing mass reconstruction are described in the following sections.

3.2 Analysis of incident particles

3.2.1 Momentum reconstruction of the beam spectrometer

The beam momentum vector was reconstructed from the data of the beam line drift chambers (BDC1,2,3 and 4), where each of the chambers had six layers of wire plane. A local straight track entering into the beam spectrometer was found from BDC1 and BDC2 by the least χ^2 fitting method. Outgoing tracks at the exit of the spectrometer were also found from BDC3 and BDC4 in the same way. In the local track search, tracks with minimized χ^2 values of more than 100 were rejected as fake tracks. If two or more tracks were found at both sides of the spectrometer, K6 track connection was tried to each combination of those local tracks with a 3rd-order transport matrix calculated by the ORBIT code [33]. The momentum of a K6 track was determined by minimizing the following χ^2 value. For multi-track events, only one combination with the least χ^2 was selected. The χ^2 value for the K6 track is defined as

$$\begin{aligned}
\chi^2_{Beam} &\equiv \frac{1}{n-5}\left(\sum_{i=1}^{12} H_i \left(\frac{P_i - f_i(\vec{X}_{in})}{w_i}\right)^2 + \sum_{i=13}^{24} H_i \left(\frac{P_i - g_i(\vec{X}_{out})}{w_i}\right)^2\right) \\
n &= \sum_{i=1}^{24} H_i \quad \begin{cases} H_i = 1 & \text{if } i\text{th layer has a hit in the local track.} \\ H_i = 0 & \text{if } i\text{th layer has no hit in the local track.} \end{cases} \\
\vec{X}_{out} &= M(\vec{X}_{in}, \delta) \ ,
\end{aligned}$$

where P_i and w_i denote the measured hit position and resolution of the ith layer. The hit position calculated by the transport matrix at the ith layer is represented by $f_i(\vec{X}_{in})$ and $g_i(\vec{X}_{out})$, where $\vec{X}$ means the calculated local track. In this analysis, $\vec{X}$ is expressed by four parameters as (x, y, $\frac{dx}{dz}$, $\frac{dy}{dz}$). The momentum is denoted

by $p = p_0(1 + \delta)$, where p_0 is the central momentum. The operator M denotes the transport matrix which connects $\vec{X}_{in}$ and $\vec{X}_{out}$. Figure 3.1 show a typical χ^2 distribution in the beam spectrometer tracking. The χ^2 region of less than 20 was accepted as good events. Figure 3.2 shows a momentum distribution for beam pions.

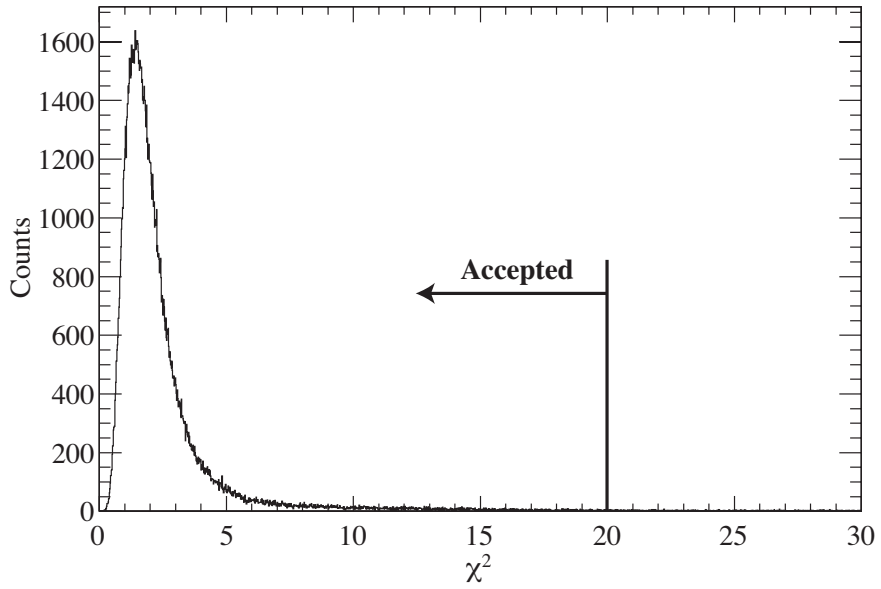

Figure 3.1: Typical χ^2 distribution in the beam spectrometer tracking. Events with $\chi^2 < 20$ were accepted as good tracks.

3.2.2 Selection of π^+

An incident pion was identified by using the time-of-flight between BH1 and BH2, both of which had horizontally segmented scintillators. Hit segments which the local track did not pass through were rejected in the analysis. Figure 3.3 shows the time-of-flight spectrum for the beam particles, where the horizontal axis is defined for the timing of pions to be zero. In order to remove accidental coincidence background and kaon contamination in the beam, we applied a cut to the spectrum. The selected region for incident pions was -1.5 ns < Beam TOF < 1.5 ns as shown in the figure.

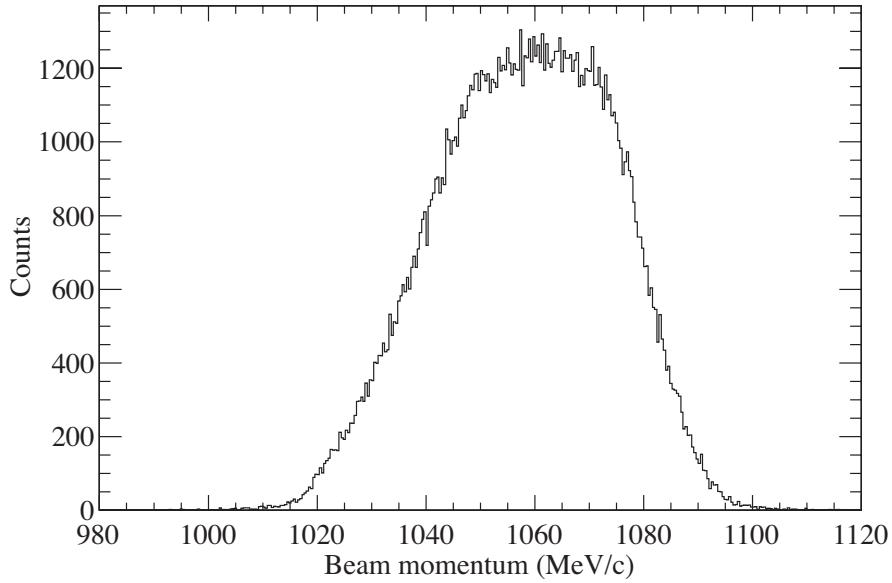

Figure 3.2: Momentum distribution measured by the beam spectrometer. The beam momentum was set to be 1.05 GeV/c.

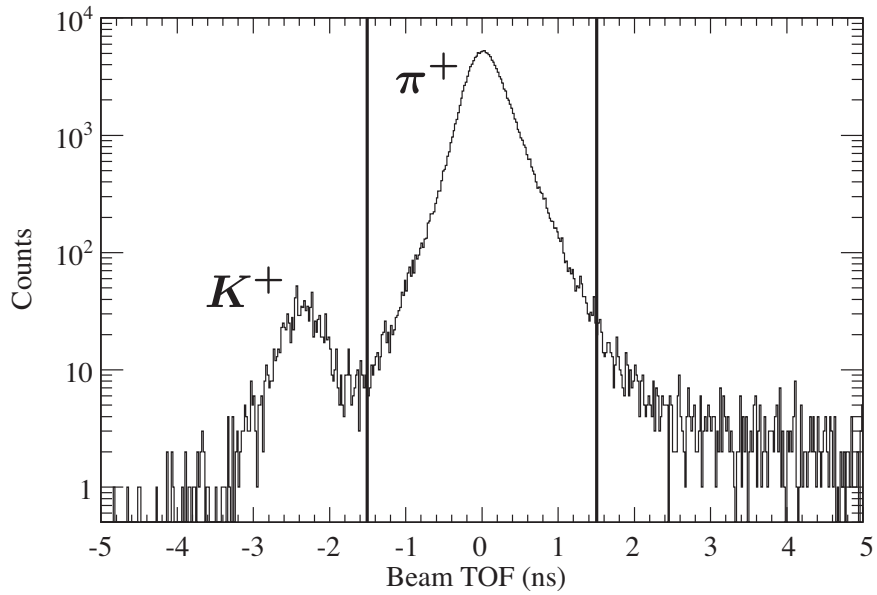

Figure 3.3: Time-of-flight distribution between BH1 and BH2. Events in the region enclosed by the solid lines were selected as pions.

3.3 Analysis of scattered particles

3.3.1 Momentum reconstruction of SKS

The momentum vector of a scattered particle was reconstructed from the data of the SKS drift chambers (SDC1,2,3 and 4). A local straight track entering into SKS was founded from SDC1 and SDC2 by the least χ^2 fitting method. Outgoing tracks at the exit of SKS were also found from SDC3 and SDC4 in the same way. In the local track search, tracks with minimized χ^2 values of more than 100 were rejected as fake ones. If two or more tracks were found at both sides of the SKS magnet, track connection was tried for each combination of those local tracks. The Runge-Kutta method [34] was used for reconstructing SKS trajectories using a magnetic field map. The magnetic field map was calculated by ANSYS code with the finite element method. The trajectory and the momentum were optimized by minimizing the following χ^2 values iteratively. For multi-track events, only one combination with the least χ^2 value was chosen. The χ^2 value of each trajectory is defined as

$$\chi^2_{SKS} \equiv \frac{1}{n-5}\sum_{i=1}^{n}\left(\frac{x_i^{tracking}-x_i^{data}}{w_i}\right)^2,$$

where x_i^{data} and w_i denote the measured hit position and the special resolution of the ith layer, and n is the number of layers having hits. $x_i^{tracking}$ is the calculated hit position on the ith layer in the track reconstruction. Figure 3.4 show a typical χ^2 distribution in the SKS tracking, where one can see a long tail due to decay-in-flight events of kaons. The χ^2 region of less than 30 was accepted as good events in this analysis. Figure 3.5 shows a momentum distribution for scattered kaons with the polyethylene target after we applied particle identification as described in the next section. By comparing with a typical outgoing momentum of 720 MeV/c in the $^{12}\mathrm{C}(\pi^+, K^+)$ reaction, it is clear that the momentum of the scattered kaon was largely shifted to the lower side due to the energy loss in the target.

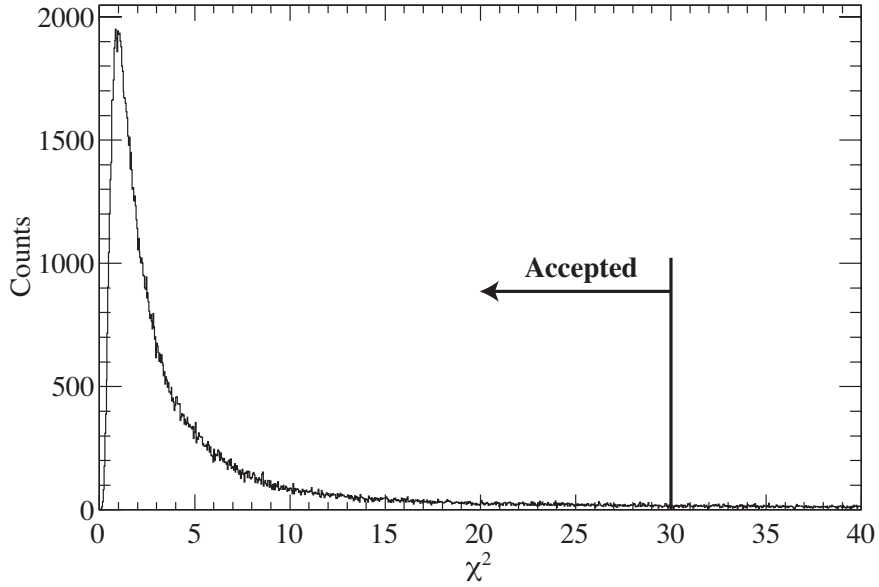

Figure 3.4: Typical χ^2 distribution in the SKS tracking. Events with $\chi^2 < 30$ were accepted as good tracks.

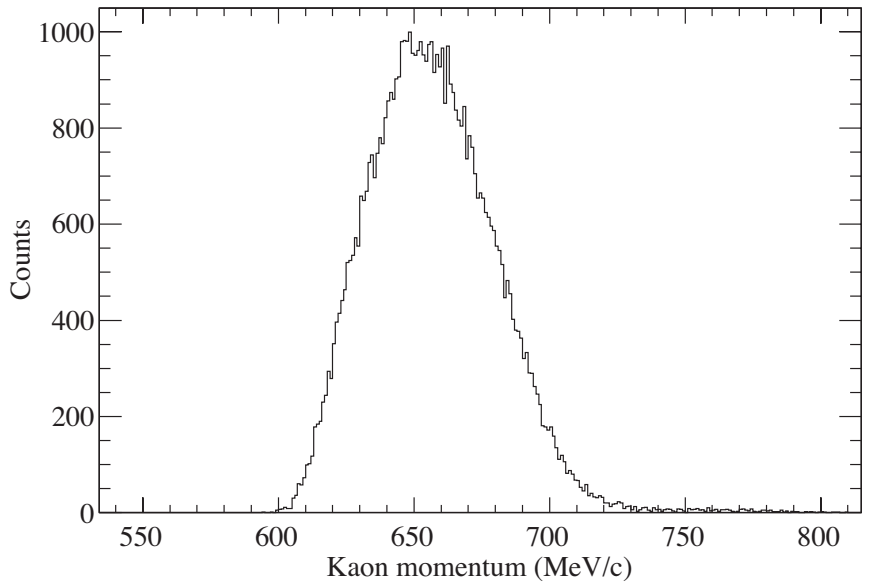

Figure 3.5: Momentum distribution for scattered kaons with the polyethylene target measured by SKS. Kaons were identified by the mass square calculated from the SKS tracking.

3.3.2 Selection of K^+

The contaminating (π^+, π^+)X and (π^+, p)X background events in the PIK trigger were rejected in this stage. After the SKS tracking, one can calculate the mass of the scattered particle (M_{scat}) by using the following formula

$$M_{scat} = \frac{p}{\beta}\sqrt{1-\beta^2}\ ,$$

where p and β are the momentum and velocity of the scattered particle. β was determined from the time-of-flight between BH2 and TOF, and the trajectory length from the target to TOF calculated by the SKS tracking analysis. The time-of-flight was analyzed only if the measured SKS trajectory passed through the hit segment of the TOF counters. Figure 3.6 shows a mass spectrum for scattered particles in the scale of mass square. We selected the region of 390 MeV $< M_{scat} <$ 590 MeV for the scattered kaon events as illustrated in the figure.

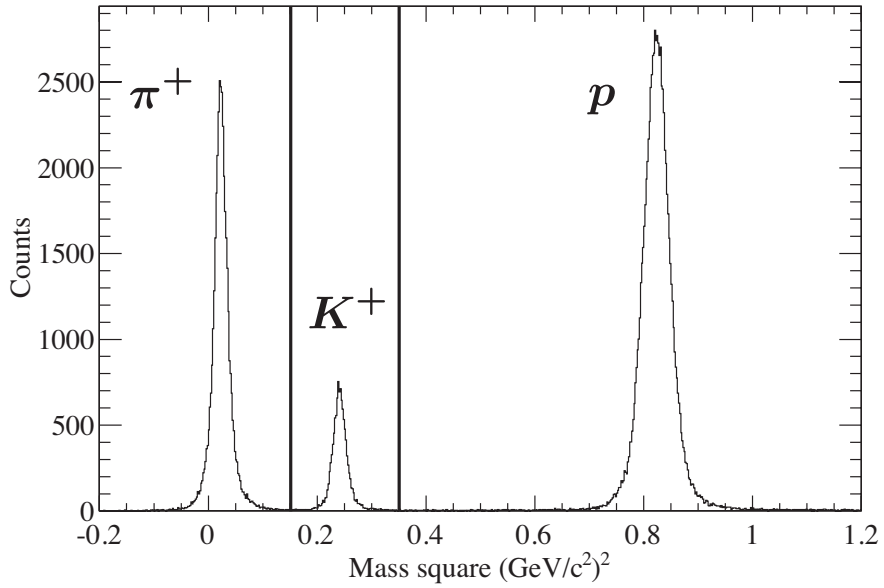

Figure 3.6: Mass square distribution of scattered particles. No event preselection was done before the SKS tracking. Scattered kaons were clearly identified from this distribution.

3.4 Reconstruction of reaction vertex

The reaction angle and the vertex point were determined from both incident beam and scattered particle vectors at the target region. In this analysis, the incident beam vector was a straight extension from a local track obtained by the BDC3,4 tracking. On the other hand, the trajectory obtained from the SKS tracking was used to determine the scattered kaon vector at the target position because of the magnetic fringing field at the SDC1,2 position. Figure 3.7 shows a distribution of the reaction angle for the ^{12}C(π^+, K^+) events. The resolution of the reaction angle was estimated to be 1.5 degree (FWHM) with a simulation, where multiple scattering inside the polyethylene target was considered.

The reaction vertex point was determined by taking a spatially closest point between the incident pion and the scattered kaon vectors. Figure 3.8 shows a distribution of the (π^+, K^+) vertex position projected to the Z axis, where the Z axis is defined as the beam direction. The polyethylene target regain and events occurred in BH2 counter are illustrated in the figure. The center of the z-vertex was consistent with the surveyed target position and the target size was well reproduced. However, some events spread beyond the target region due to inaccuracy of z-vertex. The z-vertex resolution was roughly estimated by a simulation to be about 3.5 cm (FWHM) in total, though it was a function of the reaction angle.

In order to select (π^+, K^+) events from the experimental target, we applied two types of cut to the z-vertex. Figure 3.9 shows contour plots of z-vertex versus reaction angle obtained from the data or a simulation. Firstly, events with reaction angles lower than 2 degree were rejected because of its poor z-vertex resolution. Secondly, events from BH2 counter were removed by using a cut gate as a function of reaction angle. The cut conditions were determined based on a simulation, for which resolutions of momentum vectors and the effect of multiple scattering inside the target volume were taken into account. Details of the simulation are described in the last part of this chapter.

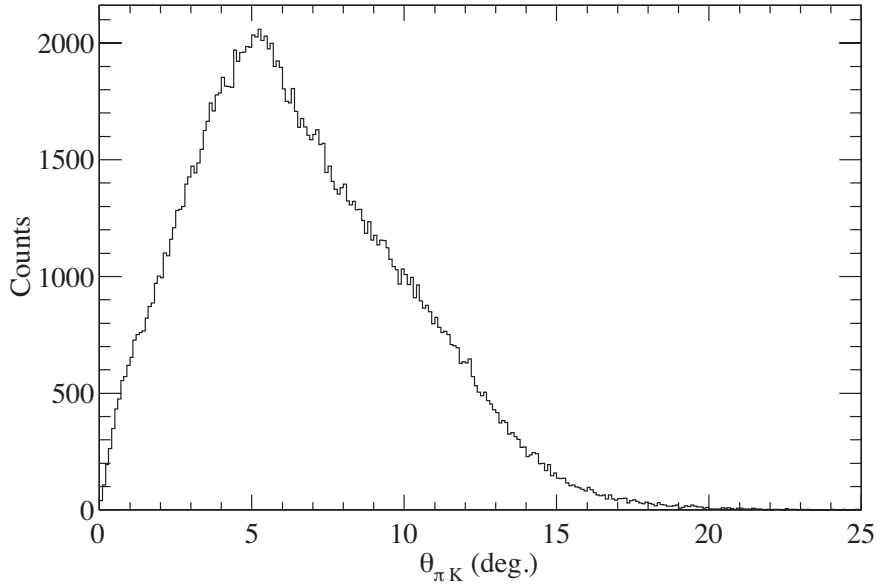

Figure 3.7: Typical distribution of $\theta_{\pi K}$ in the $^{12}\mathrm{C}(\pi^+, K^+)$ reaction. $\theta_{\pi K}$ is defined as the angle between the momentum vector of a beam and that of a scattered kaon in the laboratory frame.

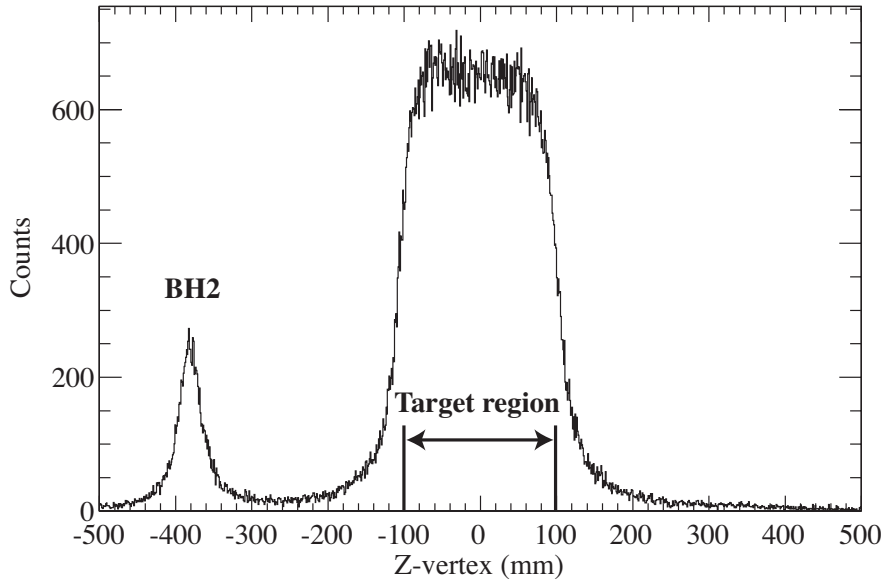

Figure 3.8: A distribution of event vertex position projected to the beam axis. The position of the BH2 counter and the region for the polyethylene target are illustrated.

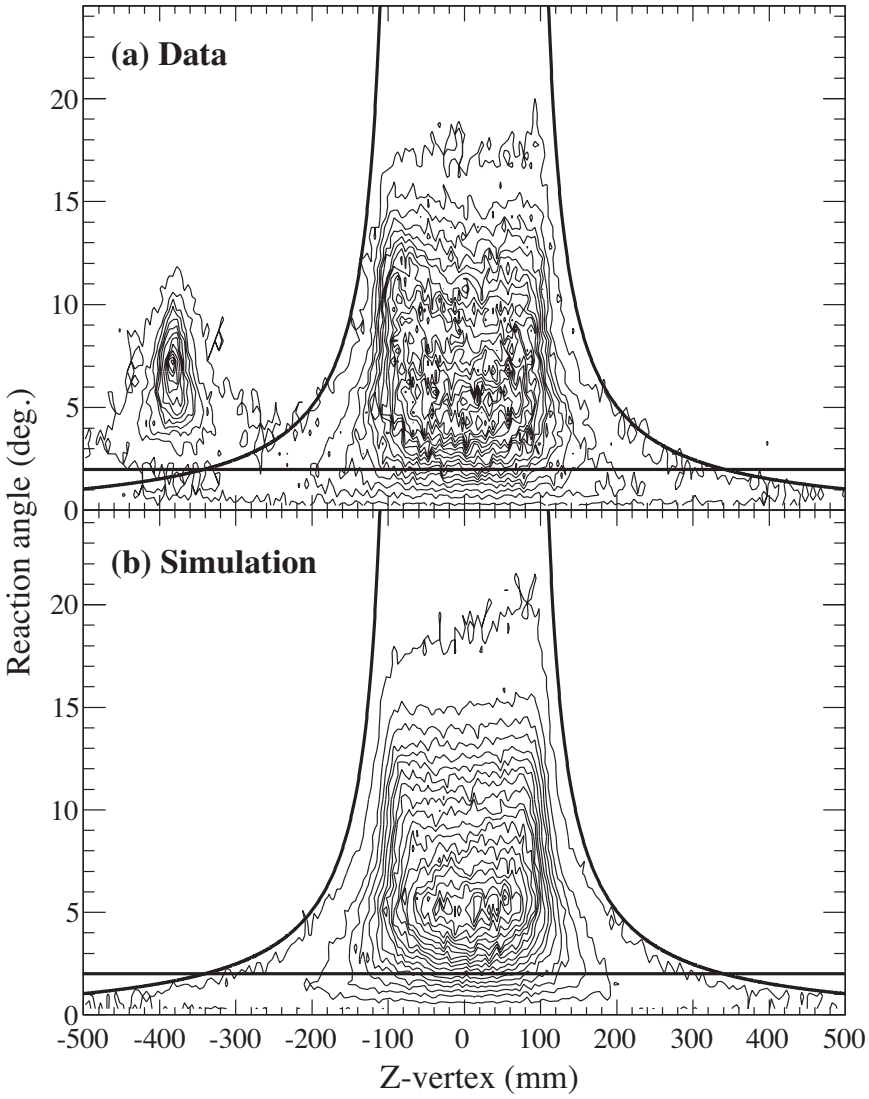

Figure 3.9: Contour plots of z-vertex versus angle in the (π^+, K^+) reaction. A distribution from the experimental data (a) and that from a simulation (b) are shown. The cut conditions represented by solid lines were determined from the simulated distribution.

3.5 Analysis of missing mass

3.5.1 Momentum correction

Before obtaining missing mass spectra, two types of correction were necessary for the momenta of pions and kaons determined in the previous sections. Firstly, we should correct for the systematic derivations of the measured kaon momentum caused by uncertainty of the calculated magnetic field and measured positions of the drift chambers. Secondly, energy loss in the target and detectors was also taken into consideration for both particles.

Horizontal angle dependence

Figure 3.10 (a) shows a scatter plot between the Λ binding energy and dx/dz of scattered kaons for the $^{12}\mathrm{C}(\pi^+, K^+)$ data taken with the reference graphite target. The dx/dz denotes the scattering angle projected to the horizontal plane. If no correction was applied, one can see a strong correlation between the binding energy and horizontal scattering angle. This correlation was removed by introducing a phenomenological correction to the measured kaon momentum as

$$p_K^{\mathrm{corrected}} = p_K^{\mathrm{measured}} + a\left(\frac{dx}{dz}\right) + b\left(\frac{dx}{dz}\right)^2,$$

where a and b are correction parameters. The parameters were taken to be 11.6 MeV/c for a and 16.1 MeV/c for b in this analysis. In the optimization of the parameters, we compared the measured kaon momentum with the calculated kaon momentum by solving the kinematics of the $^{12}_{\Lambda}\mathrm{C}$ ground state production, where the measured momentum of incident pion and reaction angle were the inputs. The scatter plot after the correction is also shown in (b) of Figure 3.10.

Energy loss in the target

The momentum of a pion measured at the beam spectrometer decreased before the reaction by passing through BH2 counter and some part of the target. The momentum of a kaon just after the reaction also decreased due to the target before it was measured by SKS. These effects should be taken into account in order to calibrate the energy scale of the missing mass spectra. In particular for the polyethylene target, an event-by-event energy loss correction inside its volume is necessary because the 20-cm length was longer than the z-vertex resolution.

We used GEANT4 code to estimate energy loss. For a beam pion, the energy loss

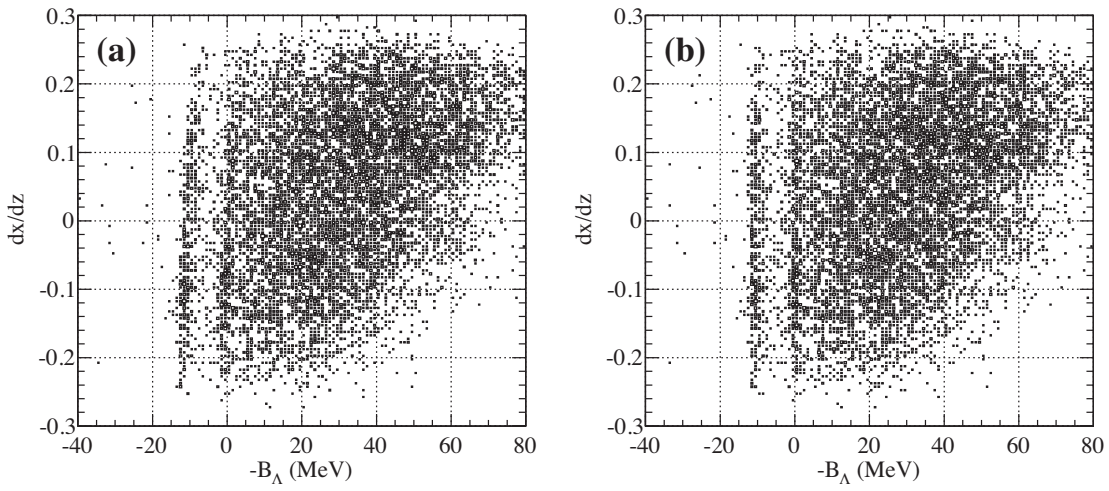

Figure 3.10: Scatter plots between the Λ binding energy and dx/dz of scattered kaons for the reference graphite (3.4g/cm^2) data, where dx/dz is the derivative of the horizontal position at the target. The figures without (a) and with (b) the correction for the SKS momentum are shown.

was calculated to be 1.08 MeV for BH2 and 1.88 MeV/cm in polyethylene, where variations of loss were negligible around 1.05 GeV/c momentum. On the contrary, the energy loss for a scattered kaon in the target differed more than 10 % in the momentum range from 0.6 to 0.8 GeV/c as shown in Figure 3.11. Therefore, modification of kaon's energy loss along the path length inside the target was also taken into account in the correction. The flight path length inside the target was calculated for both particles by using the measured momentum vectors and the reaction point.

Calibration of the absolute scale

Even after applying those momentum corrections, we observed about 3-MeV shift of the energy scale in the missing mass spectra. Because we had no data to calibrate the absolute scale, an arbitrary correction for the kaon momentum was applied additionally so as to adjust the binding energy of the $^{12}_{\Lambda}$C ground state at 10.76 MeV. This value was measured in the old emulsion experiments [35], where the B_Λ values of ground state hypernuclei were determined exclusively from π^--mesonic decays. This arbitrary correction makes uncertainty in the Doppler shift correction of γ rays. However, the effect is found to be negligible as discussed in the next chapter.

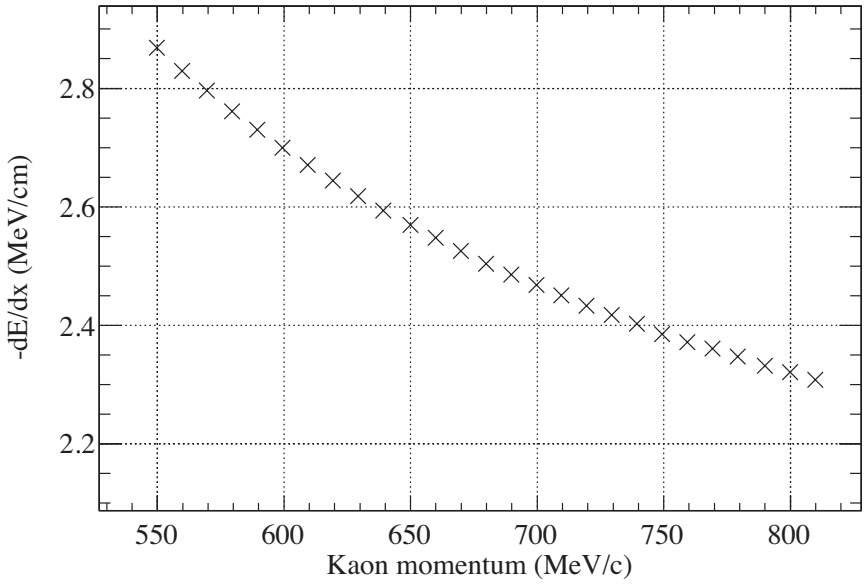

Figure 3.11: Energy loss rate for kaons in the 0.955 g/cm^3-dense polyethylene calculated by GEANT4 code. The momentum range for scattered kaons are expected to be from 600 MeV to 750 MeV.

3.5.2 Mass spectra of $^{12}_{\Lambda}$C

The mass spectra for $^{12}_{\Lambda}$C obtained in the KEK-E566 experiment are presented in this section. In order to interpret the structure of the $^{12}_{\Lambda}$C missing mass spectra, we used cross sections and binding energies measured in the KEK-E369 experiment [36], which were previously performed with the same conditions but with a thin graphite target of 0.86 g/cm^2. The $^{12}_{\Lambda}$C peaks observed in the missing mass spectrum in the KEK-E369 experiment is summarized in Table 3.1. The peaks from #1 to #4 are interpreted as the s_Λ states with a Λ hyperon in the s orbit, while #5 and #6 belong to the p_Λ states with a Λ hyperon in the p orbit. Response functions for the mass spectra in our experiment with the thick target were simulated by using GEANT4 code, where the peak positions and the relative intensities were fixed to the values listed in Table 3.1. As a result of the simulation, asymmetry of the peak shape is expected due to the Landau tail of energy loss process. The details of the simulation analysis are described in the next section.

Table 3.1: The peaks observed in the $^{12}_{\Lambda}$C mass spectrum via the (π^+, K^+) reaction obtained in the KEK-E369 experiment [36].

Peaks	Main component	B_Λ (MeV)	Cross sections (μb/sr)
#1	1^-_1	10.76	8.07
#2	1^-_2	8.25	1.04
#3	1^-_3	4.46	1.29
#4	2^+	2.70	0.99
#5	2^+_1, 2^+_2, 0^+_1	0.10	7.71
#6	2^+_3	-1.61	3.01

Graphite target

The missing mass spectrum obtained with the reference target of graphite is presented in Figure 3.12 (a). By using the simulated response function, we successfully confirmed reproducibility of the ${}^{12}_{\Lambda}$C mass spectrum in this experiment. The simulated peak shape for s_Λ states and that for p_Λ states are illustrated in the figure. The mass resolution was estimated to be 2.2 MeV (FWHM) with the simulation. An energy shift of +1.6 MeV at the ground state was corrected for by subtracting an arbitrary offset from the kaon momentum. The yield of the ground state was obtained to be 406 ± 15 counts by fitting with the response function. This spectrum corresponds to the irradiation of the 3.4 g/cm^2-thick graphite target with 8×10^9 pions.

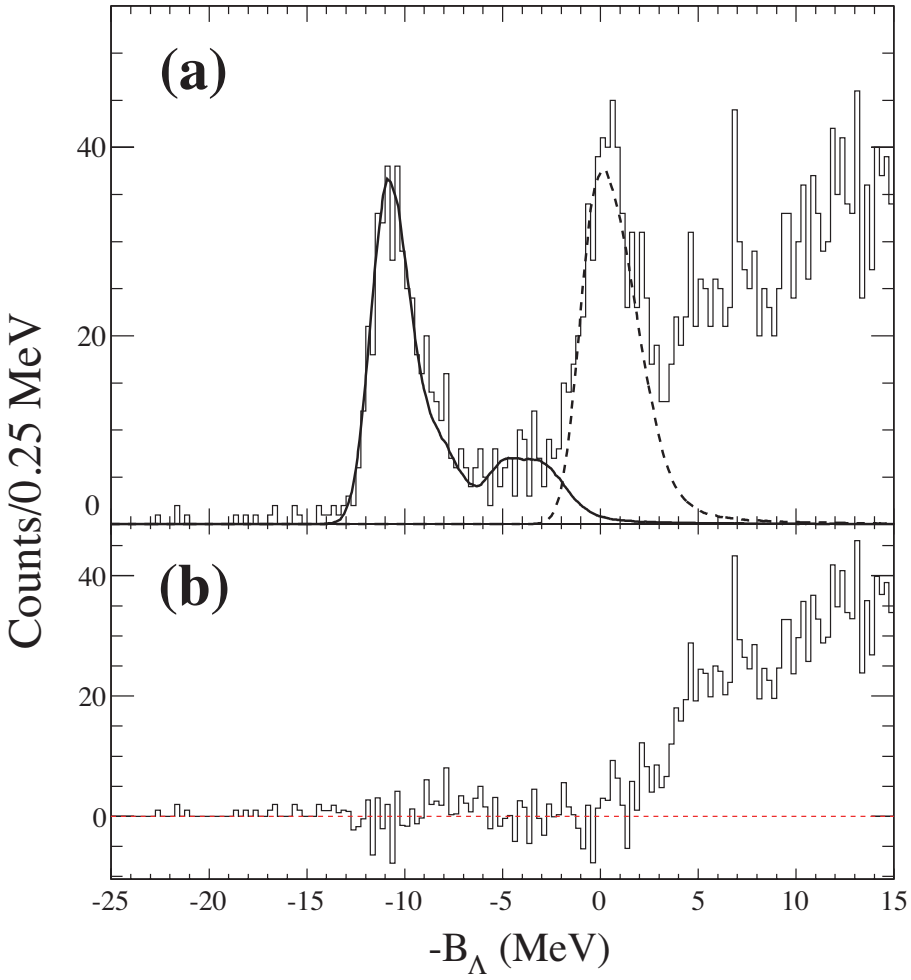

Figure 3.12: (a): Mass spectrum for ${}^{12}_{\Lambda}$C obtained with the reference target of graphite. The horizontal axis is the binding energy of Λ. Simulated spectra are illustrated by the solid line for s_Λ states and the dashed line for p_Λ states. (b): Peak subtracted mass spectrum.

Polyethylene target

Figure 3.13 (a) shows the mass spectrum for the main target of polyethylene, where a solid line for s_Λ states and a dashed line for p_Λ states are also illustrated. The peak shapes were well reproduced even though the mass thickness of the main target was about five times lager than that of the reference target. However, we are not able to separate each peak clearly because of a deteriorated mass resolution. The mass resolution was estimated to be 6.0 MeV (FWHM) with the simulation. An energy shift of +2.9 MeV at the ground state was corrected for by subtracting an arbitrary offset from the kaon momentum. The total yield of the ground state with the polyethylene target was obtained to be 1.58×10^5 counts by fitting with the response function.

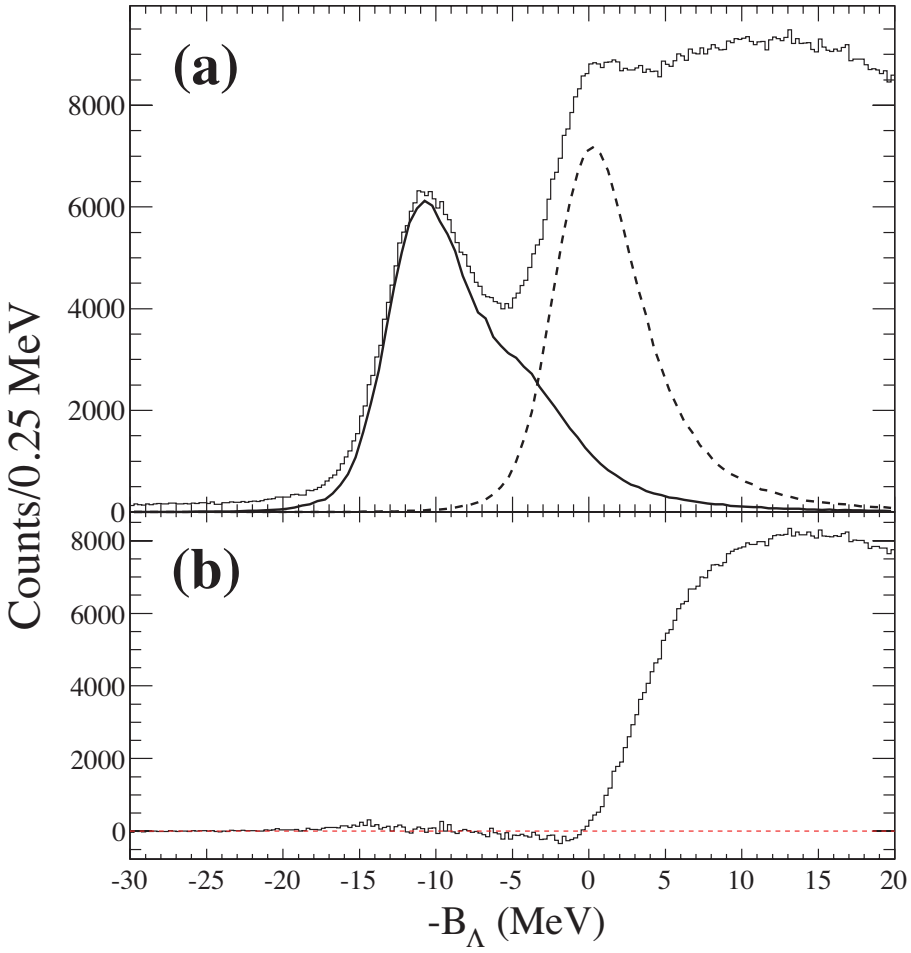

Figure 3.13: (a): Mass spectrum for $^{12}_{\Lambda}$C obtained with the main target of polyethylene. The horizontal axis is the binding energy of Λ. Simulated spectra are illustrated by the solid line for s_Λ states and the dashed line for p_Λ states. (b): Peak subtracted mass spectrum.

3.6 Performance of spectrometers

The details of the simulation analysis for the ${}^{12}_{\Lambda}\mathrm{C}(\pi^+, K^+)$ reaction are described in this section. We used GEANT4 code for a Monte-Carlo simulation.

Performance of the spectrometers was studied in order to estimate missing mass resolution in the experiment. Intrinsic spectrometer resolutions of momentum and vertex point were evaluated from the empty-target data, where the momentum of beam pions was set to be 0.72 GeV/c so that they pass through both spectrometers. Based on these results, we reproduced a missing mass spectrum for the ${}^{12}_{\Lambda}\mathrm{C}$ ground state in a virtual experiment. In fact, the performance of the spectrometers was found to be good enough when we considered the effect of energy struggling inside the target.

In the same way, the velocity of a recoiling hypernucleus was evaluated for the Doppler-shift correction in the γ ray analysis. We also studied the effective solid angle and the tracking efficiency of SKS in order to evaluate the acceptance for scattered kaons.

3.6.1 Missing mass resolution

Momentum resolution

Momentum resolutions of both spectrometers were studied by using the empty-target data, where 0.72 GeV/c beam pions passed through from BH1 to LC. Figure 3.14 shows a distribution of momentum difference between the beam spectrometer and SKS, where the difference is defined by $\Delta p = p_{K6} - p_{SKS}$. The width of the distribution gives the total momentum resolution of the two spectrometers but we have no data to decompose it. Therefore, we assumed that both spectrometers had the same momentum resolution. The width of the momentum difference was measured to be 0.22 % (FWHM) at 0.72 GeV/c and the momentum resolution of each spectrometer was estimated to be 0.15 % (FWHM). The momentum dependence of the resolution for each spectrometer was studied in detail by H. Hotchi [37] and found to be negligibly small.

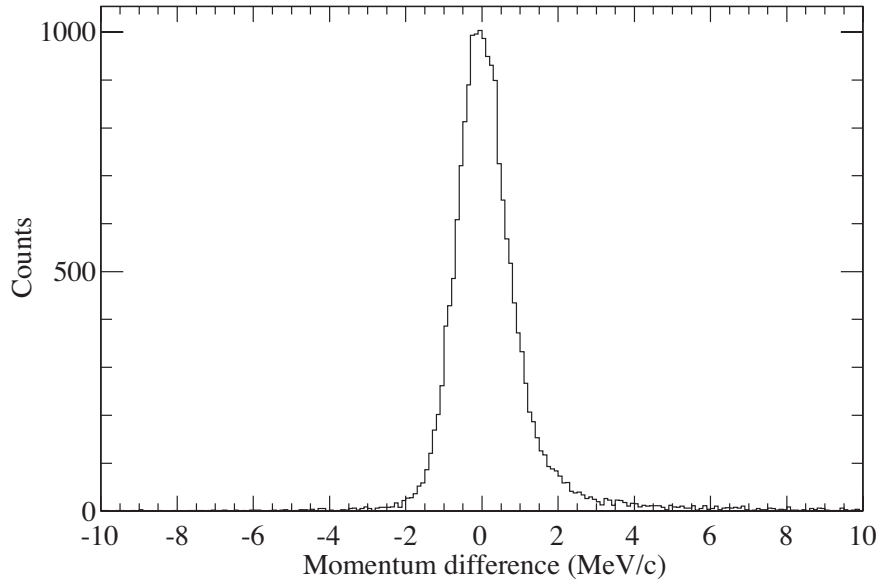

Figure 3.14: A distribution of the momentum difference between the two spectrometers for a 0.72 GeV/c pion beam.

Vertex resolution

Figure 3.15 shows distributions of spatial and angular differences at the target center between incident and outgoing momentum vectors in the 0.72 GeV/c empty-target data. In this data, both spectrometers measured the same momentum vector of beam pions. We corrected SKS geometry so as to adjust the center positions of these distributions at the origin, where these systematic offset came from geometrical inaccuracy between the two spectrometers. The measured vertex resolutions and geometrical corrections are summarized in Table 3.2.

Then, we evaluated the multiple scattering effect in the 19.1 g/cm^2-thick polyethylene target by a simulation, where the intrinsic performance of spectrometers was taken into account. As a result, the effective resolutions of reaction angle and z-vertex were estimated to be 1.5 degree (FWHM) and to be 3.5 cm (FWHM), respectively.

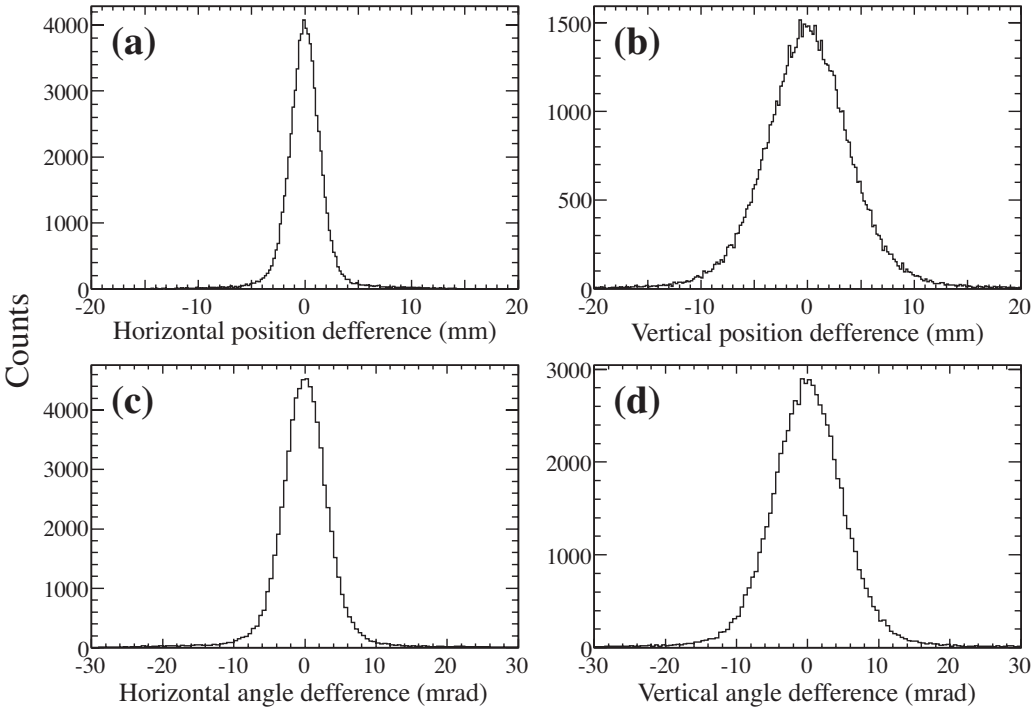

Figure 3.15: Distributions of spatial (a,b) and angular (c,d) differences at the target center between two tracks measured by the beam spectrometer and SKS in the 0.72 GeV/c empty-target data. The centers of distributions were adjusted to be zero by correcting the SKS geometry.

Table 3.2: Vertex resolutions and geometrical offsets between the beam spectrometer and SKS in the 0.72 GeV/c beam-through data.

	Resolution (mm or mrad in rms)	Geometrical offset (mm or mrad)
Horizontal position	1.4	-1.87
Vertical position	4.0	-1.15
Horizontal angle	3.1	4.51
Vertical angle	5.0	2.59

Mass resolution

Expected mass spectra for the ${}^{12}_{\Lambda}\mathrm{C}(\pi^+, K^+)$ reaction were simulated based on the evaluated performance of the two spectrometers. We used a real beam profile obtained with the BEAM trigger for the input of the beam parameters. The detector acceptance for a scattered kaon was also taken into account by reproducing SKS in the simulation. A uniform distribution of event vertex along the beam axis was assumed and the scattered kaons were generated uniformly in the center of mass frame. The momentum of scattered kaons was determined by solving the kinematics of the ${}^{12}_{\Lambda}\mathrm{C}$ ground state production with a given momentum of a pion. In the calculation of a missing mass, we applied the same energy loss correction to the simulated data as the real analysis. The simulated mass spectra are shown in Figure 3.16. By comparing figure (a) with others, one can see asymmetry of the peak shapes caused by the Landau tail of energy loss process. As a result of the simulation, the mass resolution was estimated to be 2.2 MeV for the graphite target and to be 6.0 MeV for the polyethylene target by taking a full width at the half maximum. These resolutions were explained by energy struggling inside the target volume.

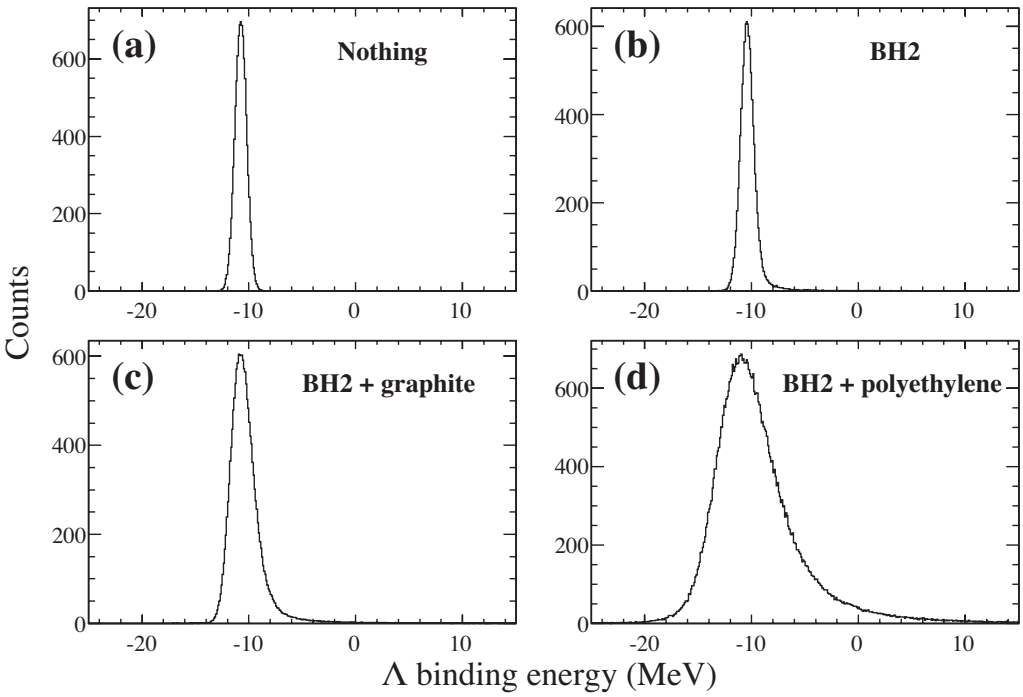

Figure 3.16: Simulated mass spectra for the ${}^{12}_{\Lambda}\mathrm{C}$ ground state production via the ${}^{12}\mathrm{C}(\pi^+, K^+)$ reaction. (a): Intrinsic response function. (b): Response function with BH2. (c): Response function with BH2 and graphite target. (d): Response function with BH2 and polyethylene target.

3.6.2 Recoil velocity of hypernulei

In the missing mass analysis for the (π^+, K^+) reaction, we can also calculated the recoil velocity of produced hypernuclei by

$$\beta = \frac{\sqrt{p_\pi^2 + p_K^2 - 2p_\pi p_K \cos\theta_{\pi K}}}{E_\pi - E_K + M_{HY}} ,$$

where p and E stand for the momentum and the energy of pions or kaons, $\theta_{\pi K}$ is the reaction angle in the laboratory frame, and M_{HY} is the missing mass. Because we know the β for each of all recorded events, it is possible to correct Doppler-shifted energy of each γ ray. The event-by-event correction method is described in the next chapter.

Figure 3.17 shows a distribution of recoil velocity calculated for the polyethylene target data, where events of the bound state production were considered. The resolution of the recoil velocity was estimated to be 0.1 % (FWHM) with a simulation. We compared the velocity of a generated hypernucleus with the reconstructed velocity from the momenta of a pion and a kaon in the simulation.

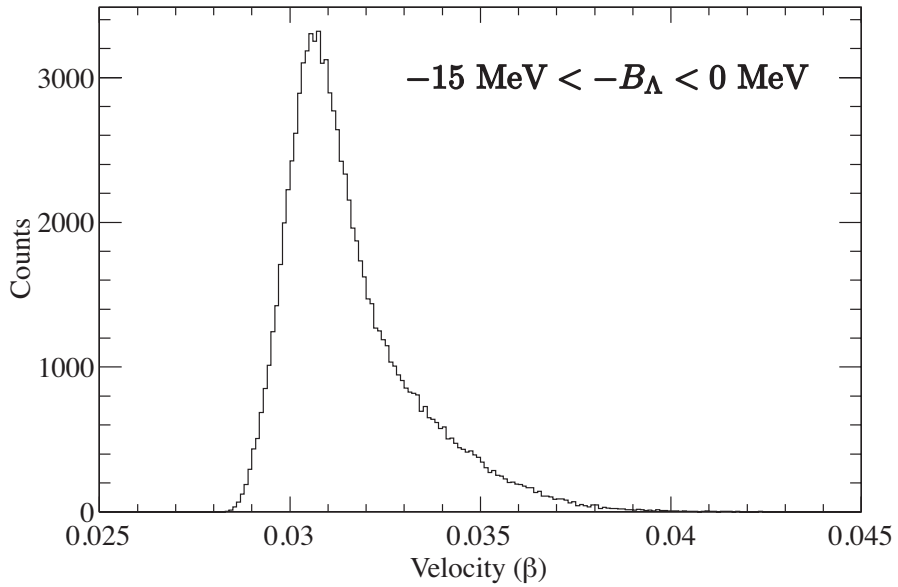

Figure 3.17: Velocity distribution of the recoiling hypernuclei in the (π^+, K^+) reaction. The velocity was calculated only if the missing mass was obtained in the bound state region of ${}^{12}_{\Lambda}\mathrm{C}$.

3.6.3 Acceptance of SKS

Angular dependence of the acceptance for scattered kaons was studied from the two aspects, namely coverage of the detectors and efficiency of the analysis. The polyethylene target was considered in this study.

Geometrical acceptance

The effective solid angle of SKS in the E566 experiment was calculated with a simulation. The simulation conditions were the same as the previous section, where the measured beam profile and the kinematics of the ${}^{12}_{\Lambda}$C ground state production were used for generating scattered kaons. The effects of energy loss and multiple scattering were also considered. The effective solid angle $\Delta\Omega(\theta)$ was calculated as a function of the reaction angle θ by

$$\Delta\Omega(\theta) = 2\pi \int_{\theta-\frac{1}{2}\Delta\theta}^{\theta+\frac{1}{2}\Delta\theta} d\cos\theta' \times \frac{\text{number of events accepted}}{\text{number of events generated}} .$$

The results is shown in Figure 3.18. In the present calculation, the $\Delta\Omega(\theta)$ was averaged on the distribution of the beam profile and scattered kaon momentum.

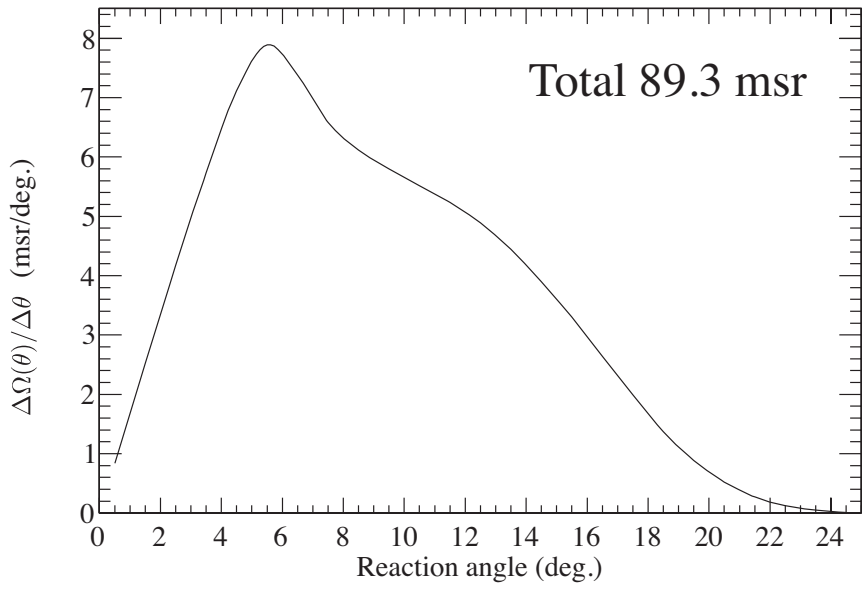

Figure 3.18: Effective solid angle of SKS in the E566 experiment.

Efficiency of tracking analysis

The analysis efficiency for the SKS tracking was estimated by using the (π, p)X events recorded in the PIK trigger, in which the particle decay in flight was negligible. The SKS tracking efficiency was evaluated as

$$\varepsilon = \frac{N(\text{ SksTrack=1 })}{N(\text{ SdcInTrack=1 } \times \text{ SdcOutTrack=1 })} .$$

The number of SKS track candidates is denoted as N(SdcInTrack=1 $\times$ SdcOut-Track=1), where we require a single local track with $\chi^2 < 100$ in both local track search at SDC1,2 and SDC3,4. N(SksTrack=1) denotes the number of events for which we succeeded in reconstructing a SKS trajectory with $\chi^2 < 30$. Figure 3.19 shows the efficiency of SKS tracking as a function of the reaction angle. The efficiency was kept about 94 % in the reaction angle region from 2 to 15 degree, but it became worse toward lager reaction angle. This dependence could result from uncertainty of the magnetic field in the fringing region of the SKS magnet calculated by ANSYS code. For forward angles less than 2 degree, the efficiency was not evaluated because of unremovable contamination of beam events.

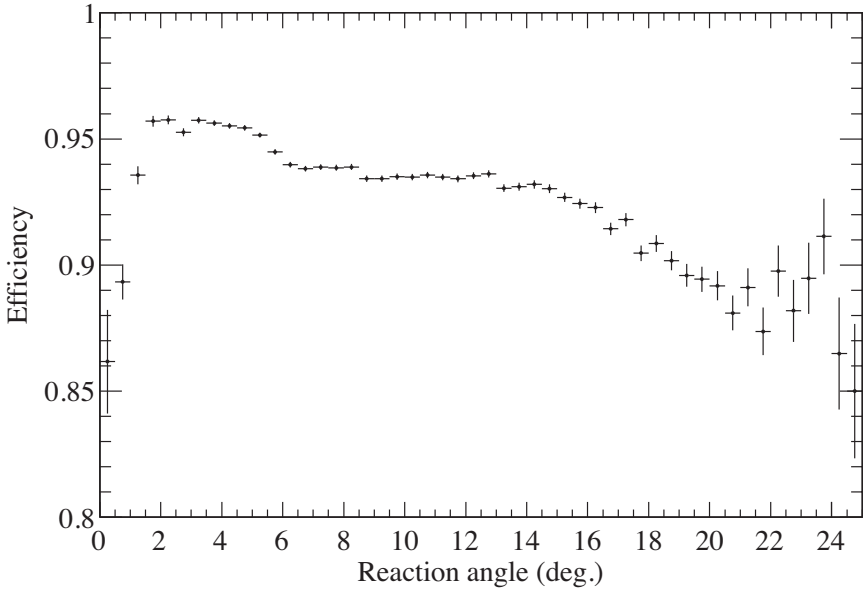

Figure 3.19: The SKS tracking efficiency as a function of the reaction angle. Efficiencies at forward angles less than 2 degree are not correct due to the contamination of beam events.

Chapter 4

Analysis II — γ rays

The analysis for Hyperball2 is described in this chapter. The goal of this part is to obtain a γ-ray spectrum in coincidence with the (π^+, K^+) reaction.

4.1 Outline

The analysis procedure of Hyperball2 consists of four steps as listed below.

1. Selection of events

In the experiment, we took a coincidence time window to be 3.6 μs between the (π^+, K^+) reaction and the hits of the Ge detectors in the trigger level. This time window was longer than a typical timing of hypernuclear γ-ray emission but was necessary for the pulse shaping of high-resolution amplifiers for the Ge detectors. Thus, a tight timing cut in the off-line analysis is important to reject accidental background in the γ-ray spectra.

Background events from Compton scattering and incomplete pulse shaping were also removed in this stage.

2. Energy calibration of γ rays

Recorded energy deposits of the Ge detectors were converted into the energy of γ rays. γ rays from standard sources and from normal nuclei excited by the beam were used for the calibration.

3. Add-back analysis of clover-type detectors

If more than one hit exist in a clover-type Ge detector equipped with four germanium crystals, we take the sum of calibrated energies for the four crystals.

4. Doppler shift correction

Some of the measured γ-ray energies could have been changed by the Doppler effect, if they were emitted in flight from recoiling hypernuclei. This effect was corrected event by event in the analysis.

4.2 Event selection

4.2.1 Coincidence events with the (π^+, K^+) reaction

Figure 4.1 shows timing distributions of a typical Ge detector for various ADC ranges, where the timing of the Ge detectors was defined as the time difference from the beam timing. Since the time resolution of a Ge detector strongly depended on the amplitude of the signal, we used constant-fraction discriminators to extract the timing of γ-ray hits. However, the recorded timing distribution of the Ge detector still had a correlation with the ADC as shown in Figure 4.2. In order to suppress accidental backgrounds which were not associated with the (π^+, K^+) reaction, we applied a timing cut for the Ge detectors as shown in the same figure. The gate width for the timing cut was a function of ADC and it was optimized for each of the Ge detectors.

4.2.2 Background events

Preamplifier reset and pulse pileup

In the pulse shaping process of the main amplifiers, some of pulses are distorted by two factors. Firstly, the preamplifier rest causes a γ-ray peak broadened by base-line shift and also makes a fake peak at a particular energy in the γ-ray spectrum by a ripple noise. Thus, events occurred within 35 μs after a preamplifier reset were removed by using the recorded timing of the reset.

Secondly, if a second signal comes before the pulse shaping of the first signal is finished, the energy information of both signals is not converted correctly by the peak-sensitive ADC. We recorded time difference of subsequent γ-ray events by using multi-hit TDC modules in order to reject such pileup events in the off-line analysis. However, in the multi-hit TDC's, satellite signals associated with true events due to the ringing noise from the fast shaping amplifier were also recorded. In this analysis, pileup rejection was not done for saving true events as much as possible.

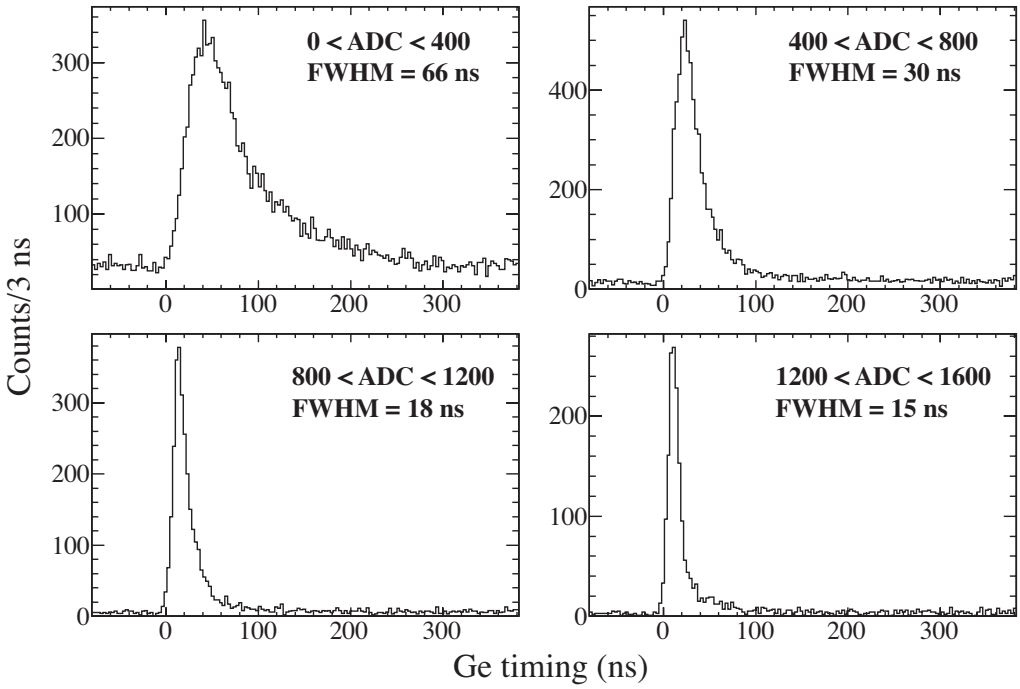

Figure 4.1: Timing distributions of a typical Ge detector for various ADC ranges. The time origin was adjusted to the timing of the beam. ADC ranges and time resolutions are shown in the each figure. The ADC denotes raw values read out from a Analog-to-Digital Converter and they can be converted into the energy by roughly 1.1 keV/ch in this experiment.

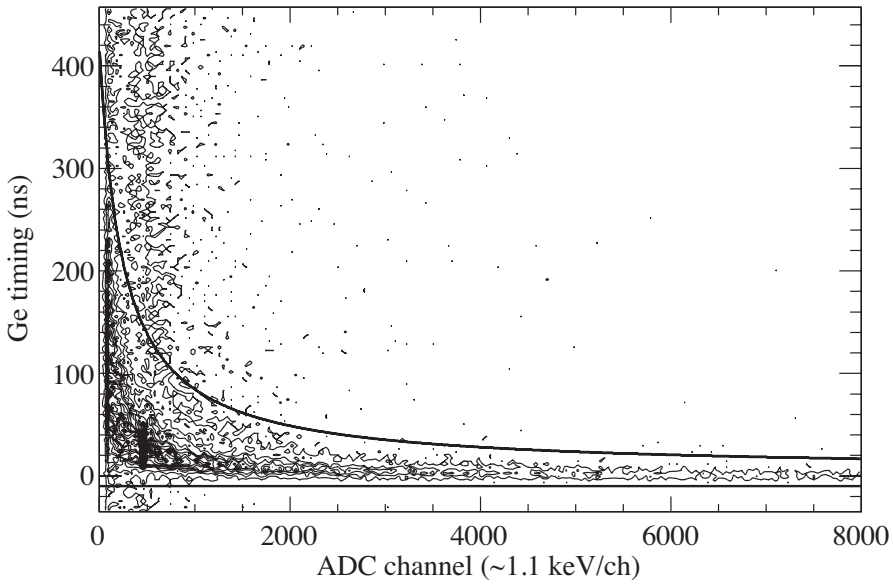

Figure 4.2: Relation between ADC and timing of a typical Ge detector. We selected the region enclosed in the solid lines for γ-ray events associated with the (π^+, K^+) reaction. The ADC scale is $\sim$ 1.1 keV/ch.

Background suppression with BGO counters

If a γ ray escapes from a germanium crystal by Compton scattering, the recorded energy deposit of the Ge detector makes a background in the γ-ray spectrum. By taking anti-coincidence between the Ge detector and the surrounding BGO counters, we can reduce such a background effectively. In this analysis, a coincidence gate was set to be -5 ns $< T <$ 60 ns commonly to all the BGO counters, where T denotes the time difference between the hits of the BGO counters and the beam timing. The coincidence gate is illustrated in Figure 4.3 with a timing distribution of a typical BGO counter. The optimization of the gate width was done so as to achieve a good suppression efficiency with a moderate accidental killing rate. We optimized the signal-to-noise ratio of a known 1483-keV γ ray emitted from $^{11}_{\Lambda}$B, which was observed in the previous Hyperball experiment [22]. The accidental killing rate was measured by comparing the 1483-keV peak counts before and after the suppression and it was found to be 3 % in this analysis.

Figure 4.4 shows γ-ray spectra in coincidence with the (π^+, K^+) reaction, where the timing cut of the Ge detectors and the rejection of reset events were done. As demonstrated in the figure, it is clear that γ-ray peaks with low intensity are revealed effectively by the BGO suppression. The BGO suppression can also reduce background efficiently in the energy region of more than 3 MeV as shown in Figure 4.5. Typically, background events were suppressed by a factor of four in this analysis.

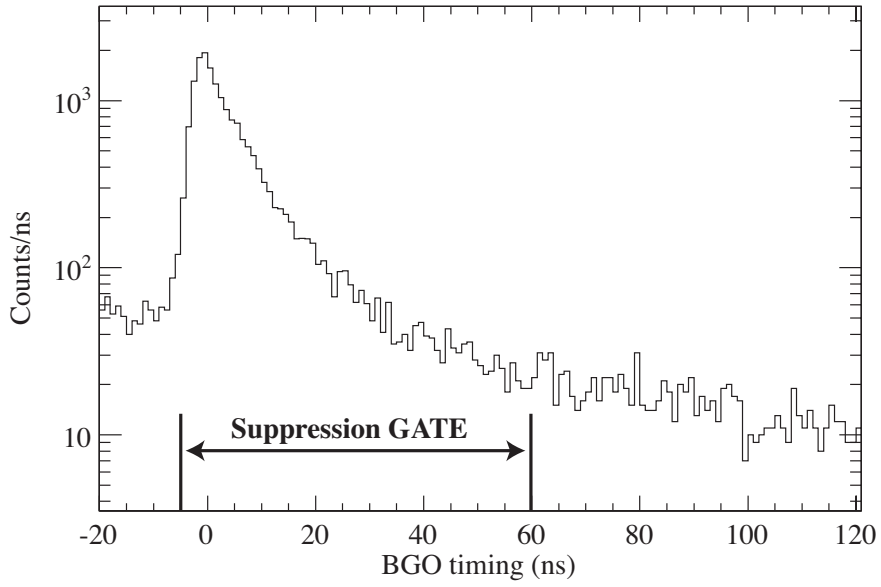

Figure 4.3: Timing distribution of a typical BGO counter.

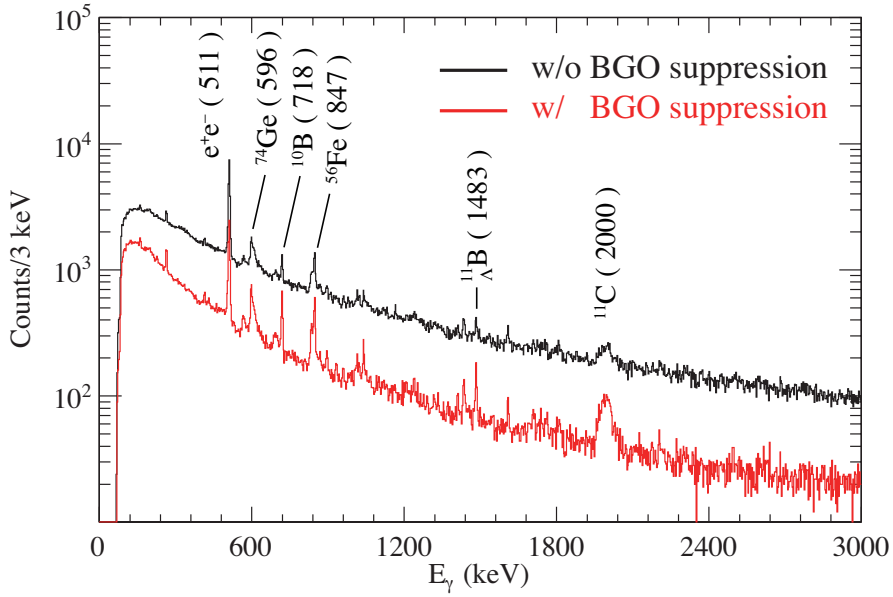

Figure 4.4: γ-ray spectra in coincidence with the (π^+, K^+) reaction. The energy region of less than 3 MeV is shown with and without the BGO suppression. Prominent γ-ray peaks are indicated in the figure.

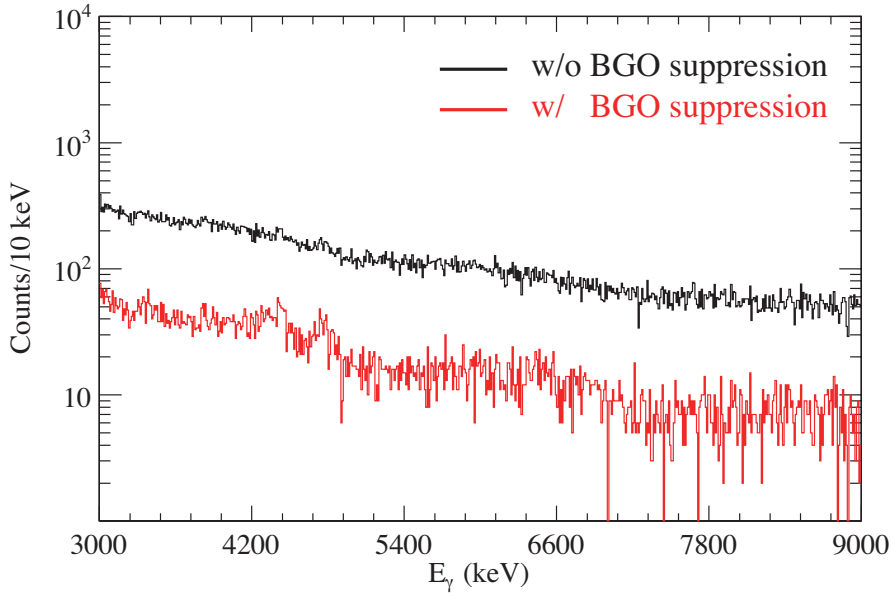

Figure 4.5: γ-ray spectra in coincidence with the (π^+, K^+) reaction. The energy region of larger than 3 MeV is shown with and without the BGO suppression. No prominent γ-ray peak is observed in this region.

4.3 Energy calibration of Ge detectors

4.3.1 Calibration curve

The energy range of Hyperball2 was set to be from 0.1 to 9 MeV because the highest energy of γ rays from ${}^{12}_{\Lambda}$C is expected to be 8 MeV according to the experimental data of KEK-E369. We used two types of γ rays for the energy calibration of the Ge detectors in the wide range. One is γ rays from a ^{152}Eu standard source and the other is delayed γ rays originated from the beam. The γ rays in use for the calibration are summarized in Table 4.1. The ^{16}N was produced via the ^{16}O(n, p) reaction, where the oxygen in the BGO crystals was the most possible target. Similarly, the ^{24}Na was produced by the ^{27}Al(n, α) reaction in the Hyperball2 frame. In the experiment, we measured γ rays from both unstable nuclei in the off-beam period, because their β-decay half lives were longer than a spill of the beam extraction.

We prepared two calibration curves with different energy ranges for each of the Ge crystals. They corresponded to the ranges between 0.1 and 2.8 MeV and between 2.6 MeV and 9 MeV. A quadratic function was used to fit the calibration curve in both ranges. The fitting results are shown in Figure 4.6. It is obvious that the number of calibration points for the higher energy side was not enough to fully cover the required energy range. Accuracy of the calibrated energy about the whole data set is discussed in the last part of this chapter.

4.3.2 Peak shift

The in-beam performance of the Ge detectors was monitored by using the ^{60}Co pulser trigger. The gains of the Ge detectors were verified to be stable during the experiment by checking the energy difference between the annihilation peak and the ^{60}Co peaks. On the other hand, it was found that the γ-ray energy was systematically shifted by $\sim$ 1 keV to the lower side when the beam was on. This phenomenon is explained by the continuous base-line shift at the main preamplifier due to the high counting rate. For the correction, we adjusted the energy of the annihilation peak at 511 keV. The run-by-run peak shift correction was adopted to each of the Ge detectors, where typical length of a run is 2 hours.

Table 4.1: The γ rays in use for the energy calibration.

Parent	Half life	Energy (keV)		Origin
e^+e^-		511.0		
^{152}Eu		121.8		γ-ray source
		244.7		
		344.3		
		778.9		
		964.1		
		1112.1		
		1408.0		
^{24}Na	15.0 h	2754.0		delayed γ
^{16}N	7.13 s	6128.6		delayed γ
		5617.6	SE6129*	
		5106.6	DE6129*	

* SE and DE stand for Single-Escape peak and Double-Escape peak, respectively.

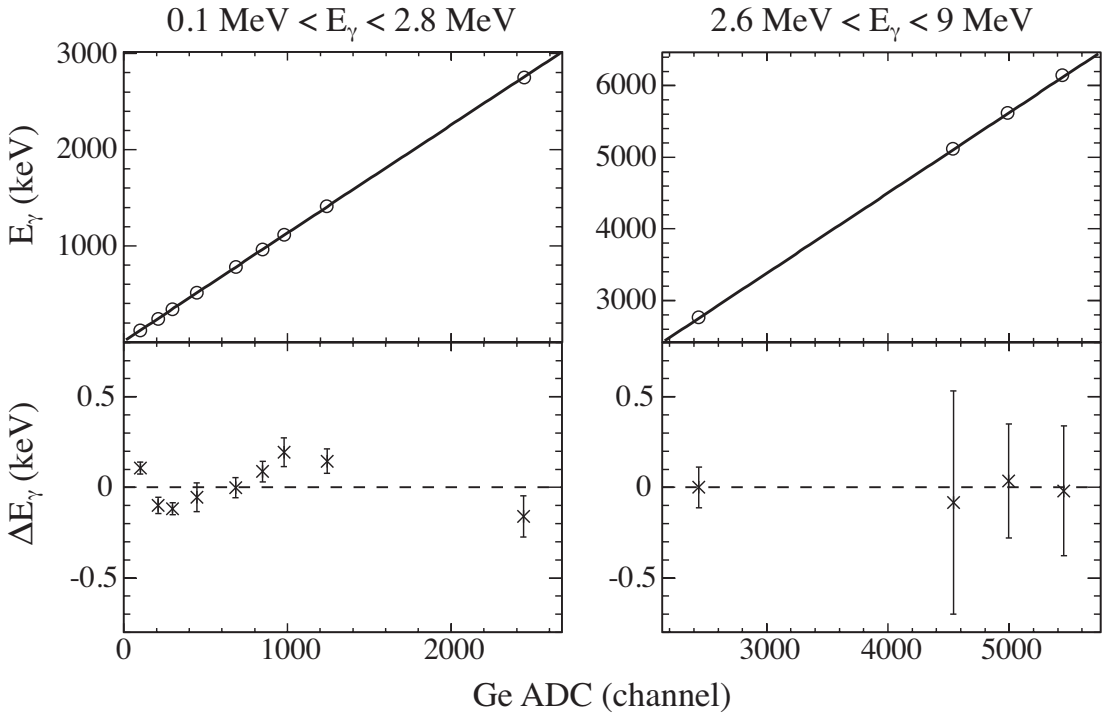

Figure 4.6: Calibration curves for a typical Ge detector in the two different energy range. Residuals of quadratic curve fitting are also shown.

4.4 Add-back analysis of clover-type detectors

Each of four crystals settled in the clover-type Ge detector was treated as an independent single-type detector in the process of event selection and energy calibration. In order to increase the photo-peak efficiency, we took a sum of energies for the four crystals when they have multiple hits. This add-back effect was studied by using the data taken with a ^{60}Co source. The multi-coincidence events in the same clover detector were classified into three condition as listed below.

- double coincidence (off-diagonal crystal combination)
- double coincidence (diagonal crystal combination)
- triple or quadruple coincidence

Figure 4.7 shows the γ-ray spectra for the above conditions with and without the add-back analysis, where each condition is illustrated in the right side of the figures. In the condition of double coincidence, it was clear that Compton events were suppressed and photo-peak events were increased with the add-back analysis. On the contrary, the add-back effect was not evident in the condition of triple or quadruple coincidence, in which independent two γ rays were mainly involved. As a result of this study, we applied the add-back analysis to the clover detectors only in the condition of double coincidence. Events with triple or quadruple coincidence were removed as an accidental background. The add-back factor of about 1.4 was obtained by comparing the photo-peak counts at 1.33 MeV with and without the add-back analysis.

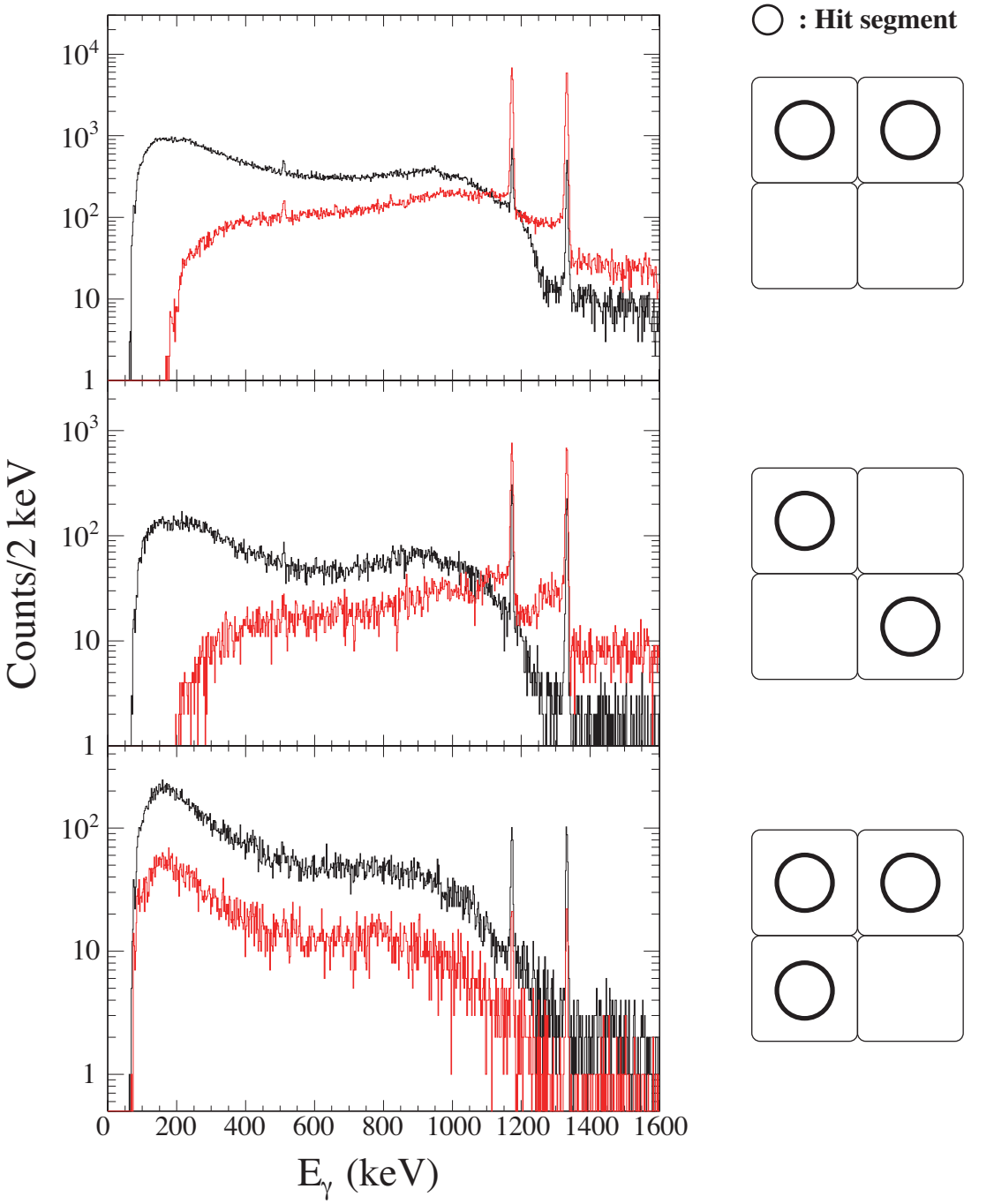

Figure 4.7: Add-back effect of clover-type detector in the three multi-hit condition. A ^{60}Co source was used. The black curves were obtained without add-back analysis and the red curves were obtained with the add-back analysis. Typical hit combinations are illustrated in right side of each figure. Top: spectra for off-diagonal double coincidence. Middle: spectra for diagonal double coincidence. Bottom: spectra for triple or quadruple coincidence.

4.5 Doppler-shift correction

When a γ-ray energy is larger than a few hundred keV, a typical life time of the M1 transition is expected to be much shorter than the stopping time of recoiling hypernucleus in the target medium. For example, a 1-MeV $M1$ transition γ ray is emitted within a few femtosecond while the stopping time of the parent hypernucleus is of the order of a picosecond. The measured energy of the γ ray should be broadened due to the Doppler effect.

By using the obtained recoil velocity (β) in the missing mass analysis, the measured energy of a γ ray can be corrected event by event as

$$E_\gamma^{corrected} = \frac{1}{\sqrt{1-\beta^2}} \cdot (1 - \beta \cos\phi) \cdot E_\gamma^{measured} \quad ,$$

where $E_\gamma^{measured}$ is the measured energy of a γ-ray and $E_\gamma^{corrected}$ is the Doppler-shift corrected energy, and ϕ is the angle between the direction of the recoil velocity and the γ ray in the laboratory frame. The direction of the emitted γ ray is defined from the reaction vertex and the position of the Ge detector which detected the γ ray. In this analysis, the center position on the surface of a germanium crystal was used for the detector position. We took the center position of both crystals in the case of a double coincidence event for the clover-type detectors. The effectivity of the Doppler-shift correction is shown in the next section together with the other performance of Hyperball2.

4.6 Performance of Hyperball2

The performance of Hyperball2 is discussed in this section. We used a Monte-Carlo simulation with the GEANT4 code to evaluate the performance. The data taken in several conditions were also used.

4.6.1 Precision of the energy calibration

The long-term stability of the energy calibration was evaluated by using the data accumulated during the off-beam period continuously in the whole beam time. More than thirty γ-ray peaks were identified in the off-beam spectrum. After summing up all the off-beam data, we observed another γ ray peak from ^{16}N as well as its escape peaks in the energy region around 7 MeV. In fact, these peaks were observed in the calibration data but was not used for calibration points due to insufficient peak counts. We chose prominent peaks and compared their measured energy with

the known energy including the 7-MeV peaks. Figure 4.8 shows residuals between the calibrated energy and the real energy, where γ-ray peaks in use for the calibration points are indicated in red. The residuals were obtained in the two ranges of the corresponding calibration curves. Because whole sets of off-beam data are used in this analysis, the residuals represent the total precision of the energy calibration.

From these result, the calibration error was estimated to be ± 1 keV for the energy range of less than 3 MeV. We took ± 2 keV for the error in the energy range from 3 MeV to 7 MeV. Because no data was available for the evaluation, the calibration error was extrapolated to be ± 3 keV for the range from 7 MeV to 9 MeV.

The off-beam spectra are shown from Figure 4.9 to Figure 4.12, where the γ-ray peaks used in this study are indicated in red as well as the other identified peaks. The BGO suppression was not done in these spectra to save the escape peaks indicated as SE and DE.

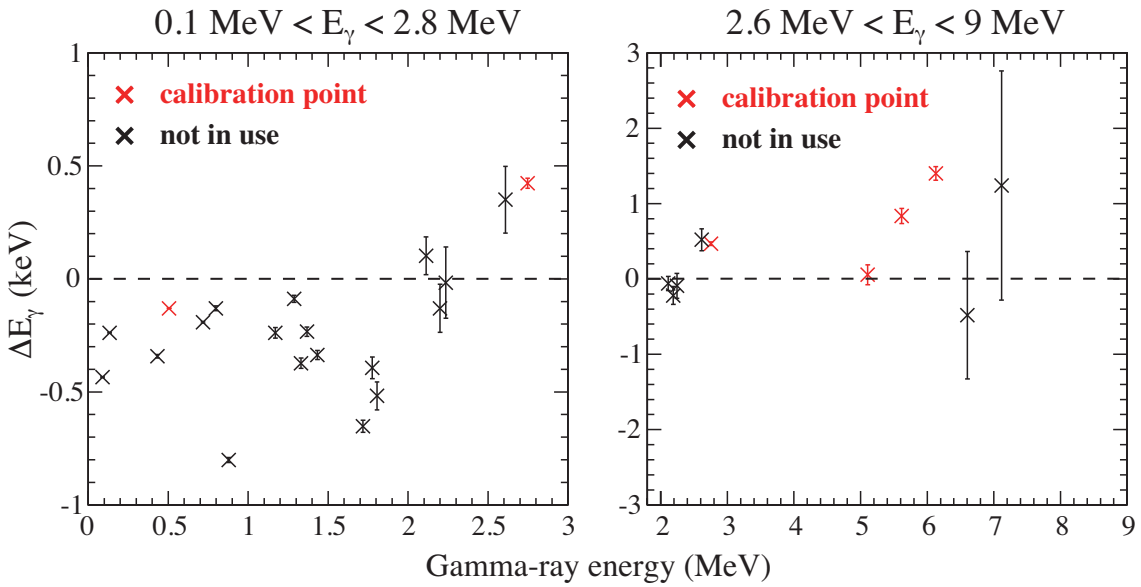

Figure 4.8: Long-term stability of the energy calibration. Residuals are evaluated in the two ranges of calibration curves.

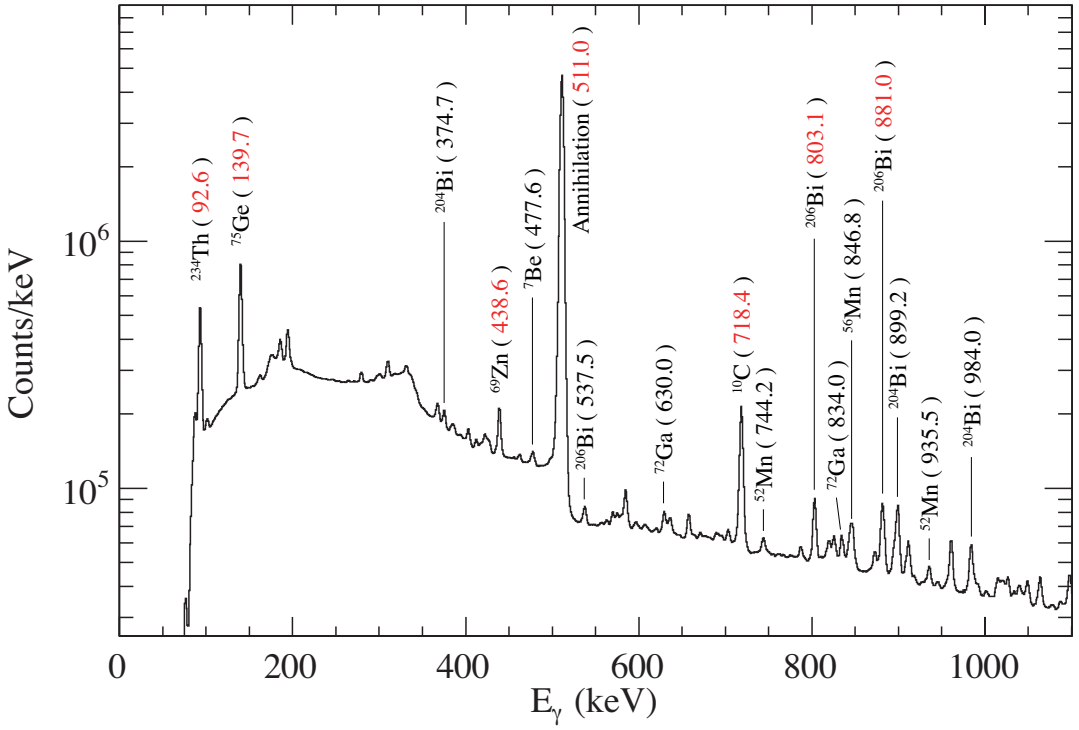

Figure 4.9: Off-beam γ-ray spectrum from 0 to 1.1 MeV.

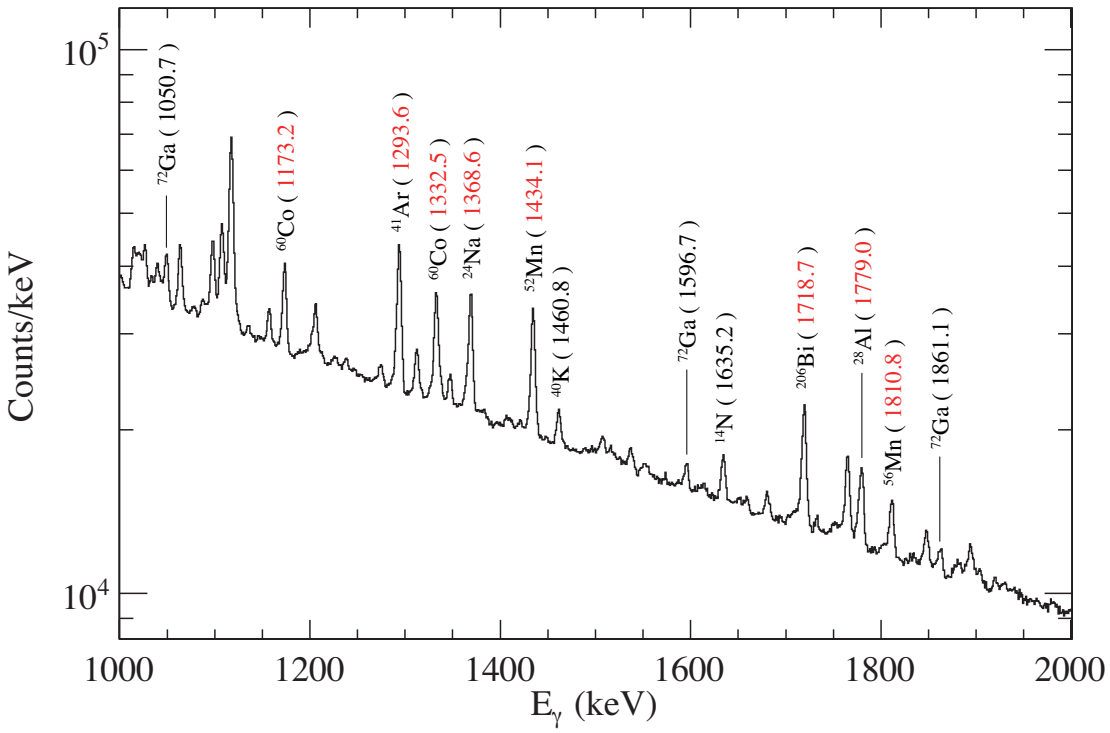

Figure 4.10: Off-beam γ-ray spectrum from 1 to 2 MeV.

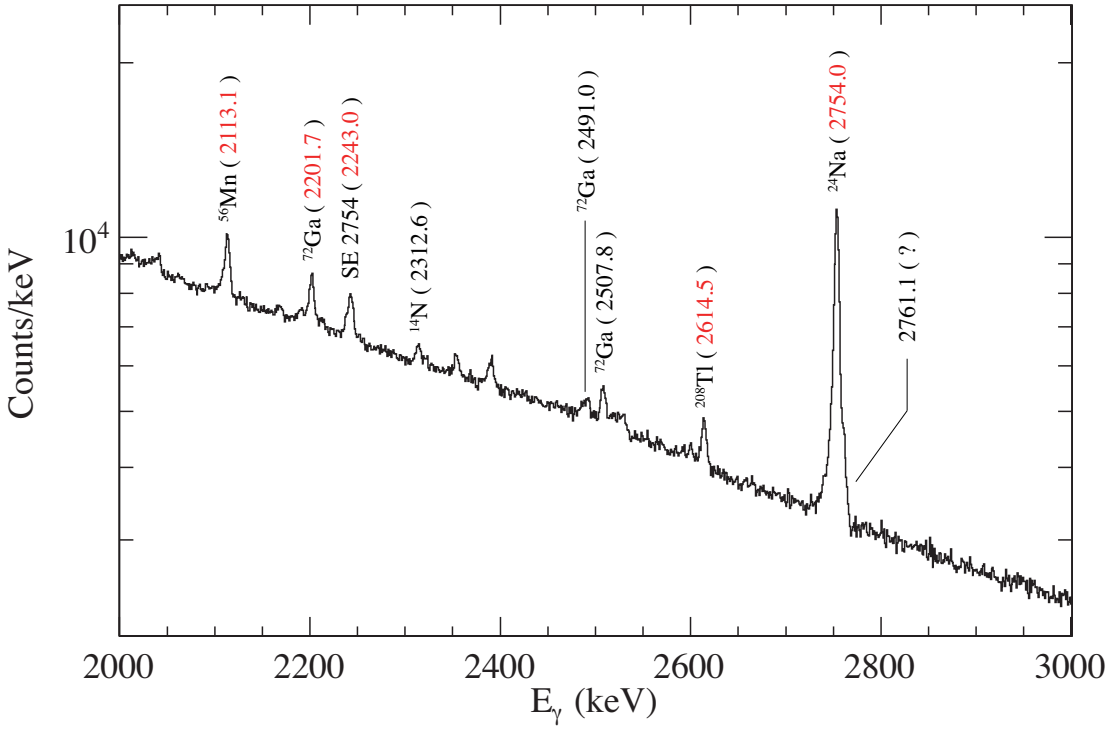

Figure 4.11: Off-beam γ-ray spectrum from 2 to 3 MeV.

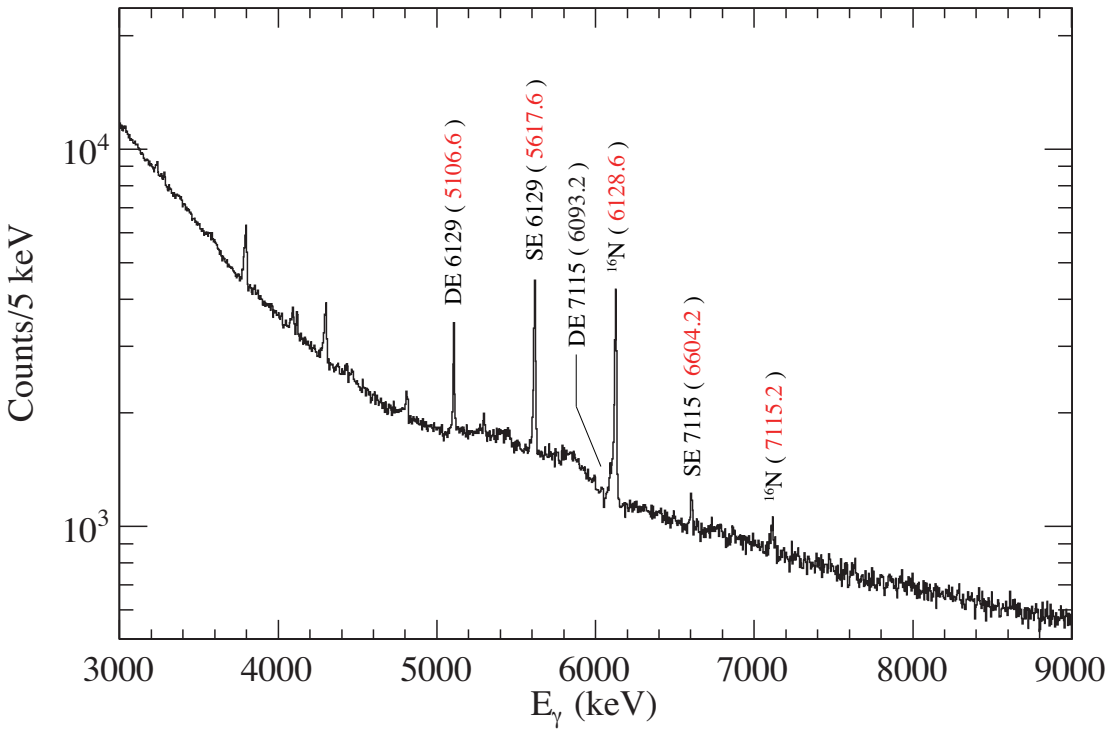

Figure 4.12: Off-beam γ-ray spectrum from 3 to 9 MeV.

4.6.2 Energy resolution

We studied the total energy resolution of Hyperball2 after summing up all the data of the Ge detectors. Figure 4.13 shows the obtained energy resolution in FWHM from the off-beam data. The plotted points are the same γ rays as used in the study of calibration precision except for the 511-keV peak, which was slightly broadened due to in flight annihilation. We assumed the squared energy resolution to be a linear function of energy as

$$\delta E_{total} = \sqrt{A \cdot E_\gamma + \delta E_{etc}^2} \ ,$$

where A and δE_{etc}^2 are parameters and obtained by fitting the measured energy resolution. The fitting result is expressed by solid line in the figure and we obtained $A = 1.25 \times 10^{-2}$ keV and $\delta E_{etc}^2 = 9.38$ keV^2. On the other hand, the resolution of the 511-keV peak was measured to be 4.8 keV (FWHM). Because these results are obtained from the off-beam data, we must consider effects of the high counting rate due to the beam. According to the ^{60}Co pulser data, it was found that the energy resolution was degraded by 6 % in the on-beam period. Thus, on-beam resolution was estimated by multiplying a factor of 1.06.

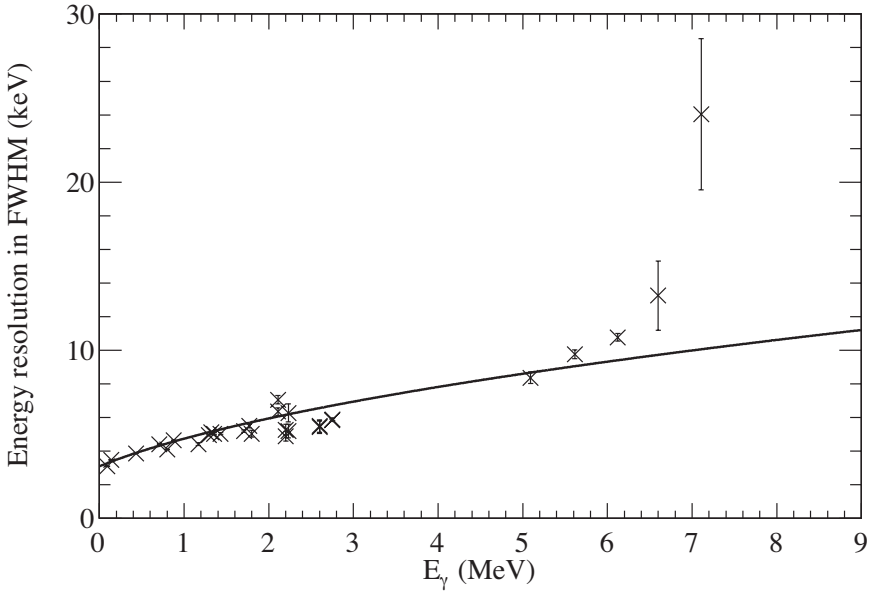

Figure 4.13: Off-beam energy resolution of the γ-ray spectrum summed up for all of the Ge detectors. The data was fitted as shown by the solid line (see text).

4.6.3 Photo-peak efficiency

The total photo-peak efficiency of Hyperball2 was studied up to the 9-MeV γ ray by using a simulation. In the simulation, we considered measured detector positions, all materials surrounding a germanium crystal, γ-ray absorption by target material, and add-back effect of the clover-type detectors. The DAQ dead time and the analysis efficiency were not taken into account.

Figure 4.14 shows the results of the simulation, where the photo-peak efficiency is drawn as a function of γ-ray energy. In the black solid line, γ rays were isotropically generated from the center of Hyperball2. The red line represents the simulated photo-peak efficiency when the polyethylene target is included and the source of the γ rays are randomly distributed within the target. The difference between the black and the rad lines shows the effect of absorption and scattering in the target.

We also recorded data with a ^{152}Eu source for evaluating the absolute efficiency of Hyperball2. However, the absolute efficiency was not obtained due to a problem in the recorded live time. Thus, the result from the ^{152}Eu data, which was plotted in the figure, was scaled to the simulated efficiency curve in order to confirm the curve shape.

The in-beam live time of Hyperball2 averaged over the beam time was measured to be 59.3 ± 0.3 % from the ^{60}Co pulser data as described in Section 2.5.3. By adding the BGO accidental killing rate (3 %), the in-beam photo-peak efficiency was estimated to decrease by 58 % than this simulation results.

4.6.4 Expected peak shape

We simulated the peak shape broadened by Doppler effect and the peak shape after the Doppler-shift correction. The following points were the essence of the simulation.

- Intrinsic response function of a Ge detector was assumed to be a Gaussian function with the width expected from Figure 4.13.

- The identical geometry configuration of Ge detectors as the experimental setup was used.

- Random distribution of the reaction point inside the polyethylene target and isotropic γ emission in the center of mass frame were assumed.

- Velocity of a recoiling hypernucleus was calculated from the kinematics of the $^{12}_{\Lambda}$C ground state production, where the measured beam profile was used.

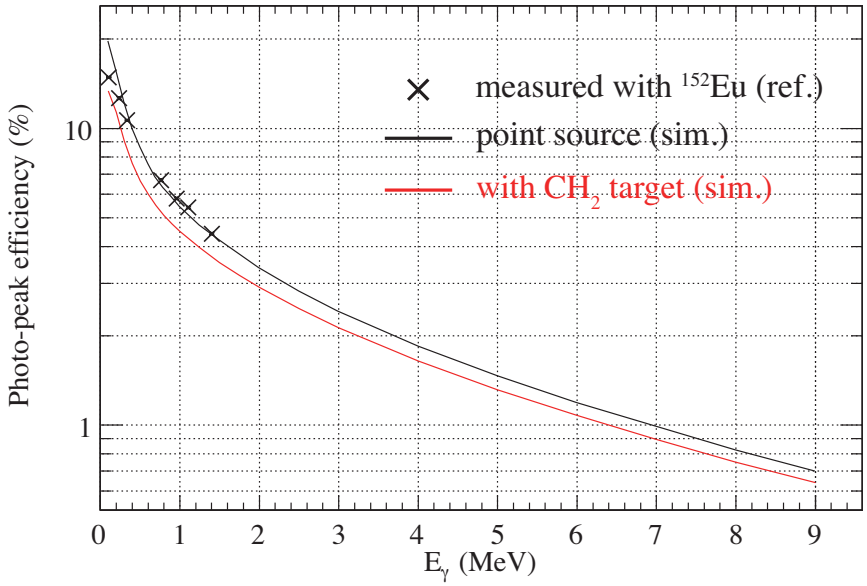

Figure 4.14: Photo-peak efficiency of Hyperball2 as a function of γ ray energy. Total twelve single-type Ge detectors and six clover-type Ge detectors are considered. The solid curves are results of the simulation. The ^{152}Eu data are plotted for just reference.

- Measured performances of the spectrometers, such as the vertex resolution and the velocity resolution, were taken into consideration.

Figure 4.15 shows a result of the simulation, in which 3-MeV γ ray is considered. In this case, we obtained a peak width of 26 keV (FWHM). As a result of this study, the peak width after the Doppler-shift correction can be explained by ambiguity of the γ-ray direction resulted from the germanium crystal size and the vertex resolution. On the other hand, a slightly asymmetric peak shape before the Doppler-shift correction was obtained because two of the six Ge detectors in the downstream ring were not working in the experiment.

4.6.5 Systematic errors of γ-ray energy

Systematic errors of the measured γ-ray energy were evaluated for the following points.

Calibration error

From the residuals of the calibrated energy in Figure 4.8, we took a systematic error of 1.0 keV below 3-MeV range and 2.0 keV in the range from 3 MeV to 7 MeV. The error of 3.0 keV is extrapolated for the energy range over 7 MeV.

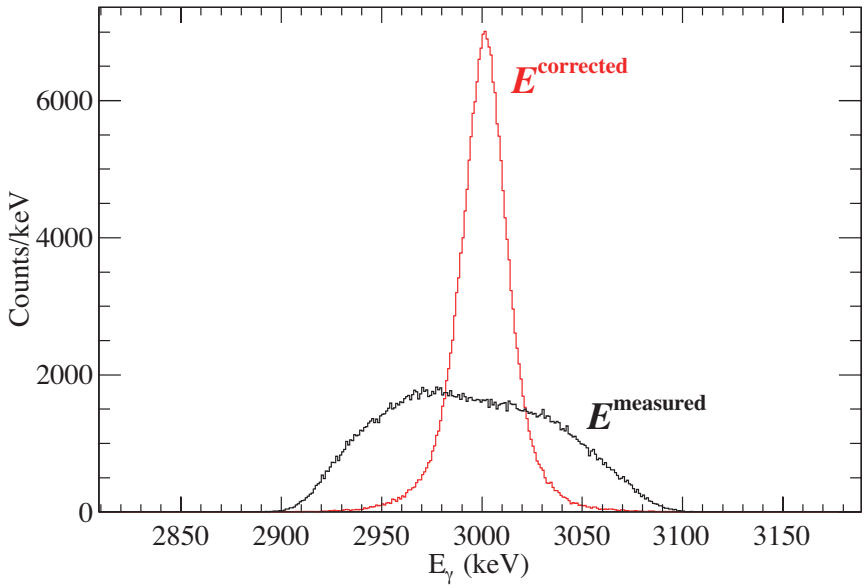

Figure 4.15: Simulated peak shape of 3-MeV γ ray. The black line shows the Doppler-broadened peak shape and the red line shows the Doppler-shift corrected peak shape. The lopsided peak shape before the correction results from the asymmetrical configuration of the Ge detectors.

Uncertainty of Doppler-shift correction

The geometrical ambiguity between the center of Hyperball2 and the center of the two spectrometers was expected to be less than 5 mm. We simulated the energy shift in the case that the vertex was shifted by ± 5 mm and it was found that the energy shift depends on the γ-ray energy. The value was 3.0 keV for the 3-MeV γ ray and 6.0 keV for the 6-MeV γ ray.

As mentioned in the missing mass analysis, we applied an arbitrary correction to the measured kaon momentum in order to adjust the binding energy of the ${}^{12}_{\Lambda}$C ground state at 10.76 MeV. The calculated velocity of the recoiling hypernucleus was modified by 1 % by this correction, but its effect on the Doppler corrected γ-ray energy was estimated to be negligible from the simulation.

Chapter 5

Results

For the final step of the data analysis, hypernuclear γ-ray spectra were obtained by gating the corresponding energy region in the missing mass spectrum. As a result, we succeeded in observing three γ-ray transitions from ${}^{11}_{\Lambda}$B and four transitions from ${}^{12}_{\Lambda}$C. In this chapter, hypernuclear γ-ray spectra are presented and we discuss their level assignments.

5.1 γ-ray spectroscopy of ${}^{11}_{\Lambda}$B

5.1.1 Mass selection

In the ^{12}C(π^+, K^+) reaction, the ${}^{11}_{\Lambda}$B hypernucleus was populated via one proton emission from p_Λ states of ${}^{12}_{\Lambda}$C. In order to identify γ rays from ${}^{11}_{\Lambda}$B, we selected the p_Λ region in the missing mass spectrum as shown in Figure 5.1. In the figure, "A" indicates the p_Λ states region (-2 MeV $< -B_\Lambda <$ 10 MeV) and "B" indicates the highly unbound region ($-B_\Lambda >$ 25 MeV). The mass gate width was determined from the simulated p_Λ peak drawn by red line, where we selected a slightly higher region in order to suppress the contaminating events from the s_Λ states.

5.1.2 γ-ray spectra

Figure 5.2 shows γ-ray spectra plotted in the range below 1.8 MeV with the mass selection of "A" and "B" without Doppler-shift correction. Right figures are the enlarged views of the left figures around 511-keV peak. Several peaks which are common to both spectra do not come from ${}^{11}_{\Lambda}$B, but from other sources such as e^+e^- annihilation (511 keV), ^{74}Ge (596 keV) and ^{56}Fe (847 keV). The 718-keV peak observed in the "B" region comes from ^{10}B produced by the quasi-free Λ production and one proton emission (^{10}B$^*+\Lambda+p$), energy threshold of which is $B_\Lambda = -8$ MeV.

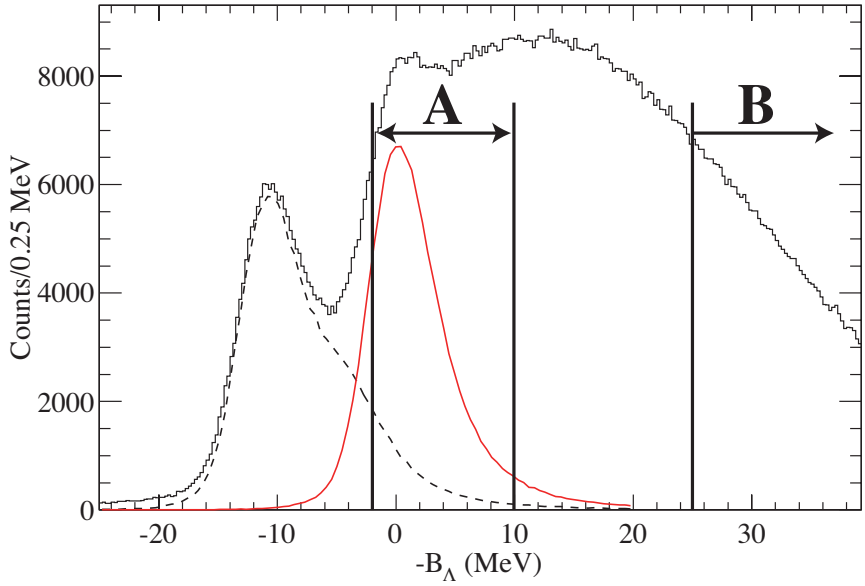

Figure 5.1: Missing mass spectrum of ${}^{12}_{\Lambda}$C. We selected the region "A" as events of ${}^{11}_{\Lambda}$B production. Events of the region "B" was not associated with the hypernucleus production.

Only in the region "A" spectra, we observed three γ-ray peaks at 264 keV, 503 keV and 1483 keV. This fact indicates that those peaks come from ${}^{11}_{\Lambda}$B. The energies of these γ rays are consistent with the KEK-E518 results, where the ^{11}B(π^+, K^+) reaction was used for a dedicated γ-ray spectroscopy on ${}^{11}_{\Lambda}$B hypernucleus and they observed six γ-ray transitions from ${}^{11}_{\Lambda}$B including these three peaks. In the KEK-518 experiment, the 1483 keV peak was assigned to the $E2(1/2^+ \rightarrow 5/2^+)$ transition but assignments of the 264-keV and the 503-keV peaks were not done.

In this study, we succeeded in assigning the 264-keV and the 503-keV peaks as well as reconfirming the 1483-keV peak. Table 5.1 shows the observed peak properties obtained by fitting. Detailed descriptions about their assignments and fitting functions are given in the following subsections.

Table 5.1: Peak properties of the ${}^{11}_{\Lambda}$B γ rays observed in the mass region "A". The quoted error is only statistical. The entry of Est. FWHM stands for the expected detector resolution (see Section 4.6.2).

Peak Energy (keV)	FWHM (keV)	Est. FWHM (keV)	Yield
263.7 ± 0.1	4.4 ± 0.3	3.8	696 ± 40
503.0 ± 0.4	4.4 ± 1.0	4.2	139 ± 28
1483.3 ± 0.3	6.0 ± 0.7	5.6	154 ± 16

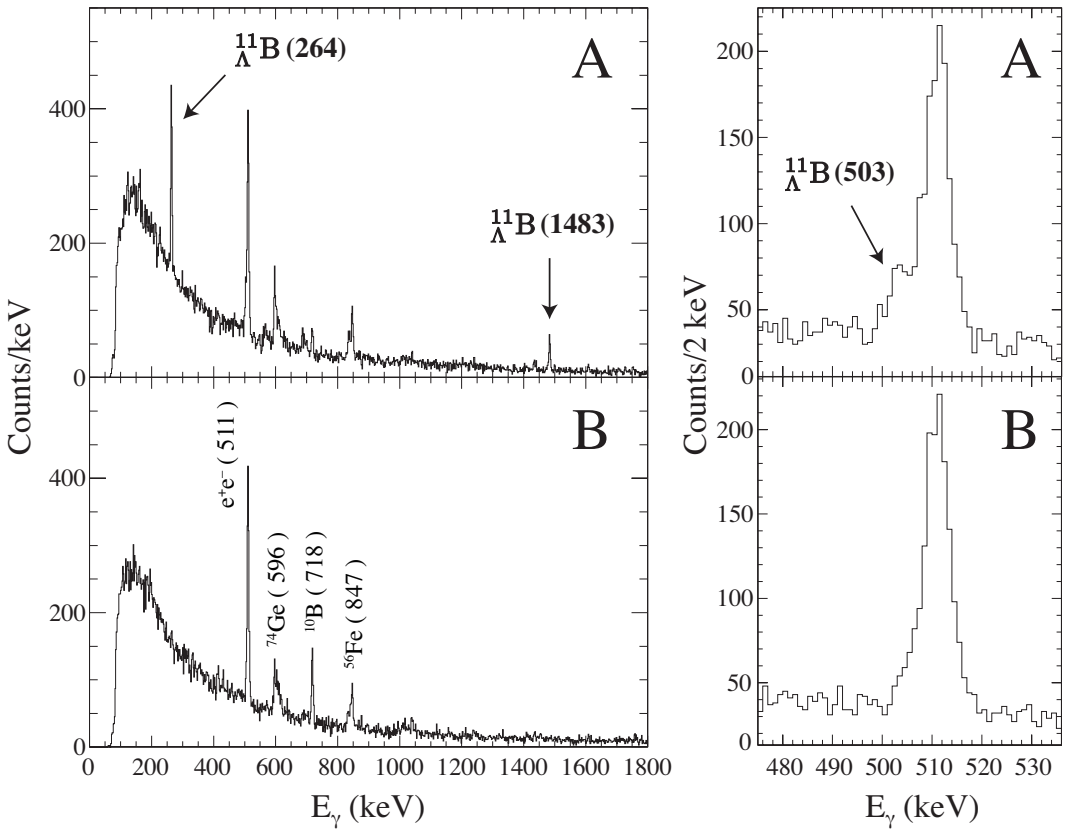

Figure 5.2: γ-ray spectra in coincidence with the ^{12}C(π^+, K^+) reaction. "A" indicates the spectrum for the events of $^{11}_{\Lambda}$B production selected in the missing mass spectrum. The spectrum "B" is obtained by selecting non-hypernuclear events. Right figures are the enlarged views of the left figures around the 511-keV peak. We can see three γ-ray peaks associated with $^{11}_{\Lambda}$B production.

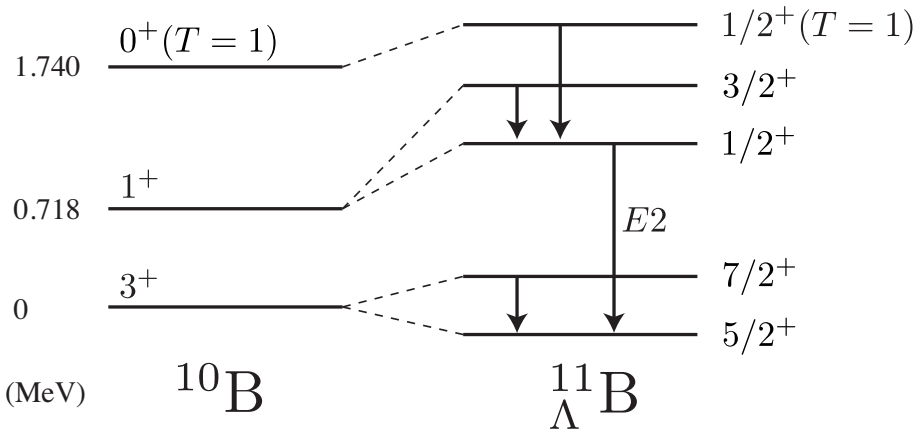

Figure 5.3: Low-lying level scheme of $^{11}_{\Lambda}$B. Possible γ-ray transitions in the E566 experiment are shown.

5.1.3 264-keV γ ray

Level assignment

Figure 5.3 shows the low-lying level scheme of ${}^{11}_{\Lambda}$B, where expected transitions are illustrated. In the weak coupling scheme, the ${}^{11}_{\Lambda}$B hypernuclear structure can be understood as a Λ hyperon coupling with the ^{10}B nuclear core. From the KEK-E518 results, the ${}^{11}_{\Lambda}$B$(1/2^+)$ state energy found to be too high to be populated through the one proton emission of the ${}^{12}_{\Lambda}$C$(2^+_1, 2^+_2, 0^+)$ states, which are dominant components of the p_Λ peak in the missing mass spectrum. Thus, the most prominent hypernuclear γ-ray peak in the region "A" is attributed to the $M1(7/2^+ \to 5/2^+)$ transition.

Mass distribution in coincidence with γ rays

In order to confirm the assignment, we studied a missing mass distribution when the 264-keV γ-ray events were selected. Figure 5.4 (b) shows the γ-energy-gated mass distribution. The gated γ-ray energy is 264 ± 4 keV as illustrated by red line in Figure 5.4 (a). In the figure (b), the hatching spectrum is an expected background contamination which is estimated by the side-band events in the hatching region of the figure (a). The background spectrum is scaled so that both spectra have the same event counts in the highly excited region (20 MeV $< -B_\Lambda <$ 60 MeV). Figure 5.4 (c) shows a difference between the γ-gated spectrum and the background spectrum. The difference spectrum is well explained by the simulated p_Λ peak which is shown in red in the figure (c). This result strongly supports the assignment of the 264-keV peak to the $M1(7/2^+ \to 5/2^+)$ transition. The p_Λ peak energy is obtained to be

$$\begin{aligned} B_\Lambda &= -0.51 \pm 0.13(\text{stat}) \text{ MeV}. \\ (\text{cf.} &\quad 0.10 \pm 0.04 \text{ MeV in KEK-E369}) \end{aligned}$$

γ-ray energy

We determined the γ-ray energy of the $M1(7/2^+ \to 5/2^+)$ transition by fitting the peak with a Gaussian plus a linear background as shown in Figure 5.5. The fitting result is 263.7 ± 0.1 keV, where the error is statistical. Taking the calibration error into account, the γ-ray energy is obtained to be

$$\begin{aligned} M1(7/2^+ \to 5/2^+) : E_\gamma &= 263.7 \pm 0.1(\text{stat}) \pm 1.0(\text{syst}) \text{ keV}. \\ (\text{cf.} &\quad 263.6 \pm 0.5 \pm 1.1 \text{ keV in KEK-E518}) \end{aligned}$$

The peak width agrees with the detector resolution.

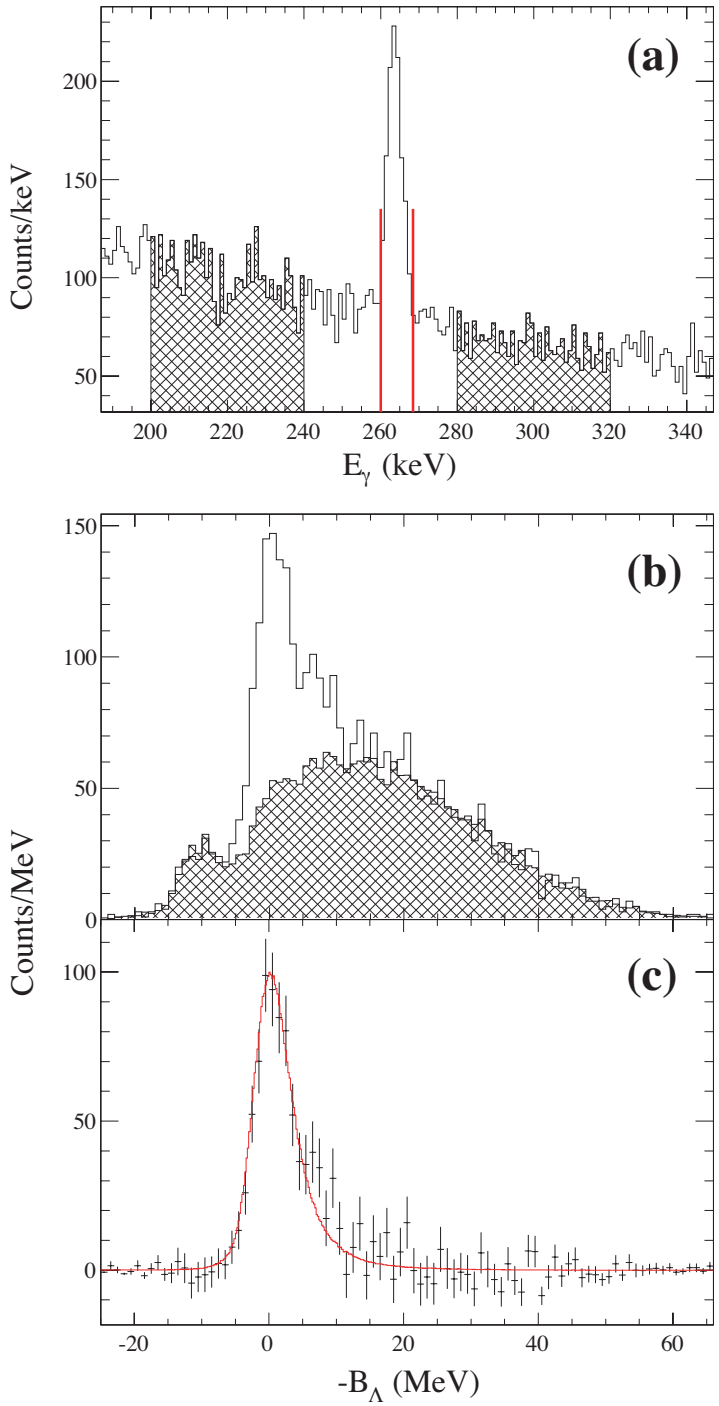

Figure 5.4: (a): γ-ray spectrum for $^{11}_{\Lambda}$B hypernuclear events. (b): Missing mass spectra with and without selection of 264-keV γ ray. (c): The difference of the two mass spectra in figure (b).

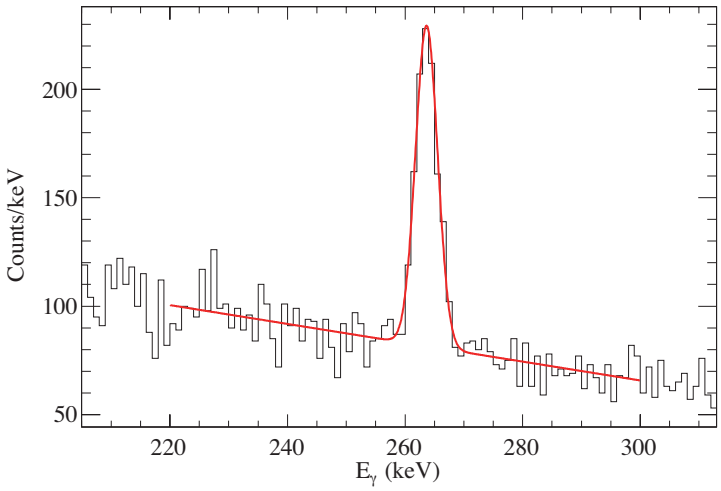

Figure 5.5: The fitting result for the 264-keV peak from ${}^{11}_{\Lambda}$B. The peak is fitted with a Gaussian plus a linear background. The goodness-of-fit statistic was obtained to be $\chi^2/DOF = 68.5/75$.

5.1.4 503-keV and 1483-keV γ rays

Level assignment

The 1483-keV γ ray was observed as a narrow peak without Doppler-shift correction. This narrow width indicates that a multipole order is $E2$ or higher because a lifetime of the transition is obtained to be much longer than the stopping time (~ 3 ps) of a recoiling hypernucleus. The $(1/2^+ \to 5/2^+)$ transition is the only $E2$ transition expected in ${}^{11}_{\Lambda}$B. Therefore, the 1483-keV peak was assigned to be the $E2(1/2^+ \to 5/2^+)$ transition. This assignment is consistent with the KEK-518 results.

The 503-keV peak is not clearly seen in the spectrum but an unnatural peak width of the 511-keV γ ray suggests the existence of this transition. In addition, this peak was confirmed as a separate peak in the KEK-E518 experiment. Two candidates are left for the 503-keV peak in Figure 5.3. The $M1(1/2^+; 1 \to 1/2^+)$ transition is expected to be very fast (11 fs) and should be Doppler broadened. The narrower peak width of the 503-keV γ ray excludes this possibility. Thus, the 503-keV γ ray is assigned to be the $M1(3/2^+ \to 1/2^+)$ transition. In this study, we used γ-γ coincidence technique for confirming this assignment.

We performed γ-γ coincidence with the 503-keV γ ray by taking a loose mass gate (-10 MeV $< -B_\Lambda <$ 15 MeV). As shown in Figure 5.6, we selected three regions at (a) 503 ± 3 keV, (b) 474 ± 3 keV and (c) 534 ± 3 keV. In the γ-γ coincidence spectrum with gate (a), a five-counts peak appears at 1485 ± 5 keV. Considering the probability of obtaining five background events in the narrow region of 1485 ± 5 keV, this five-

counts peak is certainly coincidence with the 503-keV γ ray. This result indicates that the 1483-keV γ ray is a cascading transition of the 503-keV γ ray. Therefore, the 503-keV γ ray is assigned to be the $M1(3/2^+ \to 1/2^+)$ transition.

The probability of finding a five-counts peak caused by accidental background is estimated as follows. The average background level between 1000 keV and 2000 keV in the coincidence spectrum is estimated by selecting a wide coincidence gate. When we gate the 600 keV $< E_\gamma <$ 1000 keV region, 339 events are obtained in the coincidence spectrum. There are 13490 counts in the 600 keV $< E_\gamma <$ 1000 keV region of the original γ-ray spectrum. For the 503 ± 3 keV gate where 763 counts exist in the original spectrum, the number of background events is expected to be $763 \times (339/13490) = 19.2$. Then we obtain the expected background counts within $\pm$5 keV region in the coincidence spectrum to be 19.2 $\times$ (10 keV/1000 keV)=0.19. Using a Poisson distribution, the probability of finding more than 5 counts in a 10 keV width by random fluctuation is calculated to be 4.5×10^{-5}.

γ-ray energy

The 1483-keV peak was fitted with a Gaussian plus a constant. For the fitting of the two peaks around 511 keV, we used two types of peak functions and a linear background function. One was the real response function taken from the measured 511-keV peak shape because it was asymmetrically broadened due to the in-flight annihilation. The other was a Gaussian function for the 503-keV peak shape. The fitting results are shown in Figure 5.7. Considering the calibration error, we determined their energies to be

$$\begin{aligned} M1(3/2^+ \to 1/2^+) : E_\gamma &= 503.0 \pm 0.4(\text{stat}) \pm 1.0(\text{syst}) \text{ keV}, \\ &\text{(cf. } 504.7 \pm 1.0 \pm 1.1 \text{ keV in KEK-E518)} \\ E2(1/2^+ \to 5/2^+) : E_\gamma &= 1483.3 \pm 0.3(\text{stat}) \pm 1.0(\text{syst}) \text{ keV}. \\ &\text{(cf. } 1483.3 \pm 0.2 \pm 0.7 \text{ keV in KEK-E518)} \end{aligned}$$

The widths of the 503-keV and 1483-keV peaks are explained by the intrinsic detector resolution. This fact means that their transition life times are much faster than stopping time ($\sim$3 ps) of the recoiling hypernuclei. These non-Doppler-broadened peak shapes are also consistent with the KEK-E518 results.

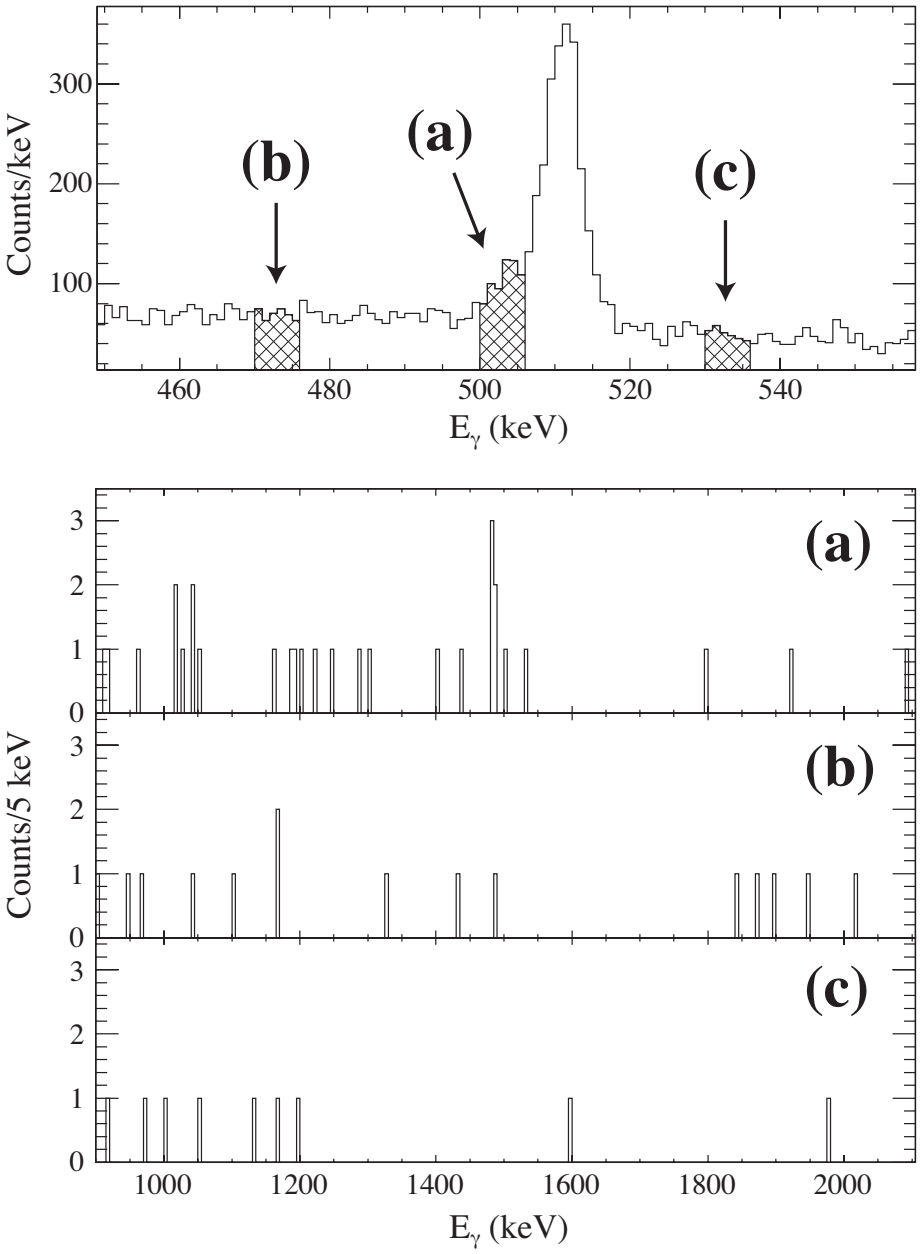

Figure 5.6: Upper figure shows the gated energy for γ-γ coincidence, where (a) corresponds to the $M1(3/2^+ \rightarrow 1/2^+)$ transition and the others are background regions. Lower three figures show γ-ray spectra around 1483-keV peak in coincidence with the (a), (b) and (c) regions.

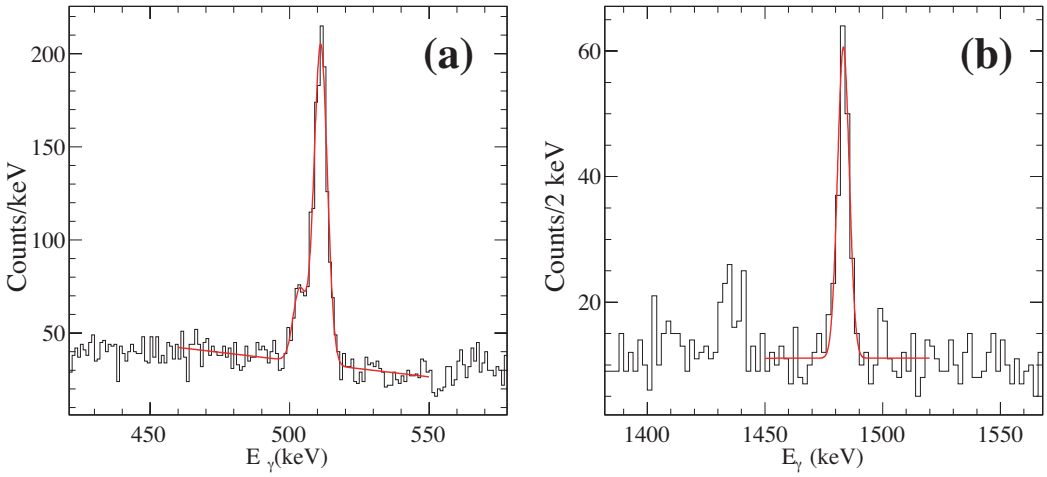

Figure 5.7: (a): Fitting result of the two peaks around 511 keV with two peak functions plus a linear background. One is a Gaussian function for the 503-keV peak shape. The other is the real response function taken from the measured 511-keV peak shape. The goodness-of-fit statistic was obtained to be $\chi^2/DOF = 96.4/103$. (b): Fitting result of 1483-keV peak with a Gaussian plus a constant. The peak around 1435 keV comes from ^{10}B (1433 or 1436 keV). The goodness-of-fit statistic was obtained to be $\chi^2/DOF = 32.9/31$.

Mass distribution in coincidence with γ rays

We also studied mass distribution for 503-keV or 1483-keV γ ray events. The analysis process was the same as that of the 264-keV γ ray except for the gate energy, which was 503 ± 3 keV or 1483 ± 4 keV. Figure 5.8 shows the results. For the 503-keV gate, it seems that events around $-B_\Lambda = 0 \sim 10$ MeV and $-B_\Lambda = 20 \sim 30$ MeV are enhanced though the signal-to-noise ratio is not sufficient. On the other hand, we succeeded in observing a sharp peak in the missing mass spectrum for the 1483-keV gate after subtracting background. The peak was well fitted with the simulated response function, where we assumed only one peak component. As a result, we determined the peak energy to be

$$B_\Lambda \;=\; -4.93 \pm 0.17(\text{stat}) \text{ MeV}.$$

This peak was not observed in the KEK-E369 experiment due to a large contamination of the quasi-free continuum. The property of this peak is discussed in the next chapter.

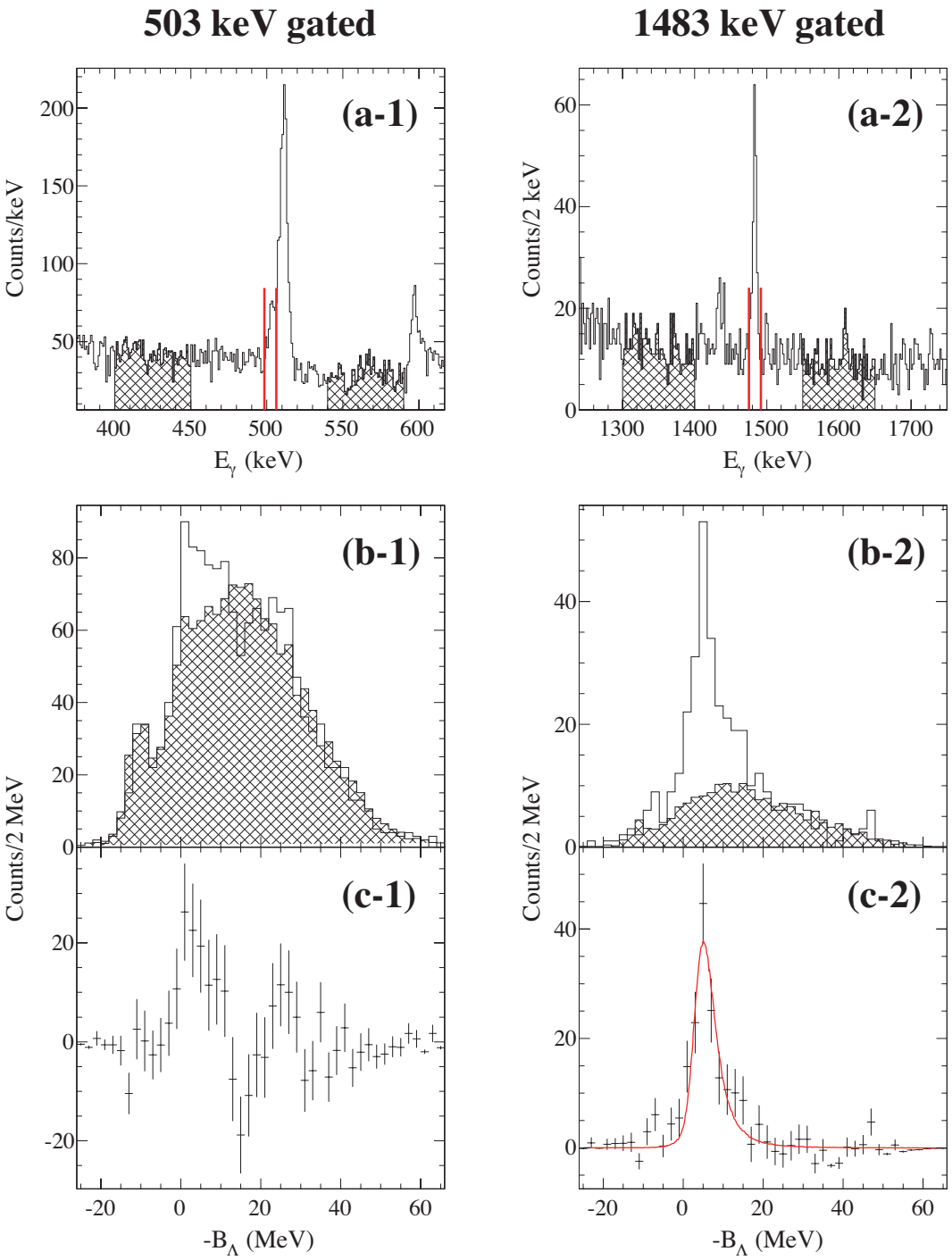

Figure 5.8: (a): γ-ray spectrum for $^{11}_{\Lambda}$B hypernuclear events. (b): Missing mass spectra with and without selection of γ-ray energy. (c): The difference of the two mass spectra in figure (b).

5.2 γ-ray spectroscopy of ${}^{12}_{\Lambda}$C

5.2.1 Mass selection

According to the KEK-E369 results, observation of four $M1$ transitions is expected in the present experiment as illustrated in Figure 5.9. In the (π^+, K^+) reaction at 1.05 GeV/c, the production ratio of the 2^-_1 to the 1^-_1 state is calculated to be a few % due to a small spin-flip amplitude [38]. Thus, all of the four γ rays should be caused by the core-excited states (1^-_2, 1^-_3) of ${}^{12}_{\Lambda}$C, which have configuration of the ^{11}C excited states ($1/2^-$, 2.00 MeV and $3/2^-$, 4.80 MeV) and a Λ in the s orbit.

We selected the core-excited s_Λ state region in the missing mass spectrum based on the simulated s_Λ peak shape in order to search for these γ rays. As shown in Figure 5.10, "C" is selected for the core-excited s_Λ state region (-12 MeV $< -B_\Lambda <$ -2 MeV), and "B" is a highly unbound region ($-B_\Lambda > 25$ MeV) in which a hypernucleus is not expected to be produced. The narrow mass-gate width of the region "C" was determined to reduce background events from the ground state and the p_Λ states decaying to ${}^{11}_{\Lambda}$B.

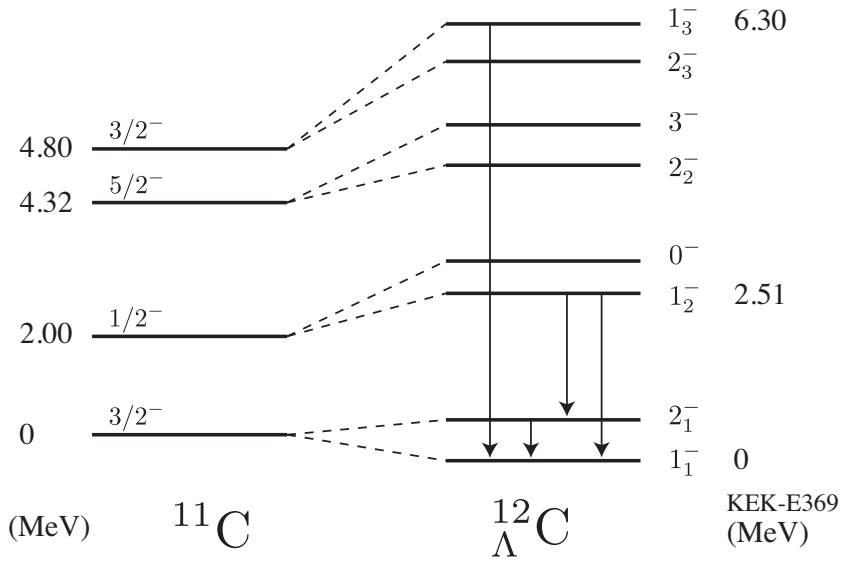

Figure 5.9: Level scheme of ${}^{12}_{\Lambda}$C. Expected γ-ray transitions in the E566 experiment are shown.

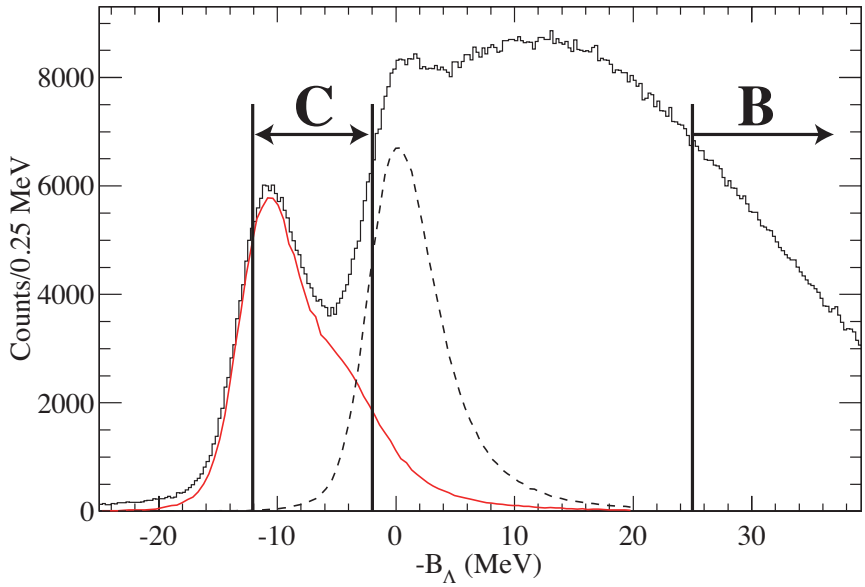

Figure 5.10: Missing mass spectrum of $^{12}_{\Lambda}$C. We selected the region "C" for the core-excited states of $^{12}_{\Lambda}$C. Events of the highly unbound region "B" is not associated with the hypernucleus production.

5.2.2 γ-ray spectra

Figure 5.11 shows γ-ray spectra plotted in the range below 1.6 MeV with the mass selection of "C" and "B" without Doppler-shift correction. A peak at 162 keV is observed only in the region "C" spectrum. In order to search for M1 transition γ rays which should be Doppler broadened, we applied Doppler-shift correction to the measured γ-ray energy based on the momentum vector of the recoiling hypernucleus. Figure 5.12 and Figure 5.13 show γ-ray spectra before and after the Doppler-shift correction. Three narrow peaks at 2670 keV, 2839 keV and 6048 keV are observed in the Doppler-corrected γ-ray spectra with the mass gate of "C". Their peak properties are obtained by fitting and results are summarized in Table 5.2.

These four γ rays are attributed to ${}^{12}_{\Lambda}$C and detailed descriptions about them are given in the following subsections.

Table 5.2: Peak properties of the ${}^{12}_{\Lambda}$C γ rays observed in the mass region "C". The quoted error is only statistical. The entry of Est. FWHM stands for the expected resolution (see Section 4.6.2).

Peak Energy (keV)	FWHM (keV)	Est. FWHM (keV)	Yield
161.5 ± 0.3	4.2 ± 0.6	3.6	215 ± 28
2670.2 ± 2.9	fixed		76 ± 12
2839.3 ± 3.6	fixed		30 ± 8
6048.4 ± 6.8	fixed		21 ± 7

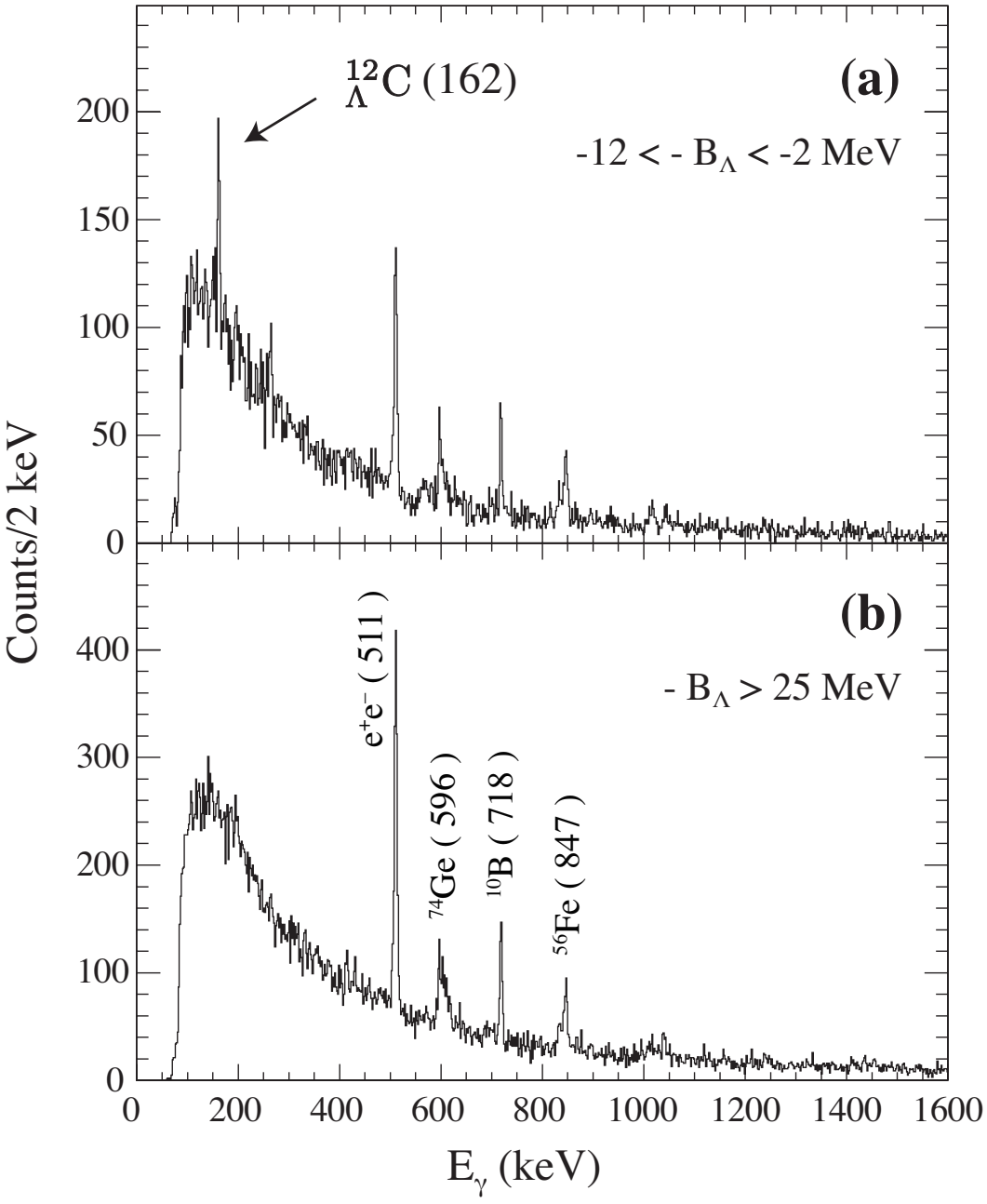

Figure 5.11: Mass-gated γ-ray spectra below 1.6 MeV without Doppler correction. (a): Spectrum for the core-excited s_Λ region of $^{12}_{\Lambda}$C. (b): Spectrum for the highly unbound region.

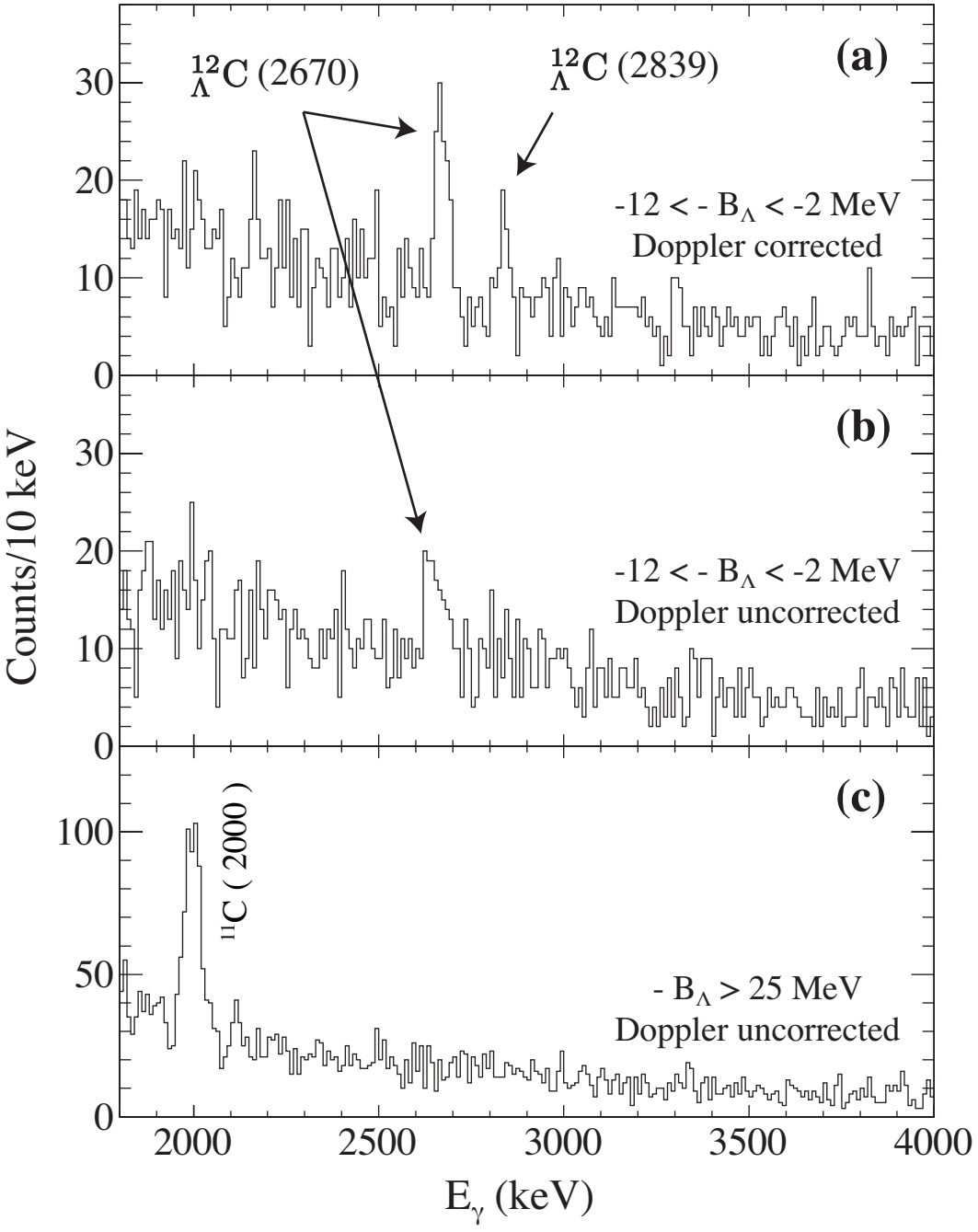

Figure 5.12: Mass-gated γ-ray spectra around 3 MeV. (a) and (b): Spectrum for the core-excited s_Λ region of $^{12}_{\Lambda}$C with and without Doppler-shift correction. (c): Doppler-uncorrected spectrum for the highly unbound region.

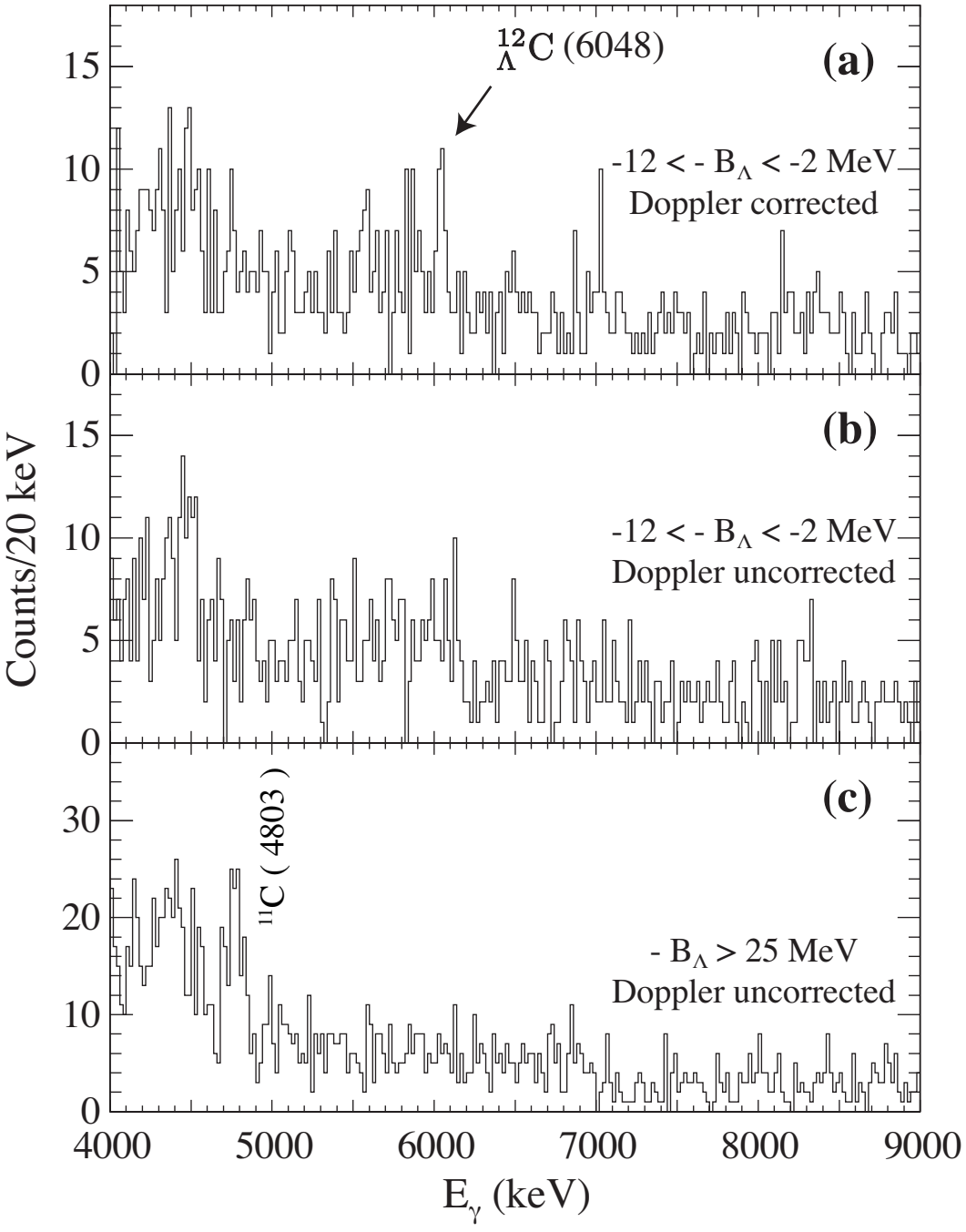

Figure 5.13: Mass-gated γ-ray spectra over 4 MeV. (a) and (b): Spectrum for the core-excited s_Λ region of $^{12}_{\Lambda}$C with and without Doppler-shift correction. (c): Doppler-uncorrected spectrum for the highly unbound region.

5.2.3 162-keV γ ray

Level assignment

Taking into account the γ-energy dependence of the Hyperball2 efficiency, the $M1$ transition between the ground state doublet members ($2^-_1 \rightarrow 1^-_1$) is expected to make the most prominent peak in the γ-ray spectrum with the gate of the core-excited s_Λ region. In addition, a γ-ray peak in this transition is expected not to be broadened by Doppler shift because the life time of 162-keV $M1$ transition is two orders of magnitude longer than the stopping time of the recoiling ${}^{12}_{\Lambda}$C hypernucleus inside the polyethylene target. Thus, the 162-keV γ ray is assigned to the $M1(2^-_1 \rightarrow 1^-_1)$ transition.

Mass distribution in coincidence with γ rays

Figure 5.14 shows the mass distribution for the 162-keV γ ray events, where the analysis method is the same as the ${}^{11}_{\Lambda}$B case. The γ-energy gate is set to be 162$\pm$4 keV as shown in the figure (a). The hatching spectrum in the figure (b) is an expected background contamination estimated by the side-band events in the hatching region of the figure (a). In the figure (c), simulated peak of the 1^-_2 state is illustrated by red line, where the vertical scale of the peak is arbitrary for a reference of its position. The upper components including the 1^-_2 state demonstrate that the 2^-_1 state of the ground-state doublets is populated by the subsequent deexcitation processes of the excited states. On the contrary, a lower component observed below the 1^-_2 state shows that the 2^-_1 state is also produced by the direct process of the (π^+, K^+) reaction. As shown in Figure 5.9, the 2^-_1 state is the only state which emits γ rays below the 1^-_2 state. Therefore, this mass distribution also support the assignment of the 162-keV γ ray to the transition between the ground-state doublet members. The detailed discussion of these population processes of the 2^-_1 state is given in the next chapter.

γ-ray energy

We determined the γ-ray energy of the $M1(2^-_1 \rightarrow 1^-_1)$ transition by fitting the 162-keV peak with a Gaussian plus a linear background as shown in Figure 5.15. The fitting result shows

$$M1(2^-_1 \rightarrow 1^-_1) : E_\gamma \;=\; 161.5 \pm 0.3(\text{stat}) \pm 1.0(\text{syst}) \text{ keV},$$

where systematic error is taken from the calibration error. The peak width agrees with the detector resolution.

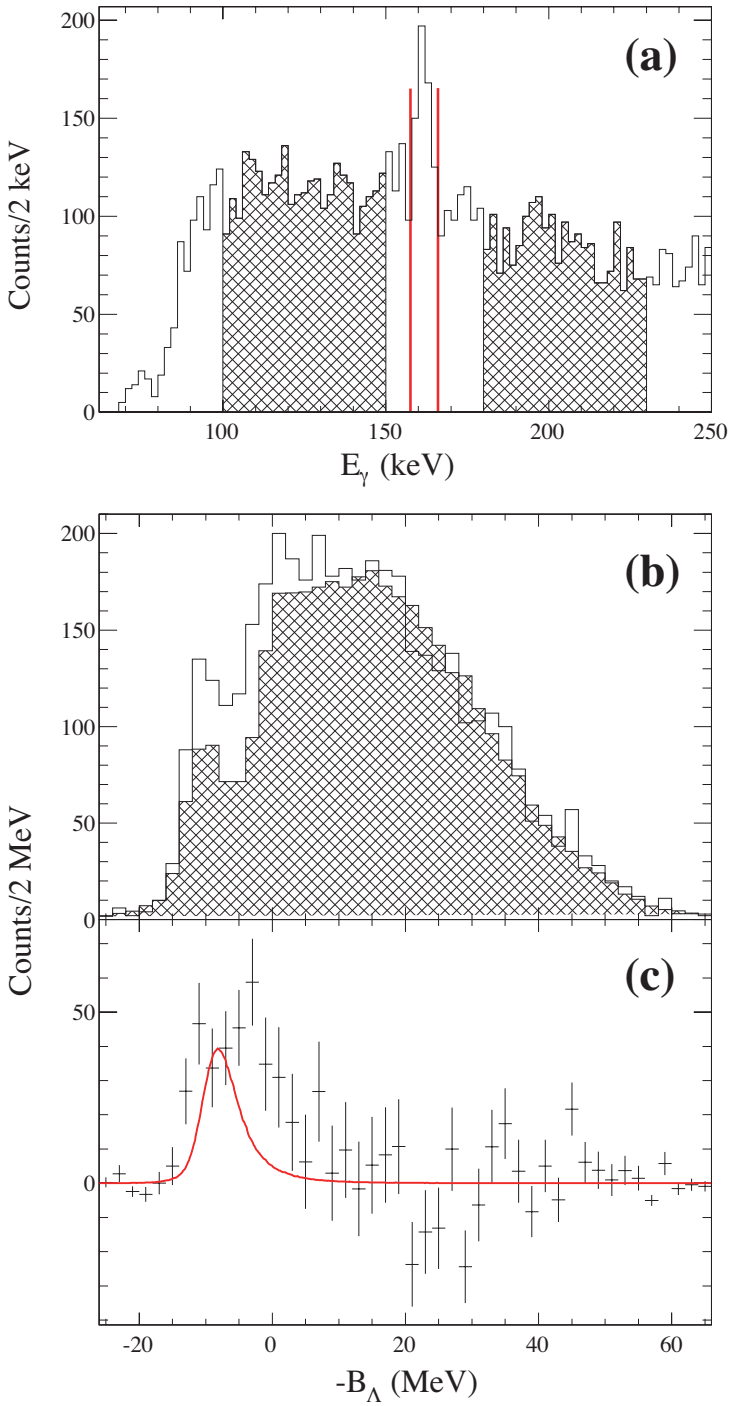

Figure 5.14: (a): γ-ray spectrum for $^{12}_{\Lambda}$C hypernuclear events. (b): Missing mass spectra with and without selection of 162-keV γ ray. (c): The difference of the two mass spectra in figure (b).

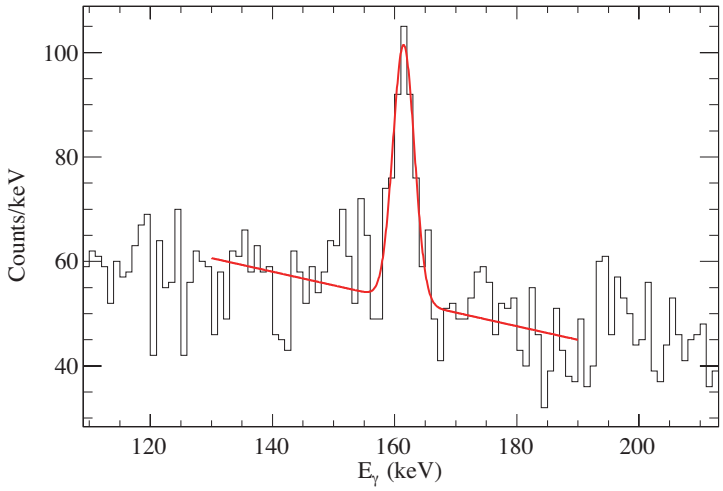

Figure 5.15: The fitting result for the 162-keV peak from ${}^{12}_{\Lambda}$C. Doppler correction is not applied to the spectrum. The peak is fitted with a Gaussian plus a linear background. The goodness-of-fit statistic was obtained to be $\chi^2/DOF = 61.3/55$.

5.2.4 2.7-MeV and 2.8-MeV γ rays

Level assignment

The 2.7-MeV and the 2.8-MeV γ rays are observed as narrow peaks after Doppler correction, and they are candidates of the $M1$ transitions from the upper 1^-_2 state to the ground state doublets. The branching ratio of the $M1(1^-_2 \to 2^-_1)$ transition and the $M1(1^-_2 \to 1^-_1)$ transition is expected to be 3:1 in the weak coupling limit and 8:2 in the shell model calculation [39]. Because the 2.7-MeV peak has a relatively large γ-ray yield compared with the 2.8-MeV peak, the 2.7-MeV peak is assigned to the $M1(1^-_2 \to 2^-_1)$ transition. Then, the 2.8-MeV peak is assigned to the $M1(1^-_2 \to 1^-_1)$ transition.

Mass distribution in coincidence with γ rays

Figure 5.16 shows the mass distribution for the 2.7-MeV and the 2.8-MeV γ ray events, where gated energies are 2670±30 keV and 2839±30 keV. A sharp peak corresponding to the 1^-_2 state appears in the mass spectrum after background subtraction. As illustrated by red line, the spectrum agrees with the simulated peak shape. This result confirms that these two γ rays correspond to the transitions from the 1^-_2 state. The peak energy is obtained to be

$$\begin{aligned} B_\Lambda &= 7.84 \pm 0.32(\text{stat}) \text{ MeV}. \\ (\text{cf.} &\quad 8.25 \pm 0.17 \text{ MeV in KEK-E369}) \end{aligned}$$

γ-ray energy

The Doppler corrected γ-ray spectrum around 2.7-MeV region is fitted by using the simulated peak shapes and some background functions. The peak widths observed after Doppler-shift correction are well reproduced by the simulated shapes. The fitting is performed with the maximum likelihood method due to low statistics of the data. As shown in Figure 5.17, three types of background functions are tested, such as a constant background, a linear background and a smoothed step function. For the γ-ray energy region over 2 MeV, the multi-Compton effect which increases the background only on the low-energy side of the peak is expected to be more pronounced. In this fitting, the multi-Compton background for the prominent peak of 2667-keV γ ray is reproduced by using a smoothed step function as

$$y = A \times EFRC\left(\frac{x - E_0}{\sqrt{2\sigma^2}}\right) + B \ ,$$

where A and B are parameters, E_0 is the peak energy, σ is the standard deviation of the peak width and $EFRC$ is the complement of the error function. When a binned maximum likelihood fit is applied to the histogram which has many bins with low statistics less than 10 counts, chi-square values calculated by the sum of squares of fitting residuals are not reliable for the goodness-of-fit statistic because of the Poisson nature of the data. The "likelihood ratio $(-2\ln\lambda)$" calculated by

$$-2\ln\lambda = 2\sum_{i}^{N}\left(\mu_i - n_i + n_i \ln\frac{n_i}{\mu_i}\right)$$

is used for an approximation of chi-square equivalent values [41], where n_i is the content of the i-th bin and μ_i is the Poisson probability of n_i events with the mean value determined by the fitting function. In this situation, histograms to be fitted are required to have a moderate number of zero bins. At the limit of large samples, the distribution of the likelihood ratio is the same as that of the corresponding chi-square value. Thus, we evaluated the goodness-of-fit statistic by using

$$\chi^2/DOF \simeq -2\ln\lambda/DOF \ .$$

In the actual fitting routine, the minimum point of the likelihood ratio is searched for by changing parameters and "1 sigma" uncertainties of the parameters are defined at the point where $-2\ln\lambda \rightarrow -2\ln\lambda + 1$.

From the goodness-of-fit statistic, the interpretation with a constant background is rejected but the other two background functions are equivalent. In order to obtain

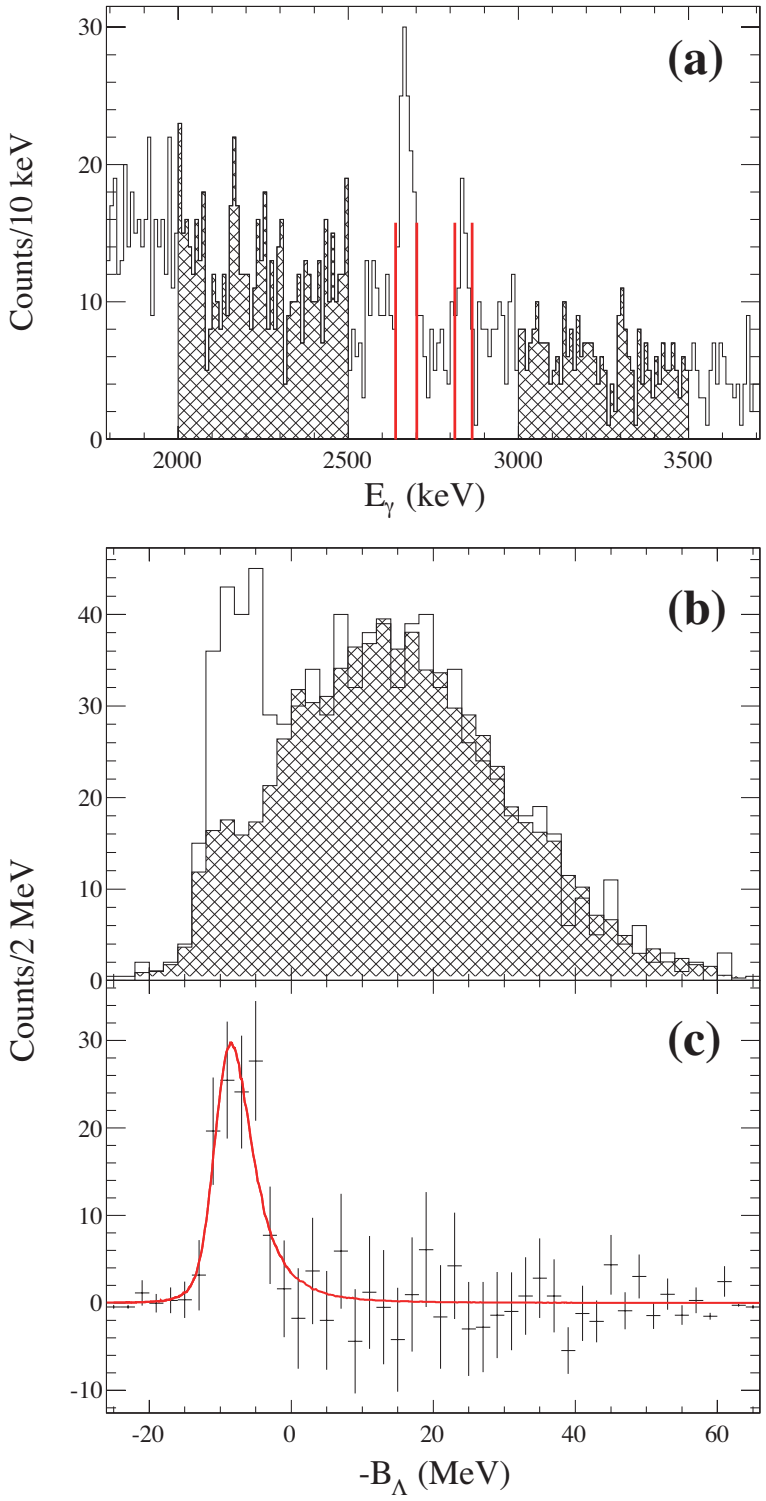

Figure 5.16: (a): γ-ray spectrum around 3 MeV for ${}^{12}_{\Lambda}$C hypernuclear events. (b): Missing mass spectra with and without selection of the 2.7-MeV and the 2.8-MeV γ rays. The hatching spectrum shows background contamination estimated by the side-band events in the hatching region of the figure (a). (c): The difference of the two mass spectra in figure (b). The spectrum is fitted with a simulated response function.

a reliable fitting result, we take the average of several fitting results with a linear and a smoothed step functions, where bin biases of the histogram are also modulated. Then, the variation of these fitting results are taken into account for the systematic error. The energies of γ rays are obtained to be

$$\begin{aligned} M1(1_2^- \to 2_1^-) : E_\gamma &= 2670.2 \pm 2.9(\text{stat}) \pm 3.6(\text{syst}) \text{ keV}, \\ M1(1_2^- \to 1_1^-) : E_\gamma &= 2839.3 \pm 3.6(\text{stat}) \pm 3.2(\text{syst}) \text{ keV}, \end{aligned}$$

where the systematic error is dominated by uncertainty of Doppler correction. The energy difference of these transitions gives the ground state splitting energy as

$$\Delta E_\gamma = 169.1 \pm 4.8(\text{stat}) \pm 1.8(\text{syst}) \text{ keV},$$

where systematic errors from the Doppler correction and energy calibration are supposed to be canceled, and then the quoted systematic error is determined by uncertainty of the fitting. Although it has low precision, the ΔE_γ value is consistent with the γ-ray energy of the $M1(2_1^- \to 1_1^-)$ transition. The counts of γ rays are also found to be

$$\begin{aligned} M1(1_2^- \to 2_1^-) : \text{counts} &= 76 \pm 12(\text{stat}) \pm 1(\text{syst}) \ , \\ M1(1_2^- \to 1_1^-) : \text{counts} &= 30 \pm \ 8(\text{stat}) \pm 3(\text{syst}) \ . \end{aligned}$$

The observed yield ratio $(1_2^- \to 1_1^-)/(1_2^- \to 2_1^-) = 0.39 \pm 0.13$ supports our level assignment by comparing with the shell-model prediction (2/8=0.25) [39].

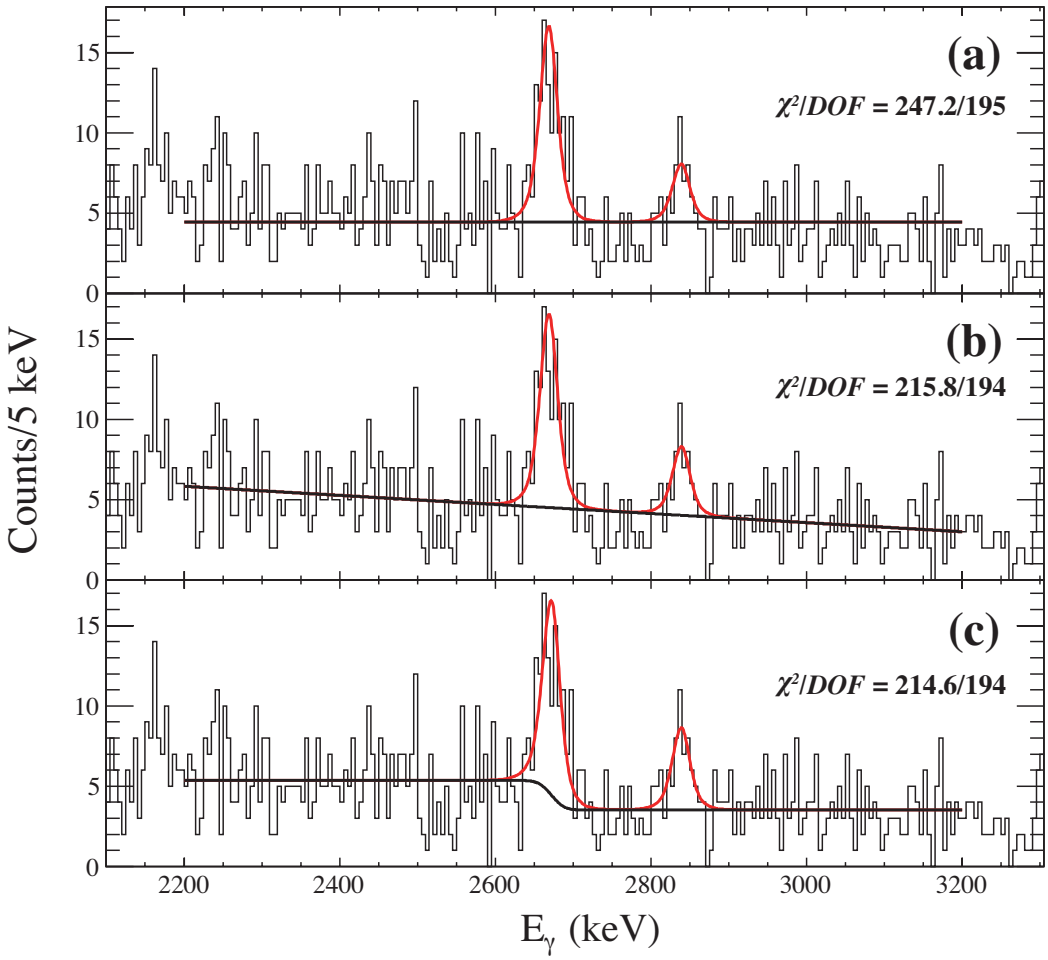

Figure 5.17: Fitting results of the Doppler-shift corrected γ-ray spectrum for the 2.7-MeV and 2.8-MeV peaks. The Doppler-corrected peak shapes are reproduced by the simulated response functions. Three types of background functions are tested, such as a constant background (a), a linear background (b) and a smoothed step function (c). Among them, the fitting result with a constant background is rejected because of the insufficient goodness-of-fit statistic. The others are equivalent.

5.2.5 6-MeV γ ray

Peak search for high energy γ-ray transitions

High energy γ-ray peaks were searched for by evaluating peak significance defined as

$$\text{Peak significance} = \frac{\text{number of peak count}}{\text{1 sigma error of peak count}} \ ,$$

where peak count was obtained by fitting with a Gaussian plus a constant background. In this fitting, Doppler-corrected peak shapes are approximated by the Gaussian with fixed width evaluated from the simulated response functions. Peak significance was successively measured as a function of γ-ray energy by 5-keV steps, where the peak position was constrained to the given energy. As a result of the peak search, we found three peaks with significance larger than 3 σ in the energy region over 2 MeV as shown in Figure 5.18 (b). When we perform a peak search with different bin widths of the histogram, such as 10 and 20 keV, peak significance is slightly changed but these three peaks are still kept over the 3-σ threshold. Two peaks denoted by γ_1 and γ_2 are identified as the $M1(1^-_2 \to 2^-_1)$ and $M1(1^-_2 \to 1^-_1)$ transitions respectively, which are discussed in the previous subsection. The fitting range of $E_\gamma \pm 100$ keV are determined so as to have a sufficient peak search sensitivity to the γ_2 peak. The remaining γ_3 peak at 6 MeV is also identified as a high energy γ ray associated with the ${}^{12}_{\Lambda}$C production.

γ-ray energy

For the fitting of the 6-MeV peak, we assumed two types of background lines by using a linear and a smoothed step functions. As shown in Figure 5.19, the observed peak shape is well reproduced by the simulated one, where the transition life time is supposed to be much faster than the stopping time. In addition, both background functions well fit to the γ-ray spectrum around 6 MeV. Thus, the fitting results with the two background functions are averaged and the variation of them are taken into account for the systematic error, where the variation caused by different bin biases are also considered. As a result, we obtained the γ-ray yield of $21 \pm 7(\text{stat}) \pm 1(\text{syst})$ counts and the peak energy of $6048.4 \pm 6.8(\text{stat}) \pm 6.7(\text{syst})$ keV. The systematic error of the energy is dominated by uncertainty of Doppler correction.

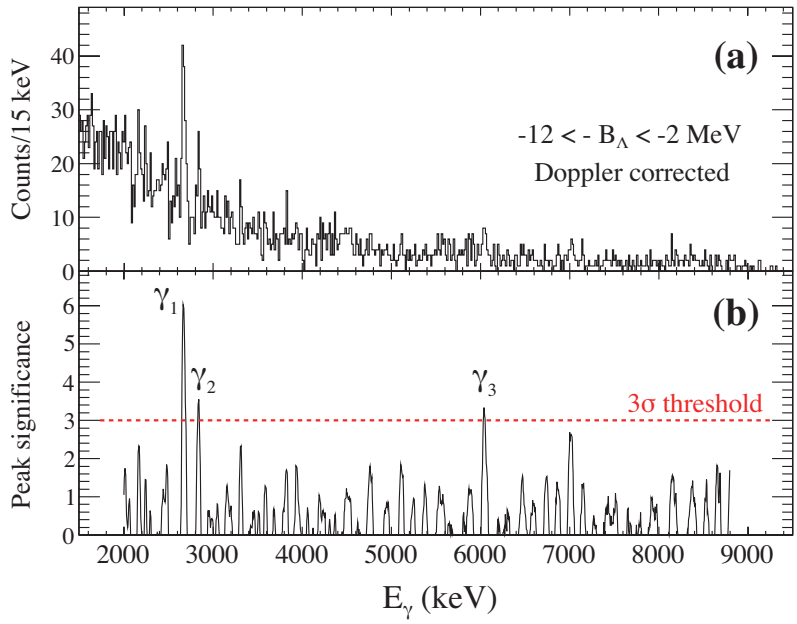

Figure 5.18: Peak search result for high energy γ-ray transitions. (a): Doppler-shift corrected γ-ray spectrum for the core-excited s_Λ region of ${}^{12}_{\Lambda}$C. Peak significance is measured by performing a constrained fitting with a Gaussian with fixed width plus a constant background. (b): Peak significance plot as a function of the γ-ray energy. Three peaks are obtained with significance lager than 3 σ.

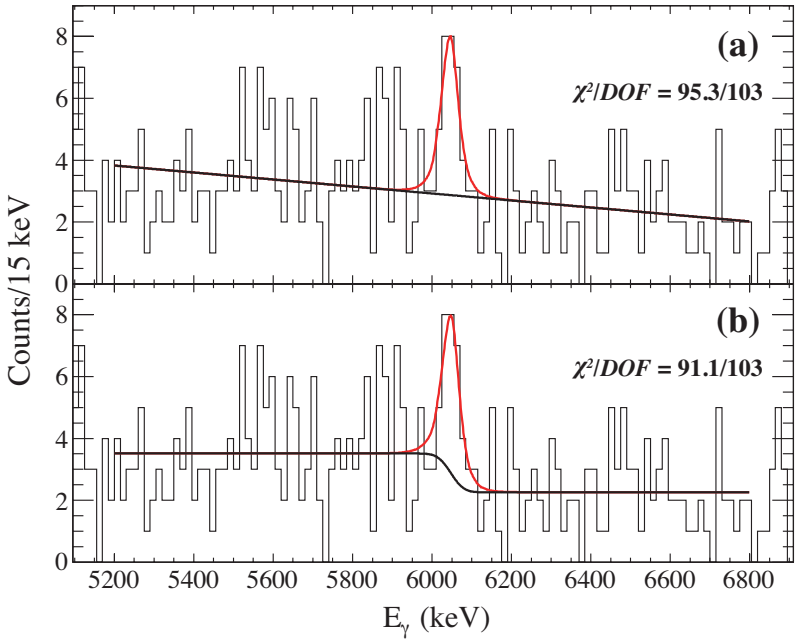

Figure 5.19: Fitting results of the Doppler-corrected γ-ray spectrum for the 6-MeV peak. The peak is fitted with a simulated peak shape plus a linear background (a) or a smoothed step function (b).

Level assignment

Since the γ-ray energy generally agrees with the excitation energy of the 1^-_3 state measured in the KEK-E369 experiment, the 6-MeV peak is the strongest candidate of the $M1(1^-_3 \rightarrow 1^-_1)$ transition. In addition, the missing mass spectrum in the present experiment reliably indicates a sizable population of the 1^-_3 state, without which we can not explain the mass spectrum. Thus, we have a chance to observe a transition from the 1^-_3 state.

The expected peak counts of the $M1(1^-_3 \rightarrow 1^-_1)$ transition in the present experiment is estimated by the following way. Firstly, the yield of the 1^-_2 state is calculated from the observed γ rays as

$$Y(1^-_2) = \frac{1}{\varepsilon_{mass}(1^-_2)} \cdot \left(\frac{I_\gamma(1^-_2 \rightarrow 2^-_1)}{\varepsilon_\gamma(2670\ \mathrm{keV})} + \frac{I_\gamma(1^-_2 \rightarrow 1^-_1)}{\varepsilon_\gamma(2839\ \mathrm{keV})} \right),$$

where $\varepsilon_{mass}(1^-_2)$ is the ratio of the 1^-_2 state events in the missing mass gate and ε_γ is the photo-peak efficiency of Hyperball2. The $I_\gamma(1^-_2 \rightarrow 2^-_1)$ and $I_\gamma(1^-_2 \rightarrow 1^-_1)$ are the peak counts of 2.7-MeV and 2.8-MeV γ rays, respectively. The $\varepsilon_{mass}(1^-_2)$ was evaluated from the simulated peak shape to be 84.2 %. Then, by using the ratio (R_σ) of the production cross sections between the 1^-_2 state and the 1^-_3 state measured in KEK-E369, the expected yield of the 1^-_3 state is given as

$$Y(1^-_3) = Y(1^-_2) \cdot R_\sigma\ .$$

Finally, we obtained the expected peak counts of

$$\begin{aligned} I_\gamma(1^-_3 \rightarrow 1^-_1) &= Y(1^-_3) \cdot \varepsilon_{mass}(1^-_3) \cdot BR(1^-_3 \rightarrow 1^-_1) \cdot \varepsilon_\gamma(6048\ \mathrm{keV}) \\ &= 32 \pm 8\ , \end{aligned}$$

where $BR(1^-_3 \rightarrow 1^-_1)$ is the branding ratio of the $M1(1^-_3 \rightarrow 1^-_1)$ transition. Considering E^3_γ dependence of $M1$ transitions, we modified a theoretically calculated branching ratio [39] based on the excitation energies of the ${}^{12}_{\Lambda}$C states determined by the γ rays. The $\varepsilon_{mass}(1^-_3)$ was 71.9 % in this study.

The observed peak count agrees with the expected one. In addition, the observed peak shape is also consistent with that of a $M1$ transition. Thus, we assigned the 6-MeV peak to the $M1(1^-_3 \rightarrow 1^-_1)$ transition. Although the observed yield is low, the 6-MeV peak is statistically significant.

5.3 Summary of observed γ-ray transitions

We observed totally seven hypernuclear γ-ray transitions in the γ-ray spectroscopy experiment with the ^{12}C(π^+, K^+) reaction.

For the $^{11}_{\Lambda}$B hypernucleus, their energies and assignments are

$$\begin{aligned} M1(7/2^+ \to 5/2^+) : E_\gamma &= 263.7 \pm 0.1(\text{stat}) \pm 1.0(\text{syst}) \text{ keV}, \\ M1(3/2^+ \to 1/2^+) : E_\gamma &= 503.0 \pm 0.4(\text{stat}) \pm 1.0(\text{syst}) \text{ keV}, \\ E2(1/2^+ \to 5/2^+) : E_\gamma &= 1483.3 \pm 0.3(\text{stat}) \pm 1.0(\text{syst}) \text{ keV}. \end{aligned}$$

For the $^{12}_{\Lambda}$C hypernucleus, their energies and assignments are

$$\begin{aligned} M1(2_1^- \to 1_1^-) : E_\gamma &= 161.5 \pm 0.3(\text{stat}) \pm 1.0(\text{syst}) \text{ keV}, \\ M1(1_2^- \to 2_1^-) : E_\gamma &= 2670.2 \pm 2.9(\text{stat}) \pm 3.6(\text{syst}) \text{ keV}, \\ M1(1_2^- \to 1_1^-) : E_\gamma &= 2839.3 \pm 3.6(\text{stat}) \pm 3.2(\text{syst}) \text{ keV}, \\ M1(1_3^- \to 1_1^-) : E_\gamma &= 6048.4 \pm 6.8(\text{stat}) \pm 6.7(\text{syst}) \text{ keV}. \end{aligned}$$

The excitation energies of the hypernuclear states are determined by applying the nuclear recoil correction to the observed γ-ray energies. By considering precision of the γ-ray energies, the 1_2^- excitation energy of $^{12}_{\Lambda}$C is determined from the summed energy of the cascading transitions $(1_2^- \to 2_1^- \to 1_1^-)$. These results are also summarized in the level schemes as illustrated in Figure 5.20 and Figure 5.21.

For the $^{11}_{\Lambda}$B hypernucleus, their excitation energies are

$$\begin{aligned} 7/2^+ : E_X &= 263.7 \pm 0.1(\text{stat}) \pm 1.0(\text{syst}) \text{ keV}, \\ 1/2^+ : E_X &= 1483.4 \pm 0.3(\text{stat}) \pm 1.0(\text{syst}) \text{ keV}, \\ 3/2^+ : E_X &= 1986.4 \pm 0.5(\text{stat}) \pm 1.4(\text{syst}) \text{ keV}. \end{aligned}$$

For the $^{12}_{\Lambda}$C hypernucleus, their excitation energies are

$$\begin{aligned} 2_1^- : E_X &= 161.5 \pm 0.3(\text{stat}) \pm 1.0(\text{syst}) \text{ keV}, \\ 1_2^- : E_X &= 2832.0 \pm 2.9(\text{stat}) \pm 3.7(\text{syst}) \text{ keV}, \\ 1_3^- : E_X &= 6050.0 \pm 6.8(\text{stat}) \pm 6.7(\text{syst}) \text{ keV}. \end{aligned}$$

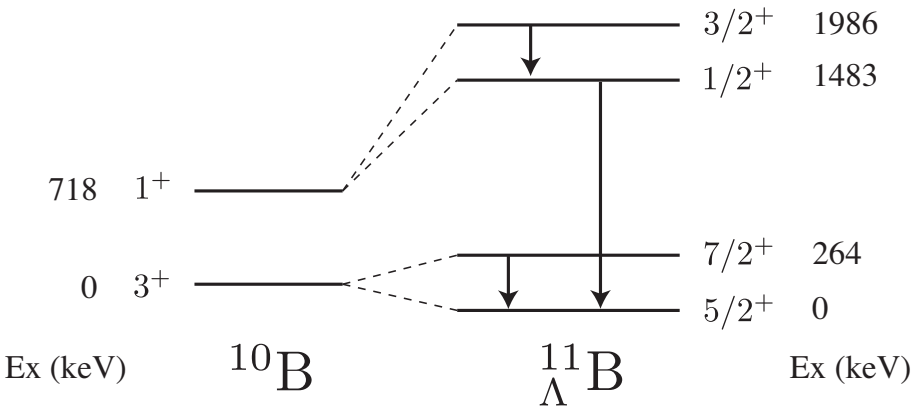

Figure 5.20: Level scheme of $^{11}_{\Lambda}$B with the observed transitions and the determined excitation energies.

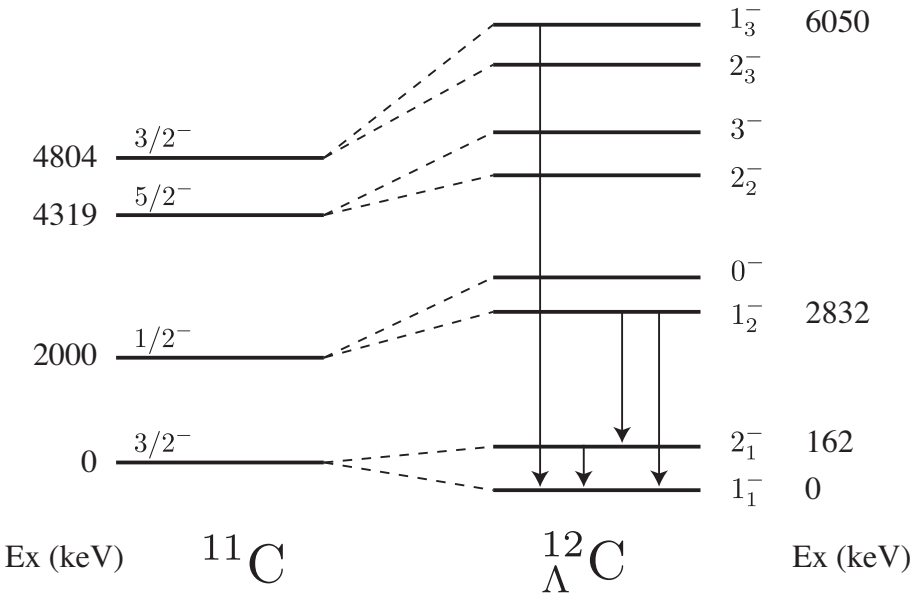

Figure 5.21: Level scheme of $^{12}_{\Lambda}$C with the observed transitions and the determined excitation energies.

5.4 Comparison with the previous analysis

In this section, the present analysis results are compared with the previous ones. The first analysis of the KEK-E566 data was performed by Dr. Y. Ma, and the results were reported in papers [42, 43]. The details of the previous analysis are also given in his Ph.D. thesis [44]. In the previous analysis, totally six hypernuclear γ-ray peaks were identified below 3-MeV energy region. By making a lot of improvements to the analysis procedures, those six γ-ray peaks have been confirmed with better sensitivity in the present analysis. Furthermore, we have succeeded in observing the 6-MeV peak from the ${}^{12}_{\Lambda}\mathrm{C}(1^-_3 \rightarrow 1^-_1)$ transition for the first time. Table 5.3 summarizes both the previous and the present analysis results.

The essential improvements of the present analysis are listed below.

- The (π^+, K^+) reaction vertex point along the beam axis was reconstructed with 3.5 cm (FWHM) resolution by fine-tuning tracking parameters.

- The better mass resolution of 6.0 MeV (FWHM) was achieved by applying a more realistic energy loss correction base on the simulation with GEANT4 code. In the previous analysis, the mass resolution was obtained to be ~ 7 MeV (FWHM).

- The γ-ray energy was determined with more precise calibration curves. In addition, the systematic shifts of γ-ray energy during the in-beam period were corrected for by adjusting the energy of annihilation peak at 511 keV.

- The γ-ray yields increased by sophisticating analysis procedures and conditions for event selections. Moreover, the γ-ray spectrum with a better signal-to-noise ratio was obtained by selecting the hypernuclear mass region based on the simulated response functions. For instance, the significance of the 2.8-MeV peak was improved from 2.7 σ to 3.5 σ.

- Strong supports for γ-ray level assignments were newly implemented by using the γ-gated mass distributions.

Table 5.3: Summary of the γ-ray energies obtained by the previous and the present analyses. The quoted errors are statistical.

			E_γ (keV)	
	Transition	Multipole	Previous [43]	Present
${}^{11}_{\Lambda}$B	$7/2^+ \to 5/2^+$	$M1$	262.9 ± 0.2	263.7 ± 0.1
	$3/2^+ \to 1/2^+$	$M1$	503.9 ± 0.7	503.0 ± 0.4
	$1/2^+ \to 5/2^+$	$E2$	1482.9 ± 0.4	1483.3 ± 0.3
${}^{12}_{\Lambda}$C	$2^-_1 \to 1^-_1$	$M1$	161.4 ± 0.7	161.5 ± 0.3
	$1^-_2 \to 2^-_1$	$M1$	2670.2 ± 2.6	2670.2 ± 2.9
	$1^-_2 \to 1^-_1$	$M1$	2833.9 ± 5.6	2839.3 ± 3.6
	$1^-_3 \to 1^-_1$	$M1$	-	6048.4 ± 6.8

Chapter 6

Discussion

We succeeded in observing three γ-ray transitions from ${}^{11}_{\Lambda}$B and four transitions from ${}^{12}_{\Lambda}$C in the γ-ray spectroscopy via the ^{12}C(π^+, K^+) reaction. By adding these transitions, 21 γ-ray data in total for p-shell hypernuclei are available at present. The six transitions among them are newly given by the present experiment. In this chapter, we will discuss interpretation of these hypernuclear γ rays in terms of the parametrized effective ΛN interaction and the effect of ΛN-ΣN coupling. A discussion on the ${}^{12}_{\Lambda}$C mass spectra with gating γ transitions is also given in the last part.

6.1 ΛN interaction in p-shell hypernulei

6.1.1 Energy spacings of spin doublets

As mentioned in Chapter 1, energy spacings of hypernuclear spin-doublet states are essential for investigating the spin-dependent ΛN interaction. In the present experiment, we experimentally revealed three spin-doublet spacings of ${}^{11}_{\Lambda}$B$(3/2^+, 1/2^+)$, ${}^{11}_{\Lambda}$B$(7/2^+, 5/2^+)$ and ${}^{12}_{\Lambda}$C$(2^-_1, 1^-_1)$ for the first time. Recently, Millener has updated his calculations based on these new results and suggested that two sets of parameters are necessary for a consistent description of the doublet spacings over the p-shell hypernuclei [47]. A set of parameters for ${}^{7}_{\Lambda}$Li and ${}^{9}_{\Lambda}$Be is proposed as

$$\Delta = 0.430, \;\; S_\Lambda = -0.015, \;\; S_N = -0.390, \;\; T = 0.030 \;\; \text{MeV} \, , \tag{6.1}$$

and another set of parameters for the heavier p-shell hypernuclei (A=10-16) is proposed as

$$\Delta = 0.330, \;\; S_\Lambda = -0.015, \;\; S_N = -0.350, \;\; T = 0.0239 \;\; \text{MeV} \, . \tag{6.2}$$

According to Millener's calculations [45, 46, 47], we summarized the contributions from each of the ΛN spin-dependent interactions and the effect of ΛN-ΣN coupling to all of the experimentally available doublet spacings in Table 6.1, where energies are given in keV. The ground-state doublet spacings of ${}^{10}_{\Lambda}\mathrm{B}(2^-, 1^-)$ and ${}^{15}_{\Lambda}\mathrm{N}(1/2^+_1, 3/2^+_1)$ have not been observed so far in the experiments but upper limits were obtained. As can be seen from Table 6.1, the energy spacings of the spin doublets are quite well explained by the parametrized effective ΛN interaction once we accept two sets of the parameters depending on the mass number. We have not understood a reason for the A-dependence of the parameters, especially for the Δ term, but Millener gives a conjecture that shell-model admixtures beyond $0\hbar\omega$ for the lightest p-shell nuclei (^{6}Li in particular) involve mainly excitations from the s-shell to p-shell, thus permitting an active role for $s_N s_\Lambda$ matrix elements which are larger than those for $p_N s_\Lambda$. For A=10 and beyond, higher admixtures involve excitations from the p-shell to the sd-shell and bring in smaller ΛN matrix elements.

In this situation, previous inconsistency on the ground-state doublet spacing of ${}^{10}_{\Lambda}\mathrm{B}$ is resulted from the relatively large value of $\Delta = 0.43$ MeV. This value is determined from the energy spacing of the ${}^{7}_{\Lambda}\mathrm{Li}(3/2^+, 1/2^+)$ doublet but is not suitable for the heavier p-shell hypernuclei. The ground-state doublet spacing of ${}^{15}_{\Lambda}\mathrm{N}$ is also the same case. In order to confirm this consistent description of the p-shell hypernuclear doublets, the energy spacings of ${}^{10}_{\Lambda}\mathrm{B}(2^-, 1^-)$ and ${}^{15}_{\Lambda}\mathrm{N}(1/2^+_1, 3/2^+_1)$ are strongly expected to be observed as a γ ray of 80-100 keV.

It is also pointed out that the effect of ΛN-ΣN coupling is essential to the consistent description of the doublet spacings over the p-shell hypernuclei even though the effect is smaller than that for s-shell hypernuclei. For most of the spin-doublet spacings, the Δ value is roughly 10 times larger than the $\Lambda\Sigma$ value and both values have the same sign. Therefore, we focus on the ${}^{12}_{\Lambda}\mathrm{C}(2^-_1, 1^-_1)$ spacing where the $\Lambda\Sigma$ value is expected to be comparable to the Δ contribution. The experimental result in which we obtained the relatively large energy spacing is well explained by the $\Lambda\Sigma$ value calculated from the NSC97f interaction. This strongly suggests that the ΛN-ΣN component of the NSC97f interaction is reasonable.

Table 6.1: Summary of spin-doublet spacings in p-shell hypernuclei. Energies are given in keV. The top three entries are calculated using the parameters in Eq. 6.1. The other entries are calculated with the parameters in Eq. 6.2. The coefficients and the ΛΣ values are calculated by Millener's shell model [45, 46, 47]. The present experimental results are marked with asterisks.

	J_u^π	J_l^π	ΛΣ	Δ	S_Λ	S_N	T	ΔE^{th}	ΔE^{exp}
${}^{7}_{\Lambda}$Li	$3/2^+$	$1/2^+$	72	628	−1	−4	−9	693	692
${}^{7}_{\Lambda}$Li	$7/2^+$	$5/2^+$	74	557	−32	−8	−71	494	471
${}^{9}_{\Lambda}$Be	$3/2^+$	$5/2^+$	−8	−14	37	0	28	44	43
${}^{10}_{\Lambda}$B	2^-	1^-	−14	188	−21	−3	−26	124	< 100
${}^{11}_{\Lambda}$B	$7/2^+$	$5/2^+$	56	339	−37	−10	−80	267	$(*)264$
${}^{11}_{\Lambda}$B	$3/2^+$	$1/2^+$	61	424	−3	−44	−10	475	$(*)503$
${}^{12}_{\Lambda}$C	2^-	1^-	61	175	−12	−13	−42	153	$(*)162$
${}^{15}_{\Lambda}$N	$1/2^+_1$	$3/2^+_1$	44	243	33	−8	−213	99	< 100
${}^{15}_{\Lambda}$N	$3/2^+_2$	$1/2^+_2$	65	451	−2	−16	−10	507	481
${}^{16}_{\Lambda}$O	1^-_1	0^-	−33	−123	−20	1	188	23	26
${}^{16}_{\Lambda}$O	2^-	1^-_2	92	207	−21	1	−41	248	224

6.1.2 Energy spacings between different core states

We also performed a cross-check for the energy spacings between different core states, which are closely connected with the S_N term. The same parameter sets in Eq.6.1 and Eq.6.2 were used for the calculation of the spacings based on the coefficients calculated by Millener's shell model [45, 46, 47]. The results are summarized in Table 6.2. The energy spacings of the beginning and the end of p-shell hypernuclei, such as ${}^{7}_{\Lambda}$Li, ${}^{14}_{\Lambda}$N and ${}^{16}_{\Lambda}$O, are well reproduced by the parametrized effective ΛN interaction, while for mid-p-shell hypernuclei the energy spacings are not well reproduced. Taking account of the consistent description for the spin-doublet spacings with the same interaction, this discrepancy is presumably ascribed to an incomplete wavefunction of the core nucleus in the p-shell model space. In other words, inaccuracy in wavefunctions of ordinary nuclei is revealed by examining the response of nuclear level energies by a Λ hyperon.

Table 6.2: Summary of energy spacings between different core states in p-shell hypernuclei. Energies are given in keV. The top two entries are calculated using the parameters in Eq. 6.1. The other entries are calculated with the parameters in Eq. 6.2. The coefficients and the $\Lambda\Sigma$ values are calculated by Millener's shell model [45, 46, 47]. The present experimental results are marked with asterisks.

	J^π_u	J^π_l	ΔE_{core}	$\Lambda\Sigma$	Δ	S_Λ	S_N	T	ΔE^{th}	ΔE^{exp}
${}^{7}_{\Lambda}$Li	$5/2^+$	$1/2^+_1$	2186	4	77	17	-288	33	2047	2050
${}^{7}_{\Lambda}$Li	$1/2^+_2$	$1/2^+_1$	3565	-20	418	0	-82	-3	3886	3877
${}^{11}_{\Lambda}$B	$1/2^+$	$5/2^+$	718	-5	-88	-19	391	-38	959	1483
${}^{11}_{\Lambda}$B	$3/2^+_3$	$1/2^+_3$	3010	-68	-177	-1	54	-49	2769	2477
${}^{12}_{\Lambda}$C	1^-_2	1^-_1	2000	45	104	-17	386	15	2533	$(*)$2832
${}^{12}_{\Lambda}$C	1^-_3	1^-_1	4804	64	123	6	576	13	5586	$(*)$6050
${}^{15}_{\Lambda}$N	$1/2^+_1$	$3/2^+_1$	2313	-49	86	11	-6	-71	2284	2268
${}^{15}_{\Lambda}$N	$1/2^+_3$	$1/2^+_2$	1635	41	-297	2	477	3	1861	1961
${}^{15}_{\Lambda}$N	$3/2^+_2$	$1/2^+_2$	1635	96	155	0	468	-6	2348	2442
${}^{16}_{\Lambda}$O	1^-_2	1^-_1	6176	-33	-85	19	523	-19	6581	6536

6.2 $^{12}\mathbf{C}(\pi^+, K^+)$ spectrum in coincidence with γ rays

6.2.1 Missing mass spectroscopy of $^{12}_{\Lambda}$C

The mass resolution of the present experiment was not sufficient to observe each peak component of $^{12}_{\Lambda}$C states as obtained in the KEK-E369 experiment, but we succeeded in extracting three significant peaks by gating γ-ray transitions (see Figure 5.4 [c], Figure 5.8 [c-2] and Figure 5.16 [c]). These extracted peaks were fitted with the expected response function estimated in the simulation. The fitting results are listed in Table 6.3 together with the results of the series of SKS experiments, where the newly observed peak is tentatively denoted as #7. For reference of each peak component, see Figure 1.5 and Table 3.1.

The global structure of the $^{12}_{\Lambda}$C spectrum except for the #4 peak have been quite well understood through the theoretically calculated spectrum as shown in Figure 6.1 [39]. In this calculation, they used a shell model, where mixing of core levels due to a Λ hyperon was considered with the Nijmegen model-D ΛN interaction. For the (π^+, K^+) reaction part, the DWIA formalism was adopted. Recently, it is suggested that a parity-mixing intershell coupling model, which calculates positive-parity excited states in an extended shell-model space, gives an explanation for the #4 peak [50]. Although the calculation is still in progress, it gives a new 2^+ state at $B_\Lambda = 3.4$ MeV and this state is naively explained as a configuration of $[^{11}\mathrm{C}^*(5/2^+) \otimes s_\Lambda]\ 2^+$.

In the present experiment, a new peak (#7) is obtained at $B_\Lambda = -4.9$ MeV by gating the $^{11}_{\Lambda}$B$(1/2^+ \rightarrow 5/2^+)$ transition. This result is quite interesting because other SKS experiments have not observed it due to the complex nature of unbound region. The experimental technique for observing the #7 peak is most unique to the present experiment (SKS+Hyperball2). The shell-model calculation by Itonaga *et al.* predicts the 3^- state at $B_\Lambda = -4$ MeV with a prominent cross section as shown in Figure 6.1. This state is interpreted as the $[p_n^{-1}, d_\Lambda]$ configuration. Thus, we suggests that the #7 peak is attributed to the 3^- state but more theoretical studies for this assignment are necessary.

Table 6.3: Results of experiments with SKS for the $(\pi^+, K^+)^{12}_{\Lambda}$C. E566 is the present experiment with SKS and Hyperball2. (A) is obtained from missing mass spectra by gating hypernuclear γ rays ($^{11}_{\Lambda}$B γ rays for #5 and #7, $^{12}_{\Lambda}$C γ rays for #2). (B) is measured from the $^{12}_{\Lambda}$C γ-ray energies.

	B_Λ (MeV)				
Peaks	E140a [48]	E336 [49]	E369 [36]	E566(A)	E566(B)
#1	10.8 (fixed)	10.80 (fixed)	10.76 (fixed)	10.76 (fixed)	10.76 (fixed)
#2	8.1 ± 0.2	8.17 ± 0.06	8.25 ± 0.17	7.84 ± 0.32	7.928 ± 0.005
#3	3.9 ± 0.2	4.71 ± 0.08	4.46 ± 0.11	-	4.710 ± 0.010
#4	-	2.68 ± 0.17	2.70 ± 0.19	-	-
#5	-0.1 ± 0.1	0.20 ± 0.03	0.10 ± 0.04	-0.51 ± 0.13	-
#6	-	-	-1.61 ± 0.09	-	-
#7	-	-	-	-4.93 ± 0.17	-

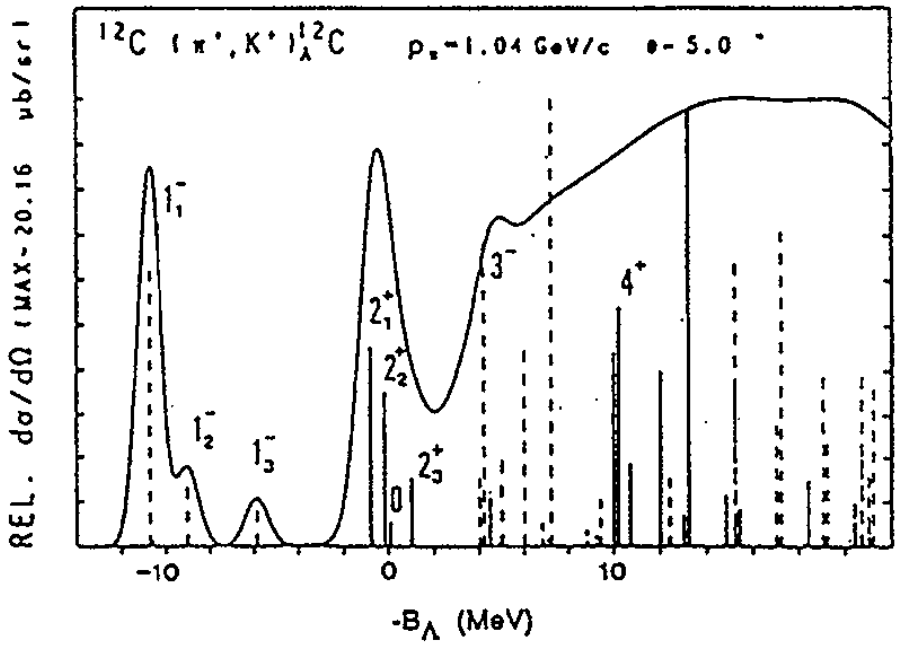

Figure 6.1: Theoretical $(\pi^+, K^+)^{12}_{\Lambda}$C spectrum based on a shell model with the Nijmegen model-D ΛN interaction [39].

Linearity of the missing mass scale

In order to estimate a systematic error for the #7 peak energy, we evaluated the linearity of the missing mass scale by using the excitation energies of the well-known #2 and #5 peaks, which were also separately measured in the γ-ray-gated mass spectra. For the reference energy of the #2 peak, the 1^-_2 state excitation energy measured from the cascading γ-ray transitions ($1^-_2 \rightarrow 2^-_1 \rightarrow 1^-_1$) was used. For the accurate energy of the #5 peak, a old emulsion data [35] was referred. In the emulsion experiment, mass values of the $^{12}_{\Lambda}$C excited states were measured to be 11368.78 ± 0.03 MeV for the 2^+_1 state and 11369.52 ± 0.02 MeV for the 2^+_2 state, where the ^{11}C+Λ threshold energy ($B_\Lambda = 0$) was 11369.72 MeV. By taking the average of the 2^+_1 and 2^+_2 states energies, the reference excitation energy of the #5 peak was obtained to be $B_\Lambda = 0.57 \pm 0.02$. Figure 6.2 shows the difference plot between the KEK-E566 missing mass values and reference mass values, where the mass difference at the #1 peak is fixed to be zero. These mass differences are fitted with a linear function and then extrapolated up to the #7 peak energy. Including the systematic error estimated from the fitting result, the #7 peak energy is determined to be

$$B_\Lambda \;=\; -4.93 \pm 0.17(\mathrm{stat})\ ^{+1.49}_{-0.00}(\mathrm{syst})\ \mathrm{MeV}.$$

The linearity of the missing mass scale in the present experiment is estimated to have a positive offset toward the unbound side in proposition to the B_Λ value. When we compare the #5 peak energies measured in the several SKS experiments (see Table 6.3) with that of the emulsion result, the same tendency of the missing mass linearity is found. The listed energies of the #3 peak also agree with this tendency. The linearity of SKS momentum was checked in detail by H. Hotchi [37] and found to be kept within ± 0.04 MeV/c in the momentum range of 0.65-0.79 GeV/c. By considering the sufficient linearity of SKS momentum, the systematic offsets in the measured B_Λ values are presumably resulted from inaccuracy of the energy loss correction for the beam pions and scattered kaons. On the other hand, the energies of the #2 peak measured in the E140a, E336 and E369 are shifted toward opposite side. This means that the fitting results of #2 peak are systematically shifted due to the tail part of the relatively larger #1 peak. Moreover, asymmetry of peak shape due to the Landau tail of energy loss process, which is found in the present analysis, should enlarge ambiguity of the overlapped small peak positions.

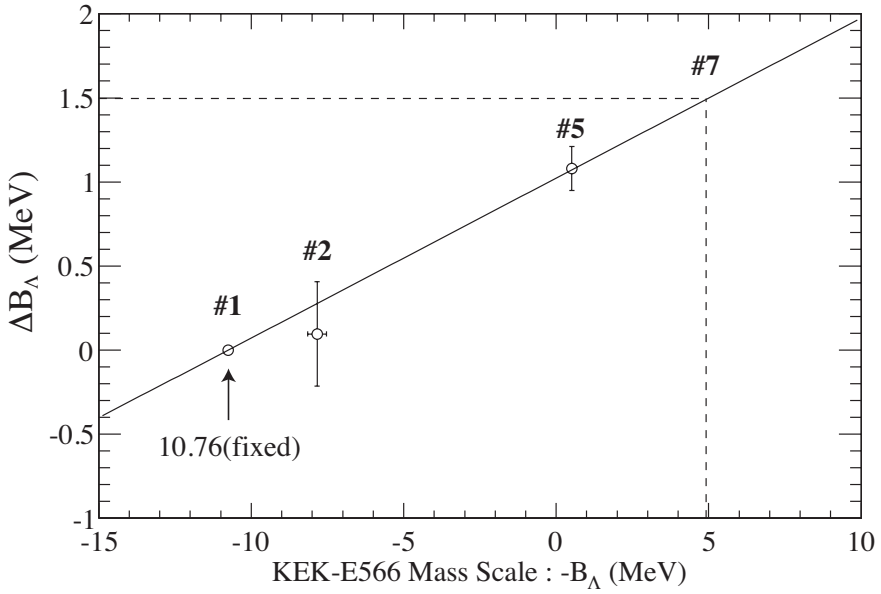

Figure 6.2: Systematic error of the excitation energy scale in the KEK-E566 experiment. The error for #7 peak is extrapolated from the linear fitting result of the mass differences at the #2 and #5 peaks, where the mass difference at #1 peak is constrained to be zero.

6.2.2 Population processes of the 2^-_1 state

When we select the ${}^{12}_{\Lambda}\mathrm{C}(2^-_1 \to 1^-_1)$ transition γ-ray peak, rather complex structure is observed in the missing mass spectrum (see Figure 5.14 [c]). In this subsection, we will discuss interpretation of this structure.

For the origin of the ${}^{12}_{\Lambda}\mathrm{C}(2^-_1 \to 1^-_1)$ transition, the following simple population processes of the 2^-_1 state are considered as also illustrated in Figure 6.3.

(A). Feeding via the $(2^+ \to 2^-_1)$ transition.

(B). Feeding via the $(1^-_3 \to 2^-_1)$ transition.

(C). Feeding via the $(1^-_2 \to 2^-_1)$ transition.

(D). Direct population via the (π^+, K^+) reaction.

For the processes of B and C, we are able to give quantitative estimations from the peak counts of observed γ rays (I_γ). Firstly, the efficiency-corrected yields of the γ rays (Y_γ) is obtained as

$$\begin{aligned} Y_\gamma(2^-_1 \to 1^-_1) &= \frac{I_\gamma(2^-_1 \to 1^-_1)}{\varepsilon_{mass}(2^-_1, 1^-_2, 1^-_1, 2^+)\varepsilon_\gamma(162\ \mathrm{keV})} \\ &= 5837 \pm 868\ , \\ Y_\gamma(1^-_2 \to 2^-_1) &= \frac{I_\gamma(1^-_2 \to 2^-_1)}{\varepsilon_{mass}(1^-_2)\varepsilon_\gamma(2670\ \mathrm{keV})} \\ &= 6622 \pm 1046\ , \\ Y_\gamma(1^-_3 \to 1^-_1) &= \frac{I_\gamma(1^-_3 \to 1^-_1)}{\varepsilon_{mass}(1^-_3)\varepsilon_\gamma(6048\ \mathrm{keV})} \\ &= 4706 \pm 1569\ , \end{aligned}$$

where $\varepsilon_{mass}(X)$ is the ratio of X state events in the mass gate and ε_γ is the photo-peak efficiency of Hyperball2. When we consider the theoretical branching ratio [39], which is modified based on the measured excitation energies of the ${}^{12}_{\Lambda}\mathrm{C}$ states, the efficiency-corrected yield of unobserved $(1^-_3 \to 2^-_1)$ transition is evaluated as

$$\begin{aligned} Y_\gamma(1^-_3 \to 2^-_1) &= Y_\gamma(1^-_3 \to 1^-_1) \cdot \frac{BR(1^-_3 \to 2^-_1)}{BR(1^-_3 \to 1^-_1)} \\ &= 918 \pm 306\ . \end{aligned}$$

Secondly, we estimate the branching ratio of the $M1$ transition (Γ_{M1}) and weak decay (Γ_{weak}) from the 2^-_1 state. The $M1$ transition probability between the spin-doublet states (J_i, J_f) is calculated by the following formula

$$\begin{aligned} \Gamma_{M1} &= 1.76 \times 10^{13} \cdot E_\gamma^3 \cdot B(M1) \quad [1/\mathrm{sec}], \\ B(M1) &= \frac{3}{8\pi} \cdot \frac{2J_f+1}{2J_N+1} \cdot (g_N - g_\Lambda)^2 \quad [\mu_N^2], \end{aligned}$$

where g_N and g_Λ stand for the effective g-factor of the core nucleus and the Λ hyperon, and J_N is the spin of core nucleus. The E_γ is given in MeV. Then, the branching ratio is calculated to be

$$BR(M1) = \frac{\Gamma_{M1}}{\Gamma_{M1} + \Gamma_{weak}} = 0.33 \pm 0.02 \ ,$$

where we give some assumptions as follows.

- $g_N = -0.643$ is obtained from the magnetic moment of ^{11}C ground state.
- $g_\Lambda = -1.226$ is the same value as the free Λ hyperon.
- The weak decay lifetime ($1/\Gamma_{weak}$) of the 2^-_1 state is the same as that of the 1^-_1 state, which was measured to be 212 ± 6 ps in the KEK-E508 experiment [51].

Finally, the contributions from B and C processes to the $M1(2^-_1 \to 1^-_1)$ transition are estimated to be

$$\begin{aligned} N_{A+B+C+D} : N_B : N_C &= 100 : \frac{Y_\gamma(1^-_3 \to 2^-_1) \cdot BR(M1)}{Y_\gamma(2^-_1 \to 1^-_1)} : \frac{Y_\gamma(1^-_2 \to 2^-_1) \cdot BR(M1)}{Y_\gamma(2^-_1 \to 1^-_1)} \\ &= 100 \ : \ 5.2 \pm 1.9 \ : \ 37.4 \pm 8.1 \ , \end{aligned}$$

where N_X denotes contribution from the X process.

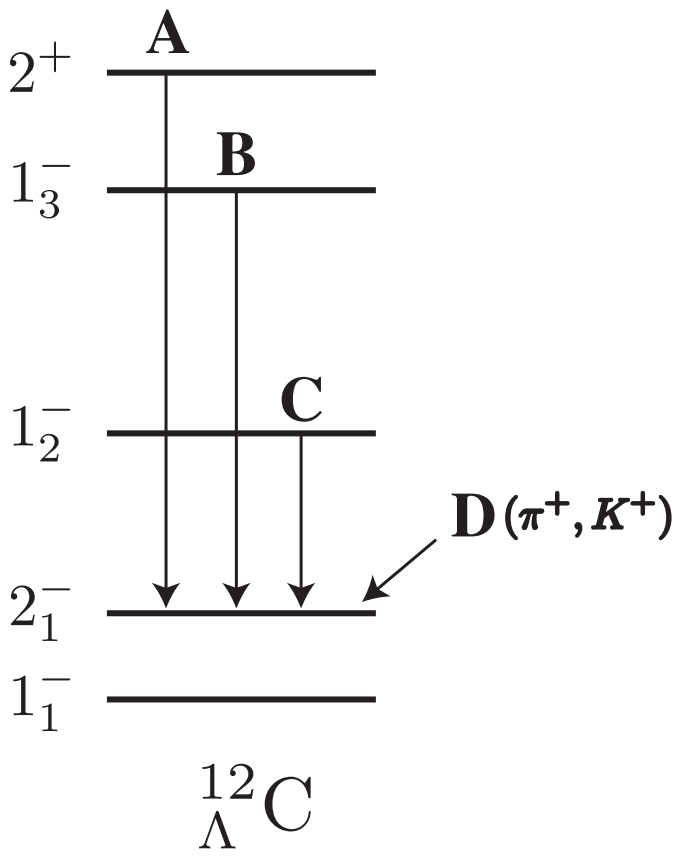

Figure 6.3: Population processes of the $^{12}_{\Lambda}\mathrm{C}(2^-_1)$ state, where simple ones are considered.

We performed a fitting of the mass spectrum attributed to the ${}^{12}_{\Lambda}\mathrm{C}(2^-_1 \rightarrow 1^-_1)$ transition with a simulated response function. The fitting function was made of the 2^+, 1^-_3, 1^-_2 and 2^-_1 components corresponding to the processes of A, B, C and D, respectively. In order to reduce the statical uncertainty, some constraints were adopted to the response function as follows. The 2^-_1, 1^-_2 and 1^-_3 positions were fixed to the E566 results measured from the γ-ray energies and the 2^+ position was fixed to the E369 result. The contributions of 1^-_3 and 1^-_2 in the ${}^{12}_{\Lambda}\mathrm{C}(2^-_1 \rightarrow 1^-_1)$ transition were also fixed to the evaluated values of the processes B and C. In this situation, the fitting parameters were the peak counts of 2^-_1 and 2^+ components.

Figure 6.4 shows the results for each of peak components. The contributions of the four processes are obtained to be

$$N_A : N_B : N_C : N_D \;=\; 38.0 \pm 8.4 \;:\; 5.2 \pm 1.9 \;:\; 37.4 \pm 8.1 \;:\; 19.4 \pm 8.9 \; .$$

The branching ratio of $(2^+ \rightarrow 2^-_1)$ transition

From the fitting result, the branching ratio of $(2^+ \rightarrow 2^-_1)$ transition is calculated as follows. The ratio between processes A and C is expressed by

$$N_A : N_C \;=\; Y(2^+) \cdot BR(2^+ \rightarrow 2^-_1) \;:\; Y(1^-_2) \cdot BR(1^-_2 \rightarrow 2^-_1) \; .$$

Then, we obtain the formula as

$$BR(2^+ \rightarrow 2^-_1) \;=\; \frac{N_A}{N_C} \cdot \frac{Y(1^-_2)}{Y(2^+)} \cdot BR(1^-_2 \rightarrow 2^-_1)$$

By using the E566 results and the production cross sections from the E369 results,

$$\begin{aligned} Y(1^-_2) : Y(2^+) &= 1.04 \pm 0.14 \;:\; 0.99 \pm 0.17 \quad \text{(E369)} \; , \\ BR(1^-_2 \rightarrow 2^-_1) &= \frac{Y_\gamma(1^-_2 \rightarrow 2^-_1)}{Y_\gamma(1^-_2 \rightarrow 2^-_1) + Y_\gamma(1^-_2 \rightarrow 1^-_1)} \\ &= 0.72 \pm 0.15 \quad \text{(E566)} \; , \end{aligned}$$

the branching ratio is determined to be

$$BR(2^+ \rightarrow 2^-_1) = 0.77 \pm 0.33 \; .$$

The production ratio between spin-flip and spin-nonflip states

The production ratio of the spin-flip state (2^-_1) over the spin-nonflip state (1^-_1) is extracted as follows. The ratio between the processes C and D is expressed by

$$N_C : N_D \;=\; Y(1^-_2) \cdot BR(1^-_2 \to 2^-_1) \;:\; Y(2^-_1; \text{spin-flip}) \,,$$

where $Y(2^-_1; \text{spin-flip})$ denotes the production yield of the 2^-_1 state in the direct process in the (π^+, K^+) reaction. By using the E566 results and E369 results,

$$Y(1^-_2) : Y(1^-_1) \;=\; 1.04 \pm 0.14 \;:\; 8.07 \pm 0.38 \quad \text{(E369)} \,,$$

$$BR(1^-_2 \to 2^-_1) \;=\; 0.72 \pm 0.15 \quad \text{(E566)} \,,$$

the ratio between the spin-flip and spin-nonflip ground-state doublet member is deduced to be

$$\begin{aligned} \frac{Y(2^-_1; \text{spin-flip})}{Y(1^-_1; \text{spin-nonflip})} &= \frac{N_D}{N_C} \cdot \frac{Y(1^-_2)}{Y(1^-_1)} \cdot BR(1^-_2 \to 2^-_1) \\ &= 0.048 \pm 0.027 \,. \end{aligned}$$

This result is the first experimental evidence that a spin-flip state is directly populated by the (π^+, K^+) reaction. The hypernuclear production cross sections were studied by Itonaga *et al.* [38] in detail for the (π^+, K^+) reaction by taking into account the elementary amplitudes having spin-flip and spin-nonflip interactions for $\pi^+ n \to \Lambda K^+$. They performed DWIA calculations based on a shell model and predicted that the spin-flip over spin-nonflip cross-section ratio of the $^{12}_{\Lambda}$C ground-state doublet is ~ 2 % at the laboratory scattering angle $\theta_{\pi K} = 5^\circ$. Their prediction is confirmed by the present experiment.

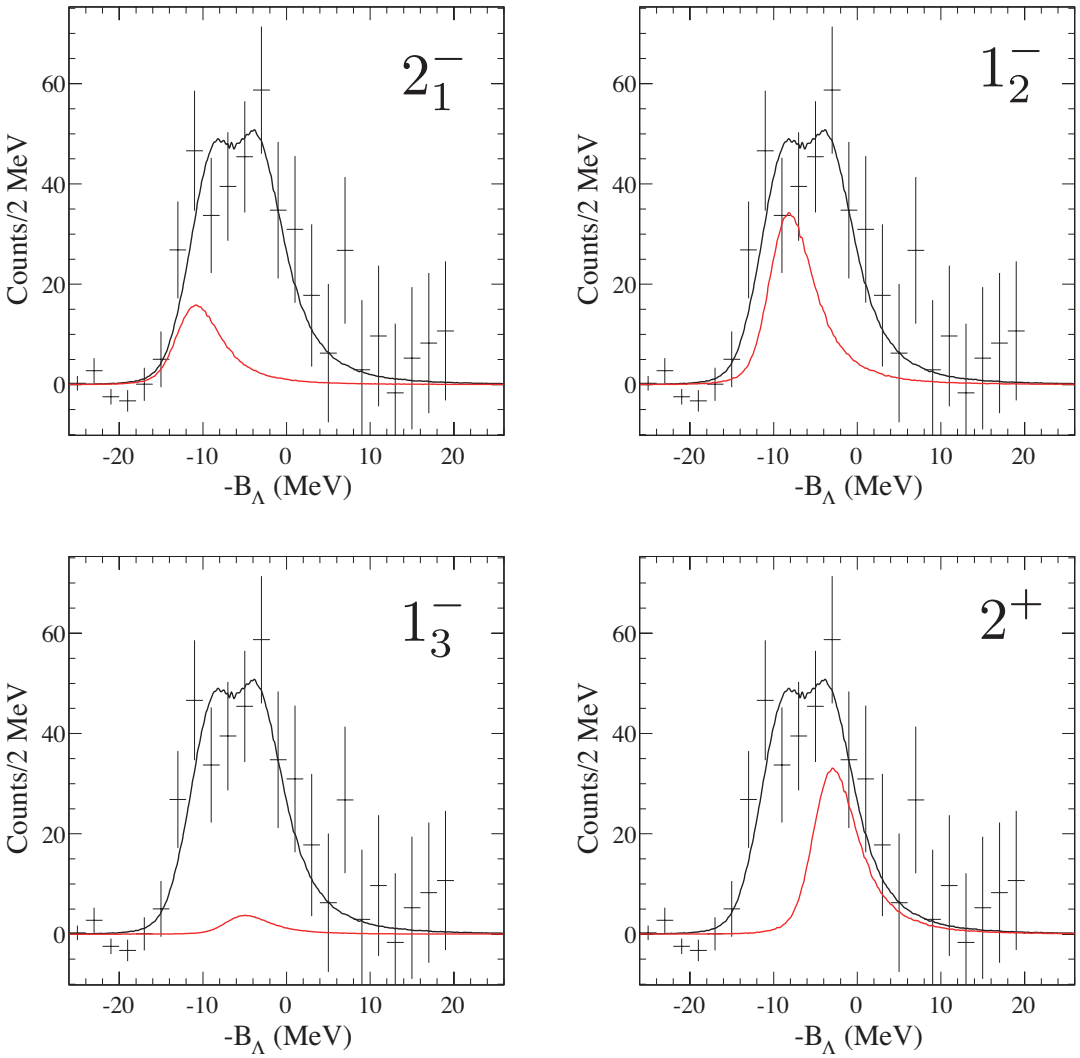

Figure 6.4: Fitting results of the mass spectrum attributed to the ${}^{12}_{\Lambda}\mathrm{C}(2_1^- \rightarrow 1_1^-)$ transition. Obtained contribution of each of the four components is shown in each panel by red lines. The peak positions are fixed to the experimentally determined energies. The peak heights of 1_2^- and 1_3^- are also fixed to the values estimated from observed γ-ray yields.

Reaction angle dependence of the hypernuclear γ ray

We also studied the reaction angle dependence of the hypernuclear γ-ray intensity. Figure 6.5 shows the angular distributions of the cross sections for the $^{12}_{\Lambda}$C states obtained from DWIA calculations based on both the elementary spin-nonflip and the spin-flip amplitudes [52]. The left figure shows cross sections for spin-nonflip states and the right one shows those for spin-flip states. Figure 6.6 shows the reaction angle dependence of the hypernuclear γ-ray intensity after corrections for the SKS acceptance and the tracking efficiency. When we compare these figures, it is found that the reaction angle dependence of the $^{12}_{\Lambda}$C$(1^-_2 \rightarrow 2^-_1)$ transition takes over the distribution of the 1^- state in Figure 6.5. On the other hand, the $^{12}_{\Lambda}$C$(2^-_1 \rightarrow 1^-_1)$ transition shows a peculiar distribution having a significant enhancement around $\theta_{\rm lab} = 10$. By considering the fact that the calculated distributions for spin-flip states have similar enhancements, we propose this measured distribution for another evidence that the spin-flip 2^-_1 state is directly populated by the (π^+, K^+) reaction.

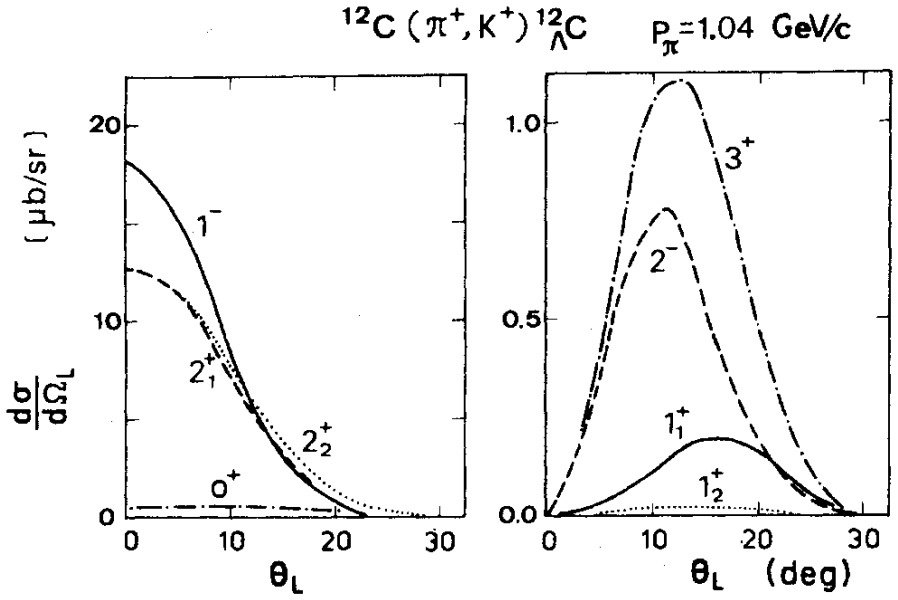

Figure 6.5: The calculated cross sections [52] for the $^{12}_{\Lambda}$C states produced in the (π^+, K^+) reaction at $p_\pi = 1.04$ GeV/c. The horizontal axes are the reaction angle in the laboratory frame. The left figure corresponds to spin-nonflip states and the right one corresponds to spin-flip states. These state have the configurations $[(p_{3/2})^{-1}_n, (s_{1/2})_\Lambda]$ 1^-, 2^- and $[(p_{3/2})^{-1}_n, (p_{3/2})_\Lambda]$ 0^+, 1^+_1, 2^+_1, 3^+ and $[(p_{3/2})^{-1}_n, (p_{1/2})_\Lambda]$ 1^+_2, 2^+_2.

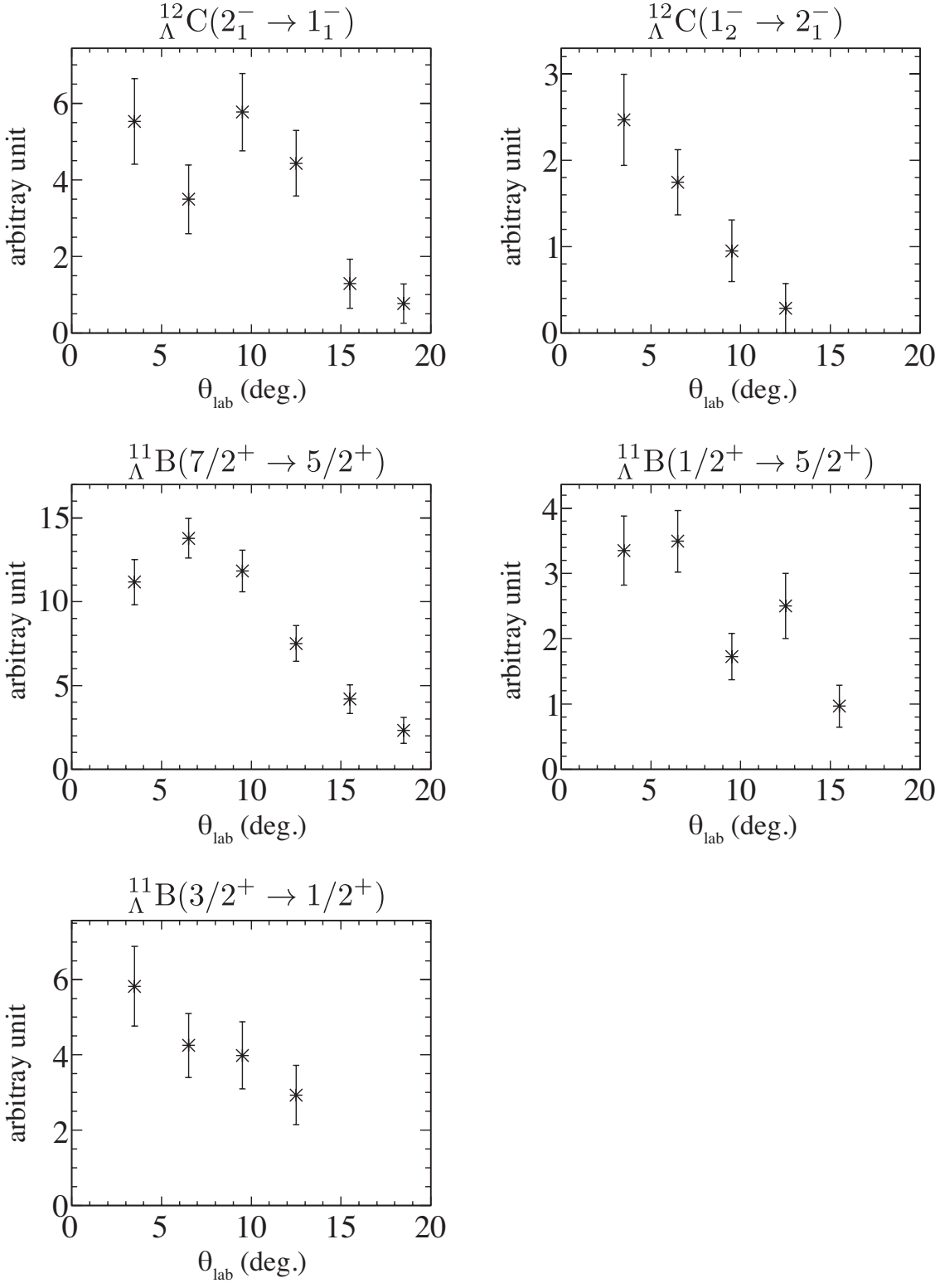

Figure 6.6: Reaction angle ($\theta_{\rm lab}$) dependence of the hypernuclear γ-ray intensities. The intensities are obtained relatively by dividing the measured γ-ray counts with the SKS acceptance (Figure 3.18), where the tracking efficiency (Figure 3.19) is also taken into account.

Chapter 7

Conclusion

We performed a γ-ray spectroscopy experiment on p-shell hypernuclei at the KEK-PS K6 beam line for the investigation of the spin-dependent ΛN interactions including the coupling between the ΛN and ΣN channels (ΛN-ΣN coupling). In the experiment, ${}^{11}_{\Lambda}$B and ${}^{12}_{\Lambda}$C were produced via the ^{12}C(π^+, K^+) reaction at $p_\pi = 1.05$ GeV/c. The hypernuclear production was analyzed by using the K6 beam spectrometer and Superconducting Kaon Spectrometer (SKS). The hypernuclear γ rays were detected by a dedicated germanium detector array, Hyperball2, in coincidence with the (π^+, K^+) reaction.

We succeeded in observing three γ-ray transitions from ${}^{11}_{\Lambda}$B and four transitions from ${}^{12}_{\Lambda}$C and revealed their precise level structures, especially three spin-doublet spacings of ${}^{11}_{\Lambda}$B$(3/2^+, 1/2^+)$, ${}^{11}_{\Lambda}$B$(7/2^+, 5/2^+)$ and ${}^{12}_{\Lambda}$C$(2^-_1, 1^-_1)$. For the ${}^{11}_{\Lambda}$B hypernucleus, observed γ-ray energies and assignments are

$$\begin{aligned}
M1(7/2^+ \to 5/2^+) : E_\gamma &= 263.7 \pm 0.1(\text{stat.}) \pm 1.0(\text{syst.}) \text{ keV}, \\
M1(3/2^+ \to 1/2^+) : E_\gamma &= 503.0 \pm 0.4(\text{stat.}) \pm 1.0(\text{syst.}) \text{ keV}, \\
E2(1/2^+ \to 5/2^+) : E_\gamma &= 1483.3 \pm 0.3(\text{stat.}) \pm 1.0(\text{syst.}) \text{ keV}.
\end{aligned}$$

For the ${}^{12}_{\Lambda}$C hypernucleus, observed γ-ray energies and assignments are

$$\begin{aligned}
M1(2^-_1 \to 1^-_1) : E_\gamma &= 161.5 \pm 0.3(\text{stat.}) \pm 1.0(\text{syst.}) \text{ keV}, \\
M1(1^-_2 \to 2^-_1) : E_\gamma &= 2670.2 \pm 2.9(\text{stat.}) \pm 3.6(\text{syst.}) \text{ keV}, \\
M1(1^-_2 \to 1^-_1) : E_\gamma &= 2839.3 \pm 3.6(\text{stat.}) \pm 3.2(\text{syst.}) \text{ keV}, \\
M1(1^-_3 \to 1^-_1) : E_\gamma &= 6048.4 \pm 3.2(\text{stat.}) \pm 6.7(\text{syst.}) \text{ keV}.
\end{aligned}$$

In the present analysis, many improvements were made to the analysis procedures as compared with the previous analysis. The 6-MeV γ transition of ${}^{12}_{\Lambda}$C was observed

for the first time in this work. In addition, the other six γ transitions were confirmed with better sensitivity than the previous analysis.

The effect of ΛN-ΣN coupling was systematically studied with the parametrized effective ΛN interactions throughout the experimentally available doublet spacings including these new data. As a result, it is found that the NSC97f interaction gives a reasonable account of ΛN-ΣN coupling to the p-shell hypernuclear state as well as the s-shell case. Furthermore, validity of the present framework is demonstrated by reproducing a large body of hypernuclear level spacings with relatively few YN parameters. In conclusion, the four strengths of the spin-dependent ΛN interactions in p-shell hypernuclei are experimentally constrained to be

$$\Delta = 0.43 \text{ or } 0.33, \;\; S_\Lambda = -0.02, \;\; S_N = -0.4, \;\; T = 0.03 \;\; \text{MeV} \; ,$$

even though level spacings between different core states were not well reproduced in mid-p-shell hypernuclei such as ${}^{11}_{\Lambda}$B and ${}^{12}_{\Lambda}$C. We suggests that an improvement of shell-model calculations, in particular the wavefunctions of core nuclei, is necessary to solve these discrepancies.

The structure of ${}^{12}_{\Lambda}$C was studied through a hybrid missing mass spectroscopy method, which was enabled by further analysis of the missing mass reconstruction in the present work. We succeeded in observing three peaks in the ${}^{12}_{\Lambda}$C mass spectrum by tagging the specified hypernuclear γ-ray transitions. The two peaks are related to the s_Λ and p_Λ states, and their excitation energies are consist with the series of SKS experiments. The remaining peak at $B_\Lambda = -4.9 \pm 0.17(\text{stat}) \, {}^{+1.49}_{-0.00}(\text{syst})$ MeV is observed for the first time in the present experiment by selecting the ${}^{11}_{\Lambda}\text{B}(1/2^+ \to 5/2^+)$ transition. Although more theoretical studies are necessary, we suggest that this peak is attributed to the ${}^{12}_{\Lambda}\text{C}(3^-)$ state with the $[p_n^{-1}, d_\Lambda]$ configuration.

The production process of the ${}^{12}_{\Lambda}\text{C}(2^-_1)$ state was examined by analyzing the mass spectrum attributed to the ${}^{12}_{\Lambda}\text{C}(2^-_1 \to 1^-_1)$ transition. We succeeded in extracting a small contribution from the spin-flip interaction in the Λ production. This result is the first experimental evidence that the spin-flip 2^-_1 state is directly populated by the (π^+, K^+) reaction. In addition, the ${}^{12}_{\Lambda}\text{C}(2^-_1 \to 1^-_1)$ transition yield as a function of the reaction angle also suggests a significant contribution of the spin-flip interaction. We also deduced the branching ratio of the ${}^{12}_{\Lambda}\text{C}(2^+ \to 2^-_1)$ transition to be 0.77 ± 0.33. The 2^+ state at $B_\Lambda = 2.7$ MeV is understood through the parity-mixing intershell coupling mediated by a Λ hyperon but theoretical calculations are still in progress. This experimentally determined branching ratio provides precious information to understand the nature of the state.

Bibliography

[1] Th. A. Rijken, V. G. J. Stoks and Y. Yamamoto, Phys. Rev. C **59** (1999) 21.

[2] B. Holzenkamp, K. Holinde and J. Speth, Nucl. Phys. A **500** (1989) 485.

[3] A. Reuber, K. Holinde and J. Speth, Nucl. Phys. A **570** (1994) 543.

[4] Prog. Theor. Phys. Suppl. **137** (2000), edited by M. Oka, K. Shimizu and K. Yazaki.

[5] Y. Yamamoto *et al.*, Prog. Theor. Phys. **117** (1994) 361.

[6] D. J. Millener, C. B. Dover and A. Gal, Phys. Rev. C **38** (1988) 2700.

[7] A. Gal, J. M. Soper and R. H. Dalitz, Ann. Phys. **63** (1971) 53.

[8] A. Gal, J. M. Soper and R. H. Dalitz, Ann. Phys. **72** (1972) 445.

[9] A. Gal, J. M. Soper and R. H. Dalitz, Ann. Phys. **113** (1978) 79.

[10] D. J. Millener *et al.*, Phys. Rev. C **31** (1985) 499.

[11] D. J. Millener, Nucl. Phys. A **691** (2001) 93c.

[12] D. J. Millener, Nucl. Phys. A **754** (2005) 48c.

[13] S. Cohen and D. Kurath, Nucl. Phys. **73** (1965) 1.

[14] Y. Akaishi *et al.*, Phys. Rev. Lett. **84** (2000) 3539.

[15] H. Tamura, Nucl. Phys. A **639** (1998) 83c.

[16] H. Tamura *et al.*, Phys. Rev. Lett. **84** (2000) 5963.

[17] K. Tanida *et al.*, Phys. Rev. Lett. **86** (2001) 1982.

[18] J. Sasao *et al.*, Phys. Lett. B **579** (2004) 258.

[19] M. Ukai *et al.*, Phys. Rev. C **73** (2006) 012501.

[20] H. Akikawa *et al.*, Phys. Rev. Lett. **88** (2002) 082501.

[21] H. Tamura *et al.*, Nucl. Phys. A **754** (2005) 58c.

[22] Y. Miura *et al.*, Nucl. Phys. A **754** (2005) 75c.

[23] M. Ukai *et al.*, Phys. Rev. C **77** (2008) 054315.

[24] M. Ukai *et al.*, Phys. Rev. Lett. **93** 232501.

[25] D. J. Millener, in *Hypernuclear Physics with Electromagnetic Probes*, edited by L. Tang and O. Hashimoto (Hampton University, Hampton, VA, 1999), p. 79.

[26] E. Hiyama, Phys. Rev. Lett. **85** (2000) 270.

[27] R. E. Chrien *et al.*, Phys. Rev. C bf 41 (1990) 1062.

[28] D. J. Millener, *private communication.*

[29] R. H. Dalitz, D. H. Davis and D. N. Tovee, Nucl. Phys. A **450** (1986) 311c.

[30] H. Bandō *et al.*, Int. J. Mod. Phys. A **05** (1990) 4021.

[31] T. Fukuda *et al.*, Nucl. Instr. Meth. A **361** (1995) 485.

[32] G. Duchêne *et al.*, Nucl. Instr. Meth. A **432** (1999) 90.

[33] S. Morinobu, *private communication.*

[34] J. Myrhein and L. Bugge, Nucl. Instr. Meth. **160** (1979) 43.

[35] D. H. Davis, Nucl. Phys. A **547** (1992) 369.

[36] H. Hotchi *et al.*, Phys. Rev. C **64** (2001) 044302.

[37] H. Hotchi, Ph.D. Thesis, University of Tokyo (2000).

[38] K. Itonaga *et al.*, Phys. Rev. C **49** (1994) 1045.

[39] K. Itonaga *et al.*, Prog. Theor. Phys. Suppl. **117** (1994) 17.

[40] R. H. Dalitz and A. Gal, Ann. Phys. **116** (1978) 167.

[41] S. Backer and R. D. Cousins, Nucl. Instr. Meth. **221** (1984) 437.

[42] Y. Ma *et al.*, Eur. Phys. J. A **33** (2007) 243.

[43] Y. Ma *et al.*, Nucl. Phys. A **835** (2010) 422.

[44] Y. Ma, Ph.D. Thesis, Tohoku University (2009).

[45] D. J. Millener, Springer Lecture Notes in Physics **724** (2007) 31.

[46] D. J. Millener, Nucl. Phys. A **804** (2008) 84.

[47] D. J. Millener, Nucl. Phys. A **881** (2012) 298.

[48] T. Hasegawa *et al.*, Phys. Rev. Lett. **74** (1995) 224.

[49] O. Hashimoto and H. Tamura, Prog. Part. Nucl. Phys. **57** (2006) 564.

[50] T. Motoba, Nucl. Phys. A **639** (1998) 135c.

[51] S. Kameoka *et al.*, Nucl. Phys. A **754** (2005) 173c.

[52] H. Bandō *et al.*, Phys. Rev. C **39** (1989) 587.